THE ANTENNA LABORATORY

RESEARCH ACTIVITIES in ---

Automatic Controls — *Antennas* — *Echo Area Studies*
Microwave Circuits — *Astronautics* — *E-M Field Theory*
Terrain Investigations — *Radomes* — *Systems Analysis*
Wave Propagation — *Submillimeter Applications*

Proceedings of the OSU-RTD Symposium
on
Electromagnetic Windows

2-4 June 1964

Vol. IV

Department of ELECTRICAL ENGINEERING

THE OHIO STATE UNIVERSITY
RESEARCH FOUNDATION
Columbus, Ohio

CLEARINGHOUSE FOR FEDERAL SCIENTIFIC AND TECHNICAL INFORMATION CFSTI
DOCUMENT MANAGEMENT BRANCH 410.1

LIMITATIONS IN REPRODUCTION QUALITY

ACCESSION # [illegible]

☒ 1. WE REGRET THAT LEGIBILITY OF THIS DOCUMENT IS IN PART UNSATISFACTORY REPRODUCTION HAS BEEN MADE FROM BEST AVAILABLE COPY.

☒ 2. A PORTION OF THE ORIGINAL DOCUMENT CONTAINS FINE DETAIL WHICH MAY MAKE READING OF PHOTOCOPY DIFFICULT.

☐ 3. THE ORIGINAL DOCUMENT CONTAINS COLOR, BUT DISTRIBUTION COPIES ARE AVAILABLE IN BLACK-AND-WHITE REPRODUCTION ONLY.

☐ 4. THE INITIAL DISTRIBUTION COPIES CONTAIN COLOR WHICH WILL BE SHOWN IN BLACK-AND-WHITE WHEN IT IS NECESSARY TO REPRINT.

☐ 5. LIMITED SUPPLY ON HAND: WHEN EXHAUSTED, DOCUMENT WILL BE AVAILABLE IN MICROFICHE ONLY.

☐ 6. LIMITED SUPPLY ON HAND: WHEN EXHAUSTED DOCUMENT WILL NOT BE AVAILABLE.

☐ 7. DOCUMENT IS AVAILABLE IN MICROFICHE ONLY.

☐ 8. DOCUMENT AVAILABLE ON LOAN FROM CFSTI (TT DOCUMENTS ONLY).

☐ 9.

PROCESSOR: [illegible]

TSL-107-10 64

Proceedings of the OSU-RTD Symposium
on
Electromagnetic Windows

2-4 June 1964

Vol. IV
Oral Papers Received too Late for Inclusion in Vols. I, II, and III
Papers Submitted for the Proceedings Only

FOREWORD

The papers presented in this report were submitted for the Seventh Symposium on Electromagnetic Windows held at The Ohio State University, Columbus, Ohio, 2, 3, and 4 June 1964. They were compiled by Alan I. Slonim of The Ohio State University under Air Force Contract AF 33(615)-1081 administered by The Research and Technology Division, Air Force Systems Command, Wright-Patterson Air Force Base, Ohio with Richard A. Ireland serving as Task Engineer.

The proceedings are published in five volumes as follows:

Vol. I

Session I - Objectives and New Techniques
Session II - Materials for High Temperature Applications

Vol. II

Session III - Electrical Design
Session IV - Structural Design for Large Radomes

Vol. III

Session V - Fabrication and Testing of Airborne Radomes
Session VI - Hypersonic Environment

Vols. IV and V

Oral papers received too late for inclusion in Vols. I, II, and III.
Papers submitted for the proceedings only.

Vol. IV

CONTENTS

ORAL PAPERS RECEIVED TOO LATE FOR INCLUSION IN VOLS. I, II, AND III

PAPERS SUBMITTED FOR THE PROCEEDINGS ONLY

A. High Temperature Telemetry Antennas for Asset,
H.W. Krah (Session VI)

B. Rain Erosion Resistance of Slip Cast Fused Silica Radomes,
R.L. Hallse, R.A. Fortain

C. Advantages of Dual Wall Radome Construction for Tactical Radar Systems,
William M. Foster

D. Microwave Fields Near a Hollow Dielectric Wedge and Dielectric Slab,
G. Tricoles, E. Rope

E. Application of a Ray Tracing Method for Predicting Radome Errors to a Small Radome,
G. Tricoles, D. Gelman

F. Radomes for Microwave Applications,
A.G. Holtum, Jr., K.E. McKee

G. The Use of Traveling-Wave Structures in Integrated Antenna-Radome Design,
John R. Baechle

H. Error and Limitation Analysis on the Measurement of Dielectric Properties by Use of the Shorted Waveguide Reflection Theory at High Temperatures,
Russell W. Johnston

HIGH TEMPERATURE TELEMETRY ANTENNAS FOR ASSET

by

J. W. Krah
Senior Engineer, Electronics
Missile and Space Engineering Division
MCDONNELL AIRCRAFT CORPORATION
ST. LOUIS, MISSOURI

INTRODUCTION

The severe aerodynamic heating encountered by re-entry vehicles has required the design of antennas capable of withstanding high surface temperatures. For hypersonic glide re-entry vehicles the time duration of the high temperature environment is much longer than that associated with typical ballistic re-entry vehicles. This paper describes the development of two antennas used on ASSET, a hypersonic glide re-entry vehicle. These are (1) the flush mounted dielectric loaded U slot configuration shown in Figure 1 for the VHF telemetry band and (2) the pressurized "open ended" waveguide X-Band antenna shown in Figure 2. This work was accomplished, in part, on Contract No. AF33(616)-8106 for Project ASSET.

While the final VHF antenna performance did not fully meet the design objectives, it has proved to be adequate for satisfying the data transmission requirements of the ASSET. The X-Band antenna completely satisfied the design objectives.

DESIGN OBJECTIVES

The overall design objective was to supply telemetry data from a hypersonic glide re-entry vehicle constructed of non-ablative material; i.e., the structure was radiation cooled. Surface temperatures in excess of 2000° F were predicted for the VHF antenna configuration.

The mission profile was such that a hemispherical radiation pattern with coverage to the right of the test vehicle would be required for satisfactory telemetry system performance. This was based on the flight profile for a launch at the ETR (Eastern Test Range, formerly Atlantic Missile Range).

The antenna electrical performance criteria necessary to satisfy the mission objectives are comparable to those for similar payloads. However, the vehicle shape and flight trajectory are such that shock induced ionization is expected to cause VHF blackout over a portion of the flight. To provide telemetry during this VHF blackout interval, X-Band telemetry was employed, thus the requirement for an X-Band antenna.

The power level required to cause voltage breakdown (arc over) at the antenna surface in the presence of the shock induced ionization was computed[1] and the proposed system output power was well below that required for breakdown across the aperture of the final design. However, the spacing between some elements internal to the VHF antenna was less than the aperture dimension and suitable design precautions were observed particularly in the connector and the feed point. The X-Band waveguide was pressurized and required a pressure window on the antenna which takes the very simple form of an open-ended waveguide.

The physical environments to which the antennas were designed are very typical of missile booster environments in all areas except temperature. It was recognized that specifying maximum operating temperatures, even with time intervals, did not represent a realistic approach for establishing the design criteria. Extensive wind tunnel tests on the ASSET vehicle configuration provided heat transfer data in the area of the antenna location. From this data and the expected flight trajectory, the temperature environments for the VHF and X-Band antennas were calculated. For the small X-Band antenna, the fore to aft surface temperature gradient is not significant; however, for the VHF antenna, with a large surface area, these temperature gradients must be considered in the selection of materials and in testing of the hardware.

THERMAL TEST METHODS

The development of the high temperature antenna requires realistic thermal testing as well as realistic specification of the thermal environment. A considerable part of this development effort was expended in developing suitable test criteria and test methods.

Although the actual flight antennas encounter an aerodynamic heating environment, the thermal testing of the antennas was conducted in a radiant heat lamp facility. The major objective of these tests was to simulate as accurately as possible the same temperature profile as predicted for the flight hardware. Since the initial test article was the antenna dielectric and not the complete antenna system, a means for accurately controlling the radiant energy from the lamps was needed. Attaching the control thermocouples directly to the dielectric was found to be unsuitable due to the low material thermal conductivity. Control thermocouples attached to the antenna mounting structure also were unsuitable because the structure itself would heat up faster than the dielectric, causing the lamp bank to go off prematurely. A calorimetric method of controlling the lamp banks was finally selected. This method was derived by computing the thickness of metallic blocks (to which thermocouples could easily be attached) which would produce the same surface temperature as the antenna dielectric under the flight heating environment. Thermocouples were then attached to these blocks to control

1 C. A. Hinrichs, "Ionization Enhanced Antenna Voltage Breakdown", McDonnell Aircraft Report No. 9111.

the power input to the lamps. The fore to aft temperature gradient expected on the flight antenna was simulated by dividing the heat source into three banks of lamps and controlling each of these banks with the calculated temperature history for three control locations, as illustrated in Figure 3.

The test specimen and control blocks are painted black to obtain a uniform high emissivity which is necessary in order to absorb the energy radiated from the lamps. Thermocouples are attached to the test specimen and the output recorded for comparison to the predicted time-temperature history thus providing the information necessary to prove test validity.

In order to obtain the required heating rates, it was necessary to place a metal reflector over the quartz lamp bank. However, the metallic sheet in the near field of the antenna proved very unsatisfactory for making measurements. The electrical characteristics were measured with the reflector in place and were monitored for change during the thermal testing. The results are not as accurate or as conclusive as is desired but have proved to be indicative and acceptable for the present program.

This does not alleviate the necessity for more suitable and adequate test facilities for future program support.

VHF ANTENNA DEVELOPMENT

As stated previously, the radiation pattern required for the ASSET telemetry systems was essentially hemispheric on the right side of the vehicle. The system parameters required an essentially high radiator efficiency and low VSWR. Flush mounting of the antenna with minimum antenna thickness was desired to keep peak surface temperatures as low as possible.

Consideration was given to a linear slot and a notch excited surface to fulfill these objectives for the VHF system. However, their size and required location for installation produced many problems in integrating these designs into the airframe of the ASSET vehicle. The linear slot would necessarily have been much to large to mount without seriously affecting the structural integrity of the vehicle. The notch excited surface had its limitations, in that, the areas in which it could be located, were areas where temperatures were extremely high (e.g. wing leading and trailing edges).

The cavity-backed U-Slot antenna design was chosen because of its extremely low profile, thus its adaptability into the airframe. Although its length and width were large for this application, it was felt that by dielectrically loading the cavity the dimensions could be controlled within reason and the smallest possible flush mounted antenna could be realized.

Material studies were initiated to find a dielectric material suitable for this application. A high temperature dielectrometer was utilized to measure dielectric constant and loss tangents of materials at temperatures up to 3000° F. Tests were conducted on fused quartz, boron

nitride, beryllium oxide, pyroceram and aluminum oxide (alumina). Samples of nickel, silver, platinum, and gold platings on some of the above materials were subjected to the high temperature in an oven. The capability of the platings to withstand the temperature in an oxidizing atmosphere was of prime concern. Nickel plating over a molybdenum-manganese base on aluminum oxide appeared to be superior in surviving the environment.

Alumina was therefore selected as the best material for this application. Alumina's dielectric constant of 9.5 (Room temperature) and low loss tangent together with the availability of proven methods of metallizing its surface were deciding factors in the selection.

Electrical prototypes were constructed to experimentally determine the slot width and length, location of the feed point and minimum cavity size. The electrical properties of alumina were reproduced in a Stycast material which was used as the cavity dielectric in all electrical development testing. Optimum performance of the antenna was achieved at 237.8 megacycles with a cavity size of 7 inches X 6.75 inches X 0.5 inches. The slot length and width required were 12 inches and 1.5 inches respectively.

The antenna location was governed by the required radiation pattern and maximum surface temperatures on the vehicle. It was possible to locate it on the vehicle at a point where surface temperatures were minimized. It was also desired to locate it on a flat surface since flat ceramic bodies are more easily fabricated than ones with complex curvatures.

The final location was determined by radiation pattern measurement on a 1/4 scale model of the vehicle. A location on the right side of the vehicle above the wing and toward the rear was chosen.

The mechanical installation of the antenna on a structure designed to expand and contract proved to be another problem area. The difference in thermal coefficients of expansion of the alumina and the vehicle structural material caused concern over excessive mechanical stresses being induced into the antenna by the structure. The same problem existed between any metal antenna mounting flange and the ceramic body. Although metal to ceramic seals have been made successfully in the past, an expansion joint was required in this antenna design. Both of these problems led to a design of mounting the metallized ceramic body clamped between two surfaces as shown in Figure 4.

Since the antenna was to operate at surface temperatures approaching 2000° F a suitable connector and coaxial cable were required. The connector and cable chosen were designed and fabricated by Electronic Specialty Co. A cross-section of the antenna connector is also shown in Figure 4. The connector shell and center-conductor are made of KOVAR, a nickel-alloy steel, whose thermal expansion characteristics approximate those of alumina. The center conductor is brazed to the metallized outer surface of the cavity (slot-side) with a high temperature braze material. An expansion joint is effected between the thin wall of the center-conductor and the alumina. The connector shell and alumina dielectric is also brazed to the metallized alumina body.

The connector was silver-plated and a flash of rhodium added to give protection from oxidation at temperature. A high temperature metal to metal seal is incorporated for a seal with the mating connector.

The mating connector is fabricated of KOVAR and attached to a cable manufactured by McGraw-Edison Co. The cable assembly is shown in Figure 5. The inner and outer conductors are of OFHC copper. A powdered silica is used as the dielectric. The outer conductor is sheathed within a AISI 347 stainless steel jacket. The cable used has a diameter of .170 inch although larger cables with smaller attenuation are available.

Before the VHF antenna design could be finalized, the capability of the alumina block to withstand the high heating rates and consequent large thermal gradients had to be demonstrated. A number of blocks were subjected to what was thought to be the required environment with numerous failures. Due to the low thermal conductivity of the test specimen, problems were encountered in attempting to control the heat flux inputs by measuring the surface temperature of the dielectric with thermocouples. Consequently, surface temperatures higher than those desired were attained and caused failures of the ceramic bodies due to excessive temperature gradients (thermal shock). The calorimetric control system described earlier was utilized and the alumina body survived the required environment.

The black paint, used during thermal tests to enhance absorption of energy from the radiant heat lamps, was also applied to the flight hardware. The emissivity of nickel and alumina is approximately 0.3 while for the black paint it is 0.8. According to theory, the increase in emissivity will allow more heat to be radiated from the antennas during flight and result in reduced surface temperatures.

An engineering model of the antenna was then subjected to the radiant heat test and electrical measurements were made. The results indicated that a very definite lowering of resonant frequency at elevated temperatures had occurred. It was determined after the test that a significant part of the shift was due to a change in position of the metal reflector required for the quartz lamps. The change in physical size of the cavity and the slot also contributed. Another contributing factor was the change in dielectric constant of the alumina at elevated temperature.

The curve of Figure 6 exhibits the narrow-band characteristic of the antenna at room temperature. Although the dielectric constant change with temperature was anticipated, it was felt that the magnitude of the shift would not affect the antenna tuning. Obviously, this assumption was not valid for the U-Slot antenna. Possibly a more wideband antenna type would have given much better performance. The frequency shift was in the range of 5 megacycles and possibly with additional bandwidth the frequency shift could be tolerated.

At this time, it was decided to attempt to limit the antenna temperature to a point where the telemetry system signal margins could absorb the mismatch loss due to the frequency change. A number of tests were conducted to determine the shift in frequency with temperature. A quartz window and insulation were placed over the basic radiator to decrease its maximum temperature from about 2000° F to less than 1000° F.

A typical cross-section is shown in Figure 7. The quartz window is 0.125 inches thick and is painted with the black ceramic paint to increase its emissivity. Beneath the window is a 0.125 inch layer of H. I. Thompson's A-100 Fibrous insulation. A layer of CS 1000 insulation is clamped between the vehicle skin and the vehicle structure to eliminate a direct heat "short" at the edges of the antenna. The antenna is mounted in its retainer on a layer of Refrasil Cloth which is also wrapped around the sides of the antenna.

This configuration reduced the antenna temperatures to a maximum of 700° F as shown in the temperature history of Figure 8. The antenna is tuned to a resonant frequency higher than the transmitter frequency at room temperature. The resulting mismatch loss is absorbed by the excessive system signal margin present when the vehicle is "on the pad". The amount of de-tuning is obtained by predicting the antenna temperature history and by knowing its characteristic change in resonant frequency with temperature, the magnitude of the de-tuning is determined. The average detuning on ASSET antennas has been about 3 megacycles.

Since this antenna configuration satisfied the ASSET telemetry system requirement, no further development effort was undertaken.

X-BAND ANTENNA DEVELOPMENT

The radiation pattern required for the X-Band telemetry was identical to that required for the VHF system. An antenna capable of flush mounting and withstanding one atmosphere of differential pressure was required. The open-ended waveguide antenna was chosen because of its adequate radiation pattern and relative simple mechanical design.

All material studies, fabrication techniques and experience were applicable to the development of the X-Band antenna. Alumina was chosen as the window material for this reason. A window was fabricated of a Stycast material and used to determine the window thickness. The thickness of the alumina window for minimum VSWR at 9320 megacycles was determined to be .215 inches. A VSWR vs. frequency plot is shown in Figure 9.

The problem of maintaining one atmosphere of differential pressure inside the waveguide during elevated temperatures was considered a major one. An effective seal between the alumina window and the waveguide walls had to be accomplished. A cross-section of the antenna is shown in Figure 10 to illustrate how this was accomplished. The antenna mounting flange was fabricated of KOVAR. Although the thermal expansion characteristics of alumina and KOVAR are similar, it was decided to add an expansion joint between the window and the mounting flange. This expansion joint is accomplished by brazing the

alumina window inside a .010 inch thick KOVAR expansion sleeve whose inside dimensions are that of standard MS 90035-52 waveguide. The expansion sleeve is approximately twice as long as the thickness of the window. The sleeve is then brazed to the mounting flange. The mounting flange has been machined to dimensions to allow a small gap around the expansion sleeve. All stresses induced by differences in thermal expansion characteristics between the alumina and the KOVAR mounting flange are then relieved in the thin expansion sleeve. Behind the expansion sleeve, a length of standard MS-90035-52 waveguide and a MS90058-40B waveguide flange are brazed.

The braze materials used are shown in Figure 11. It should be noted that various braze materials were used. This is possible because temperatures throughout the antenna vary as shown in the temperature history of Figure 12. The use of different braze materials allowed the brazing to be accomplished in three separate steps. Maximum precision in positioning the parts was therefore obtained.

Oxidation of the basic materials at elevated temperatures was another problem area. A highly conductive plating or coating was required to allow the antenna to operate efficiently. A silver plating with a rhodium flash was used.

Temperature tests of this antenna were conducted using the quartz lamp radiant heat facility. The antenna VSWR varied slightly during thermal tests but the change was insignificant. The one atmosphere of pressure differential inside the waveguide was maintained throughout the test. The pressure differential increased slightly due to expansion of the air inside waveguide as its temperature was increased.

CONCLUSIONS

The antennas described were developed to satisfy a particular program and requirement. The VHF antenna does not meet the design expectations and is far from optimum in thermal performance; however it does satisfy the present program requirements.

Problems were encountered in testing antenna electrical characteristics at high temperature. Improvements in testing methods were required and were partially achieved. Improvement in test facilities is still required.

Specification of maximum steady-state temperatures for antennas is not a realistic description of the environment encountered in transient heating. The heat flux and/or the temperature history should be specified.

The fabrication technique used for the X-Band antenna has been satisfactory.

The fabrication technique for the VHF antenna leaves something to be desired in the areas of producibility and dielectric characteristics. Additives to alumina may provide a material with improved thermal stability of dielectric constant. The manufacturing technique can be improved and should be suitable for large quantity production.

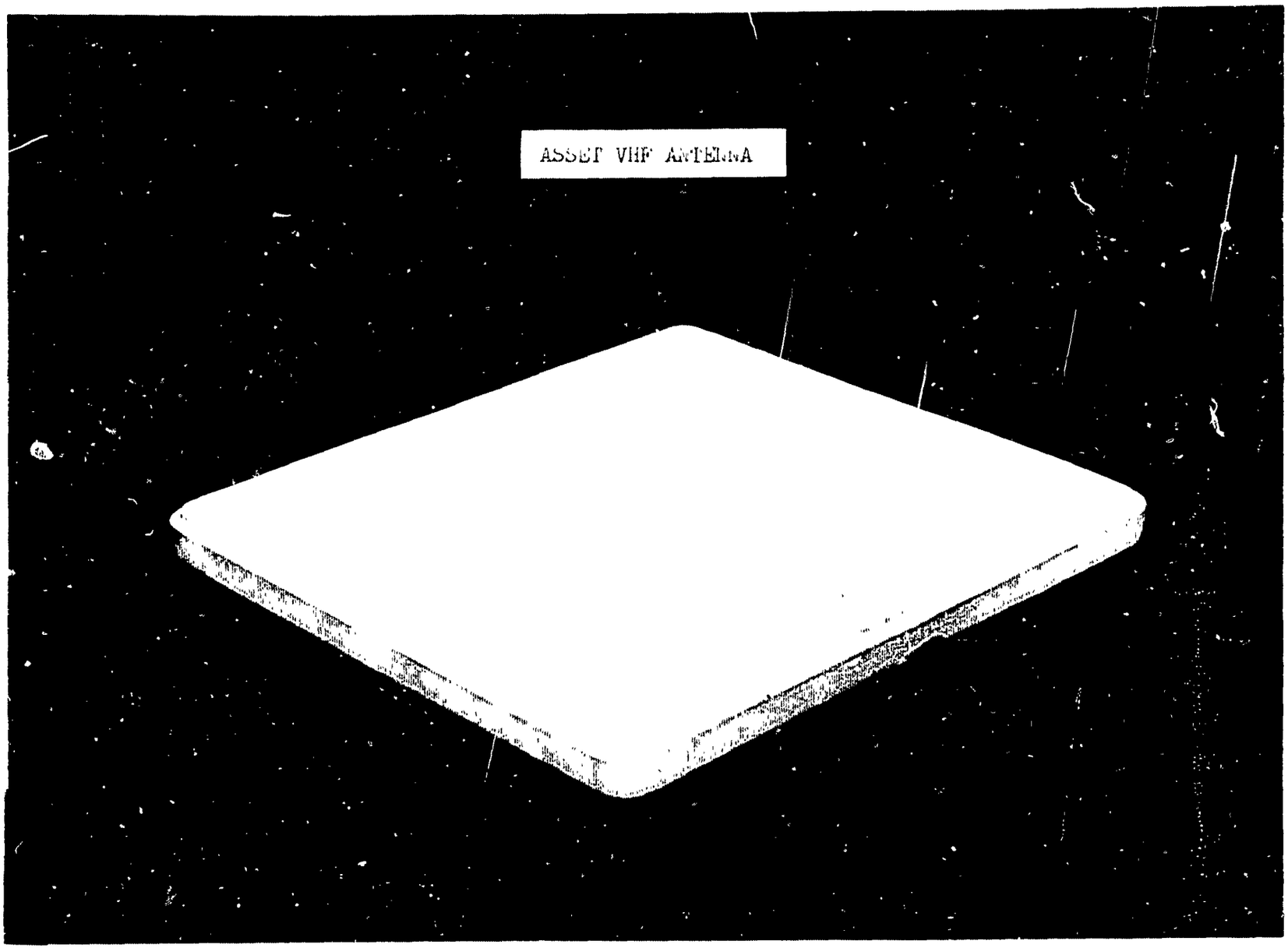
ASSET VHF ANTENNA

Figure 2

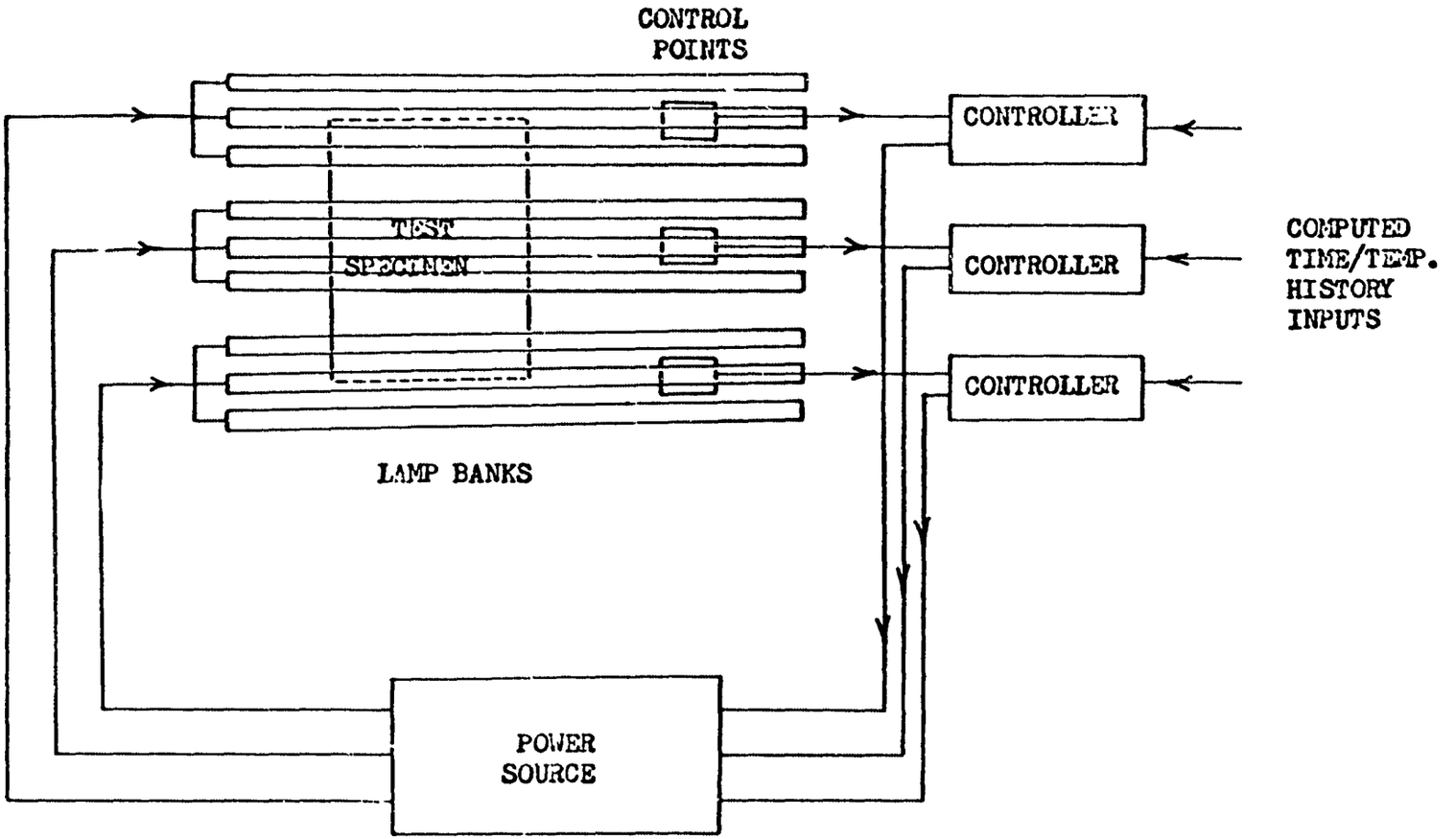

Figure 3

QUARTZ LAMP CONTROL DIAGRAM

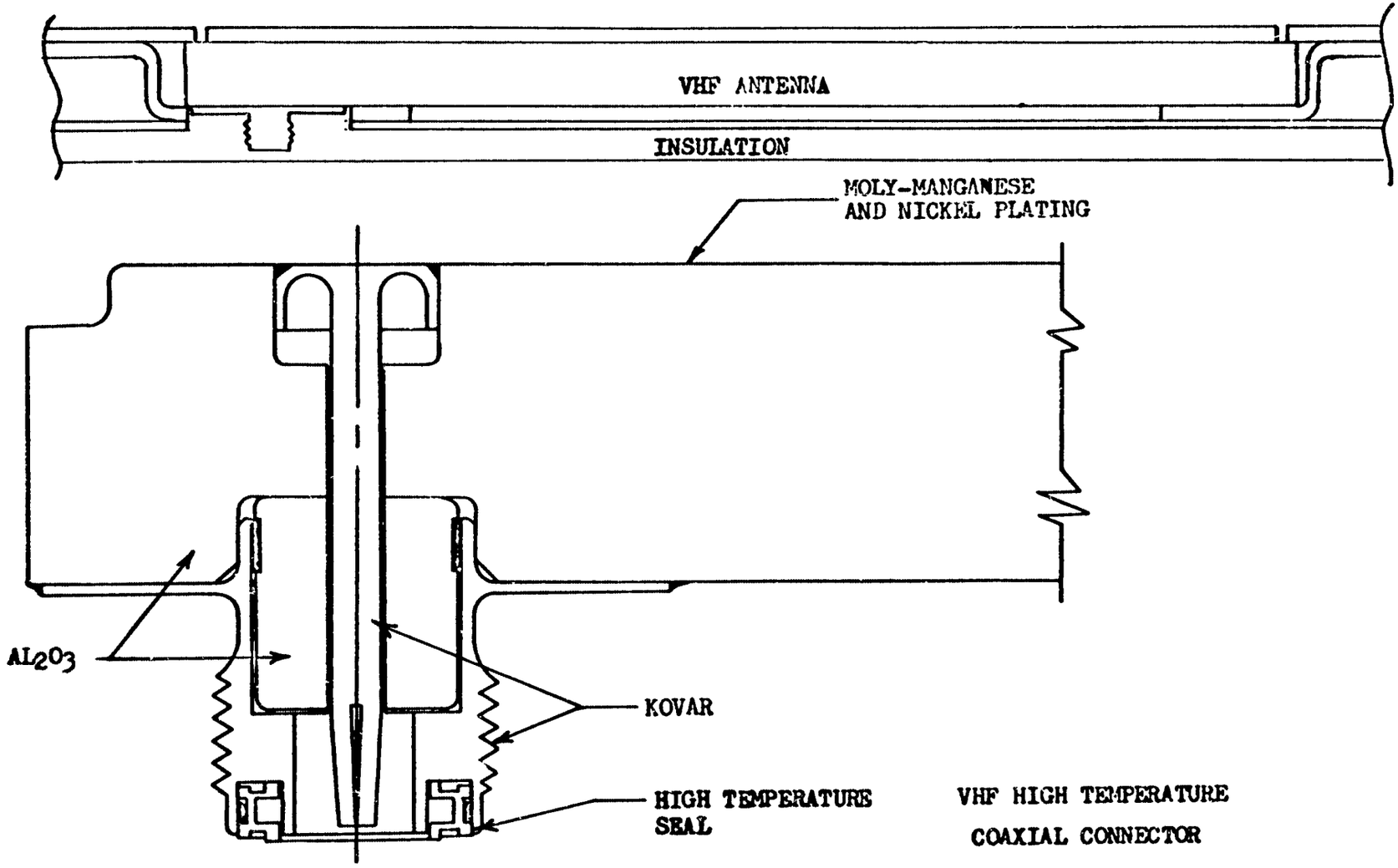

VHF HIGH TEMPERATURE
COAXIAL CONNECTOR

Figure 4

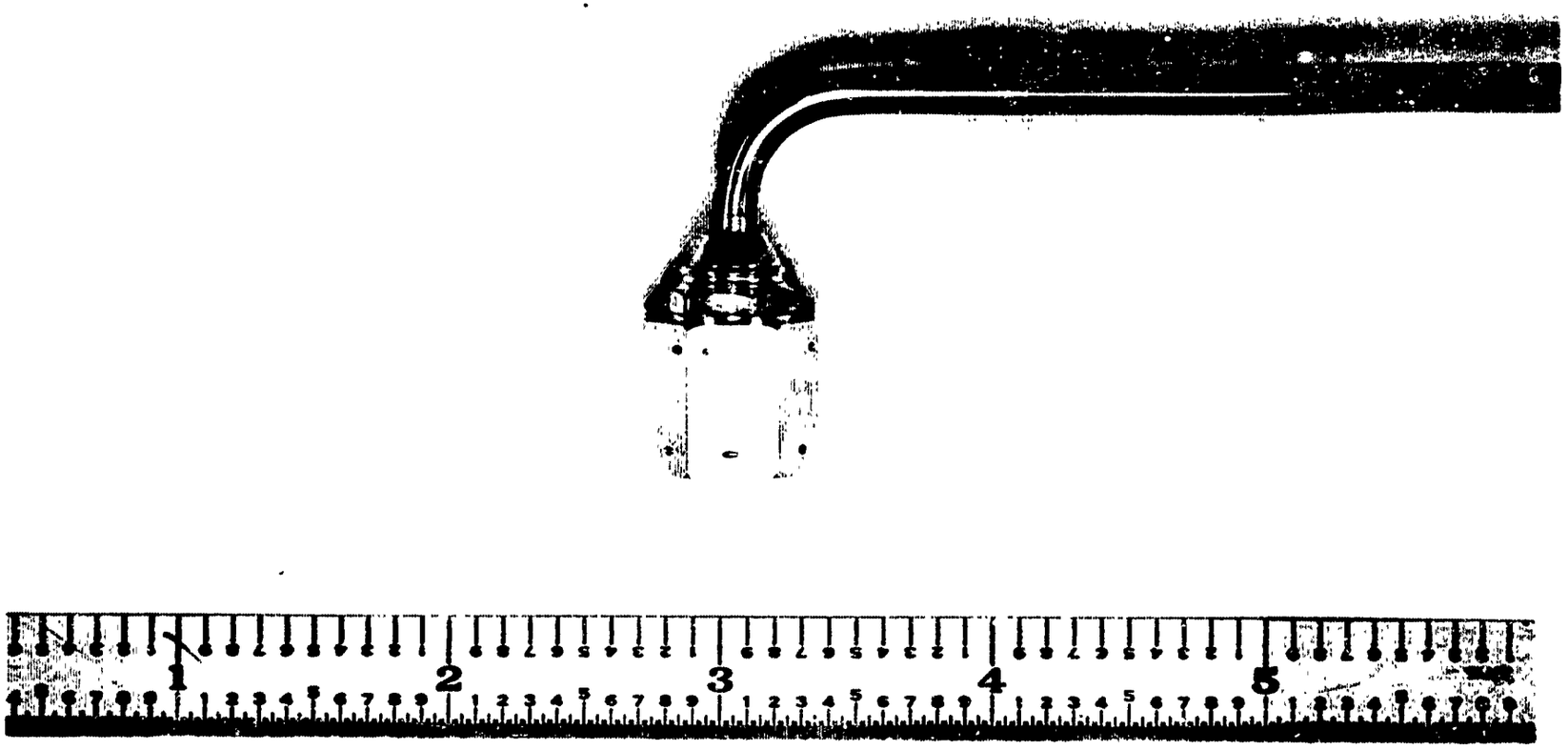

Figure 5

HIGH TEMPERATURE CAP

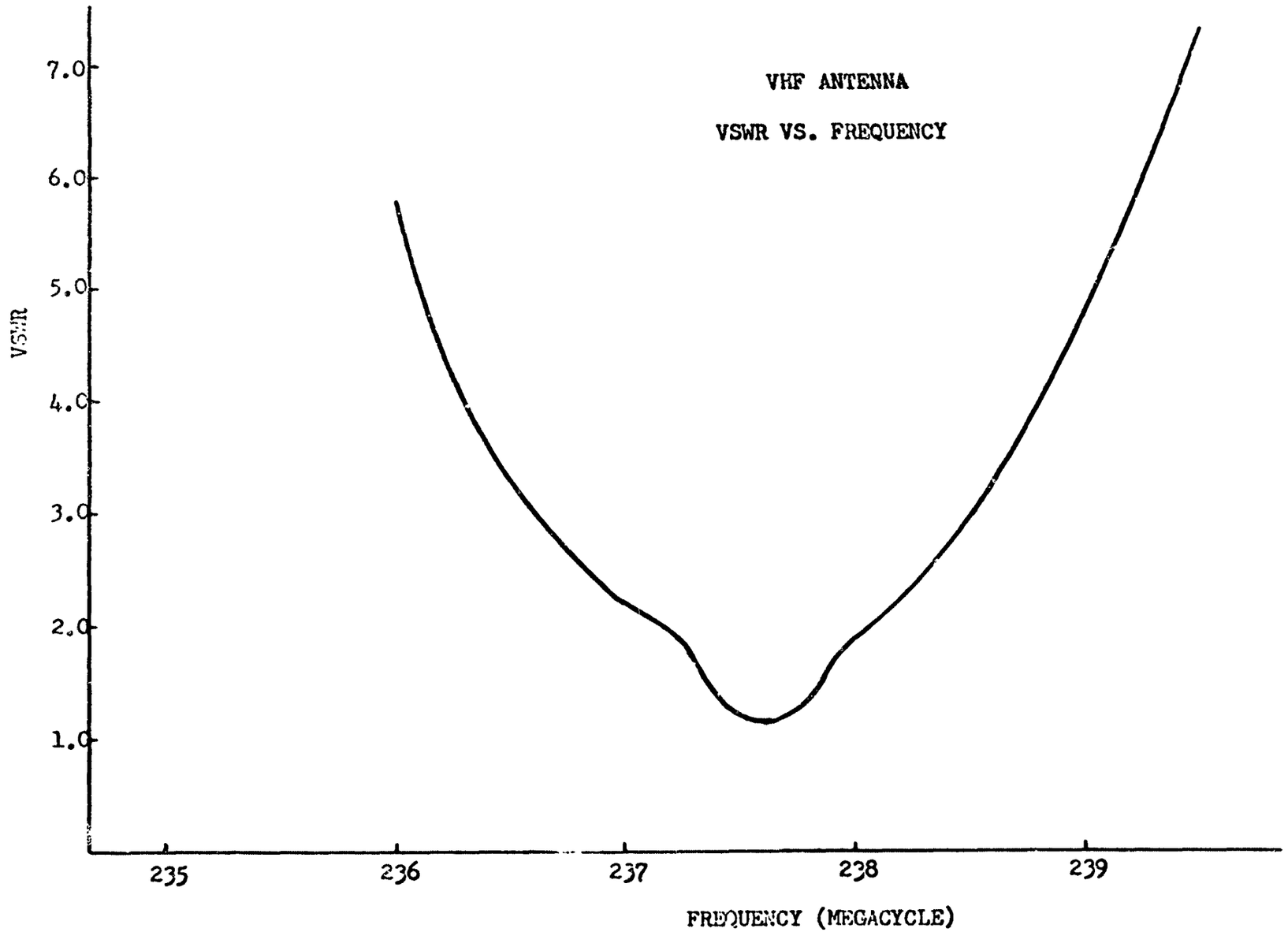
VHF ANTENNA
VSWR VS. FREQUENCY
VSWR
7.0
6.0
5.0
4.0
3.0
2.0
1.0
235
236
237
238
239
FREQUENCY (MEGACYCLE)

Figure 6

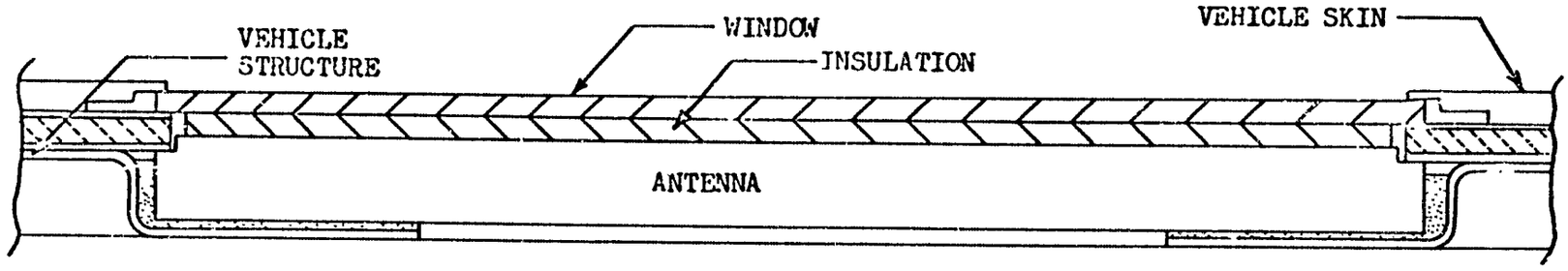

QUARTZ

A100

REFRASIL CLOTH

CS1000

VHF ANTENNA

INSTALLATION

Figure 7

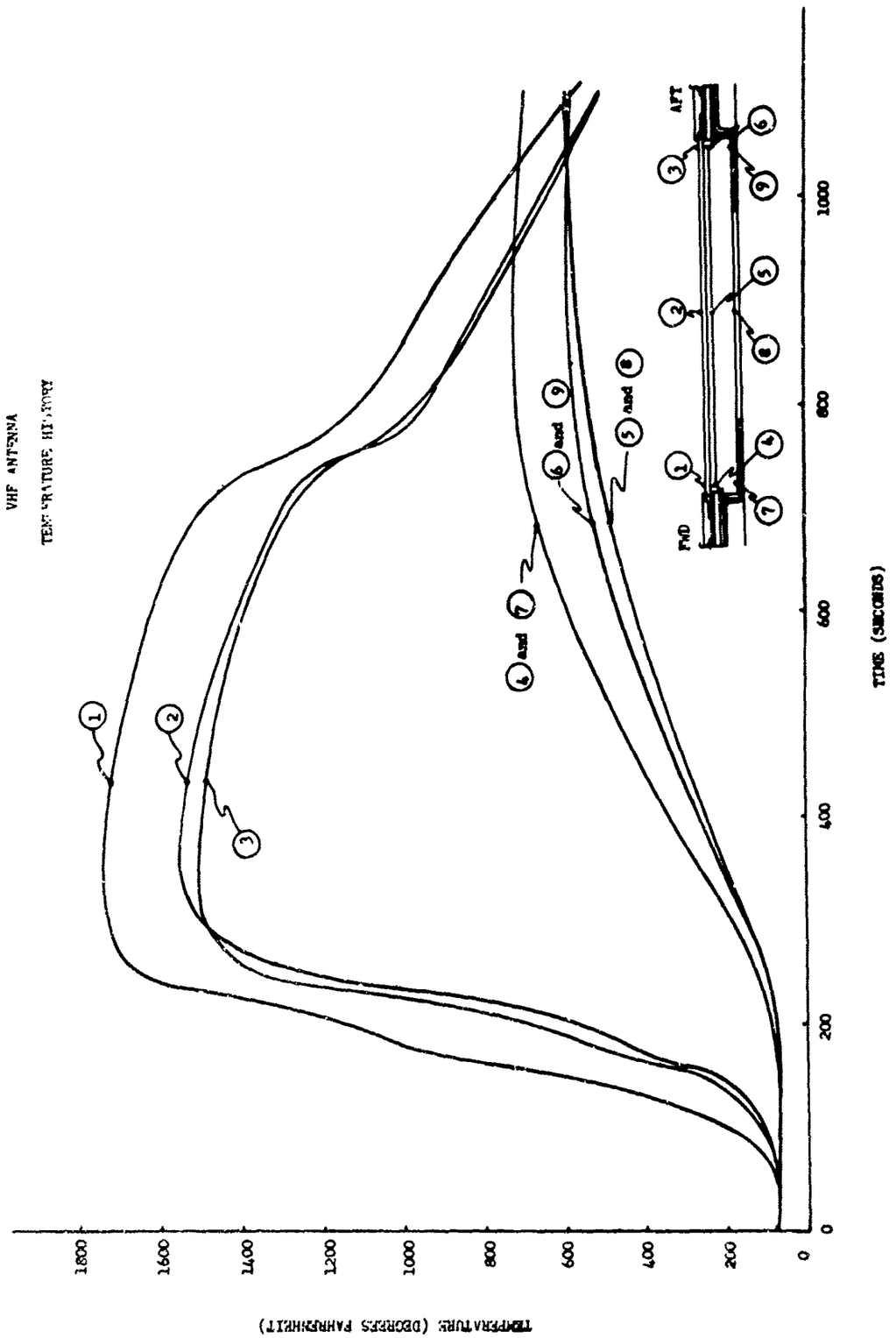
VHF ANTENNA
TEMPERATURE HISTORY
TEMPERATURE (DEGREES FAHRENHEIT)
TIME (SECONDS)
FWD
AFT
4 and 7
5 and 8
6 and 9

Figure 8

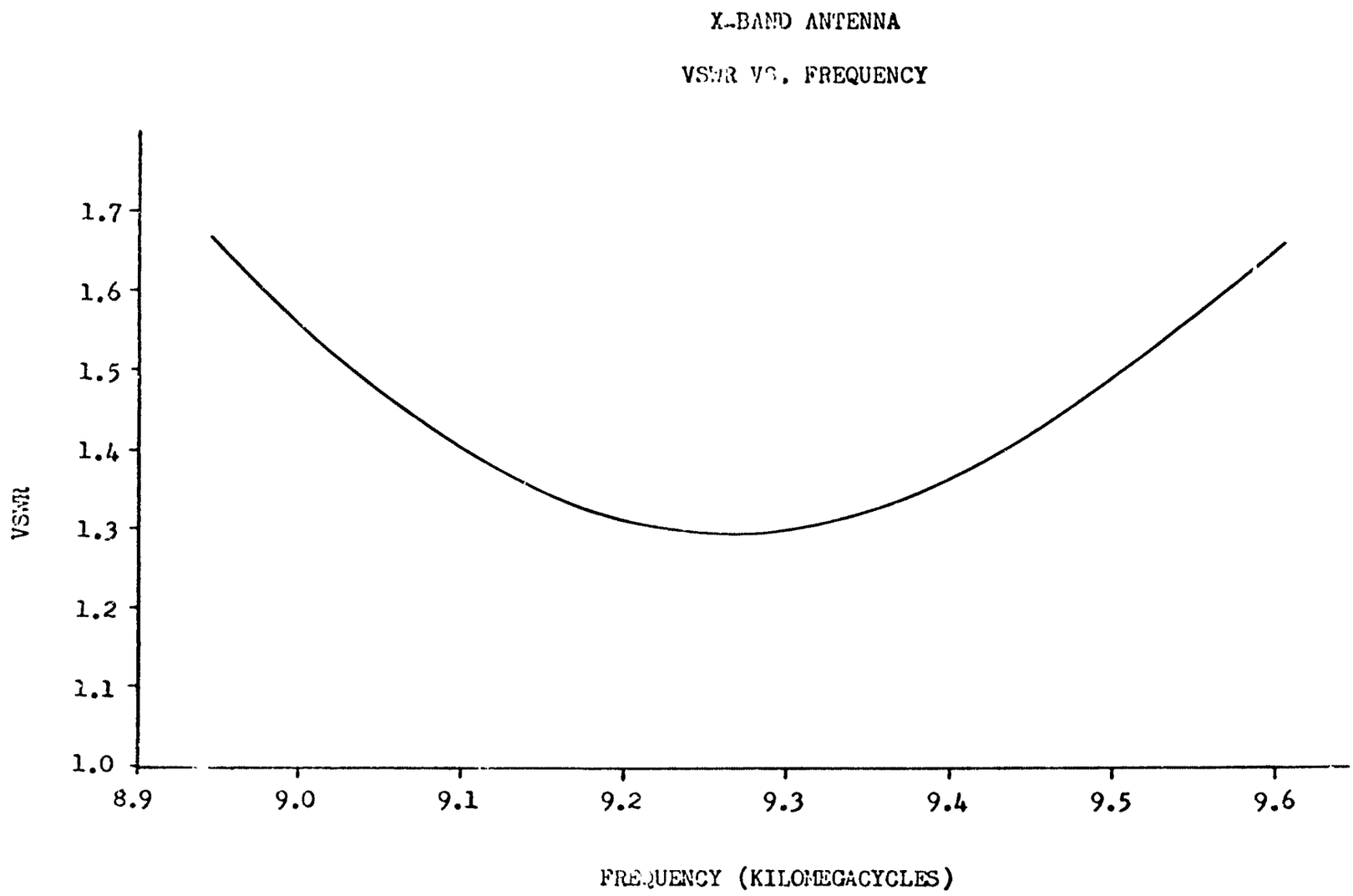
X-BAND ANTENNA
VSWR VS. FREQUENCY
VSWR
1.7
1.6
1.5
1.4
1.3
1.2
1.1
1.0
8.9
9.0
9.1
9.2
9.3
9.4
9.5
9.6
FREQUENCY (KILOMEGACYCLES)

Figure 9

X-BAND ANTENNA

CONSTRUCTION

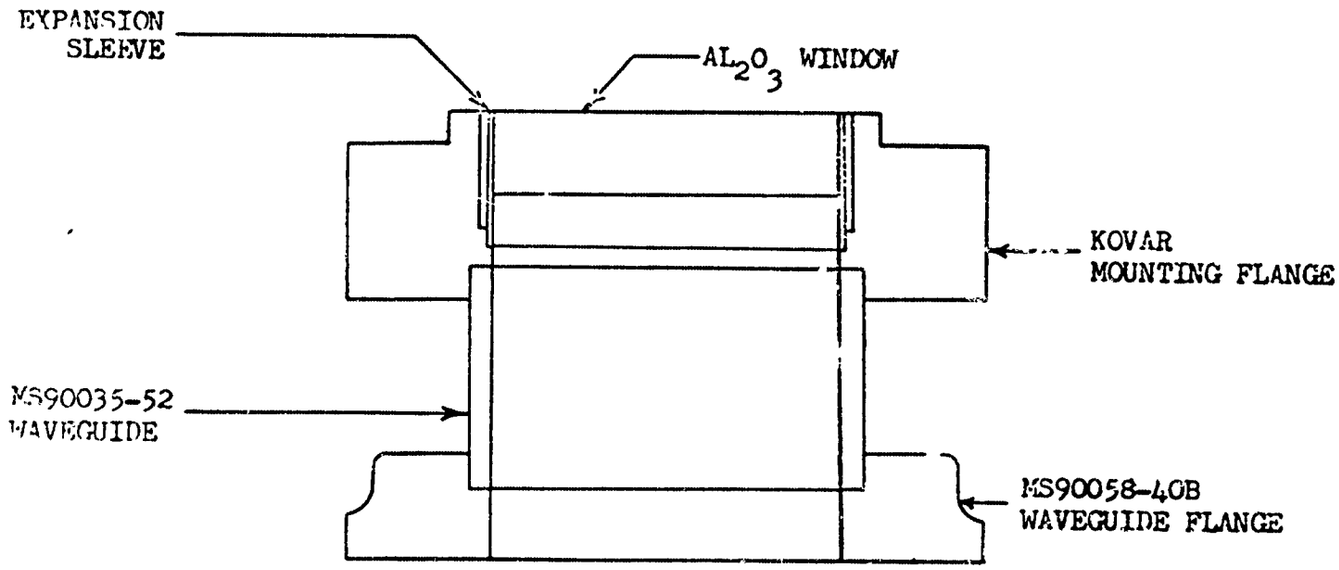

FIG-10

Figure 10

X-BAND ANTENNA

BRAZE MATERIALS

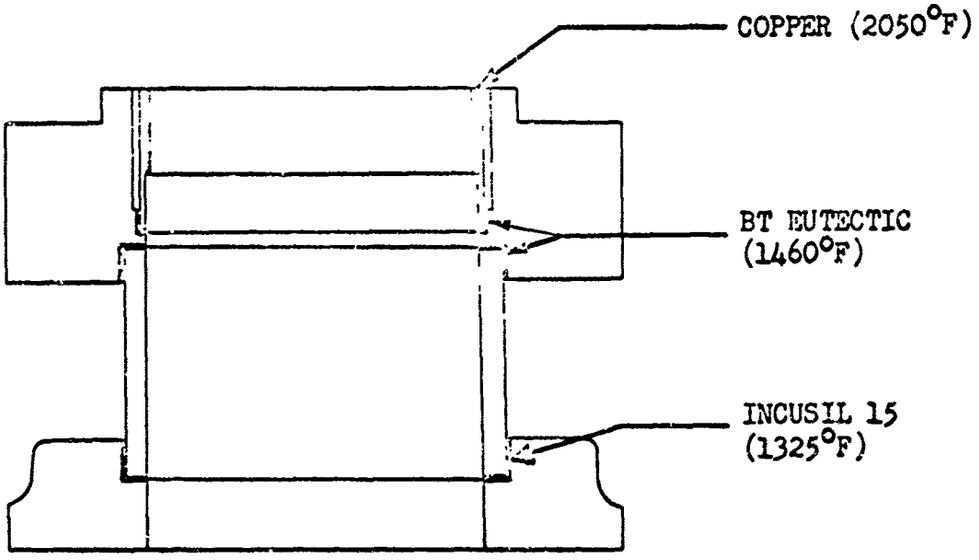

Figure 11

X-BAND ANTENNA
TEMPERATURE HISTORY
TEMPERATURE (DEGREES FAHRENHEIT)
0
200
400
600
800
1000
1200
1400
TIME (SECONDS)
0
100
200
300
400
500
600
700
800
900
1000
1100
1
2
3
4

Figure 12

RAIN EROSION RESISTANCE OF SLIP CAST FUSED SILICA RADOMES

by

R. L. HALLSE
Staff Scientest

and

R. A. FORTAIN
Design Engineer

GENERAL DYNAMICS/POMONA
Pomona, California

This program was funded under Contract No. Now 62-1087 #35 TOC

INTRODUCTION

Slip cast fused silica is currently being considered for missile radome applications. One of the major questions regarding this material's use as a radome has been its ability to withstand rain erosion or rain impact. For this reason rain environment tests were conducted at the Naval Ordnance Test Station (U.S. NOTS), China Lake, California, to determine the capability of the material to withstand rain environments when traveling at supersonic velocities.

PURPOSE

There are a number of factors that influence the rain erosion or rain impact resistance of a radome in a specified environment. The most important of these are: (1) Strength of material, (2) Hardness of material, (3) Surface finish, (4) Shape of radome, (5) Missile velocity, (6) Rain drop size, (7) Rain rate, and (8) Length of rain field. The objectives of this series of tests were (a) to determine the effectiveness of a plasma glazed surface as a protective coating on slip cast fused silica, (b) to compare the differences of a rounded nose vs. a pointed nose radome, and (c) to determine what effect a metal tip has on the ability of slip cast fused silica to withstand a rain environment. Thus the first four factors mentioned above were varied during the tests and the remaining four, which are a function of the particular test facility, were essentially held constant.

TEST FACILITY

The Supersonic Naval Ordnance Research Track (SNORT) at NOTS runs in a northerly direction for 21,500 feet. The first 2,000 feet is used for the sled acceleration phase, the next 2,500 feet is exposed to simulated rain fall while the remaining 17,000 feet are required to slow the vehicle to a stop. Plastic water bags are taped on the last 1,500 feet of the track to provide the necessary energy exchange to stop the sled completely. The curvature of the earth is taken into consideration by raising the track at one end by several inches. Earth's rotational effect is negligible and therefore omitted.

Artificial rain is created by sprinkler heads located five feet above and on the west side of the track. Sampling of the rain field area showed that the drop distribution was the same over the sampled area and corresponded to that occurring in two inches per hour of natural rainfall (See Figure 1). Since the track area is exposed to wind, tests are cancelled if there is a crosswind of five knots or more. Sandia Corporation has concluded that the average drop size in an average rain storm is 1.5 millimeters with a rate of fall of half inch per hour (227 drops per cubic foot). The artificial rainfall for these tests had an average drop size of 2.0 millimeters at a rate of 2 inches per hour.

The sled mounts two radomes and consists of streamline fairings back of the radomes. This provides aerodynamic stability and mounts a telemetering pack with a stub antenna. The sled is powered by two Cajun Rockets, each delivering 8,000 pounds of thrust. The test specimens are mounted at a zero angle of attack.

A dummy run was made on March 5, 1963 to obtain velocity curves for this series of tests (See Figure 2).

TEST SAMPLES

Four runs, consisting of two radomes each, were made during this series of tests. Six different radomes, all approximately 13 inches in length and 5.5 inches in diameter, were tested. Of the six radomes tested, five were fabricated as a joint project of the Ceramics Branch, Engineering Experiment Station, Georgia Institute of Technology, and General Dynamics/Pomona. Two of these radomes were run twice in order to determine the effect of a prolonged rain environment. The attachment method for these radomes consisted of a slotted aluminum ring having a 6° taper bonded into the radome by means of a room temperature cure epoxy adhesive (Shell 901/B1). Fiberglass insulation was then wrapped around the exposed aluminum in order to minimize the temperature of the attachment. This design is shown in Figure 3. The sixth radome was of high purity fused silica and was manufactured by Corning Glass Works, Corning, New York. The attachment consisted of a bonded nylon-phenolic ring overwrapped with fiberglass.

TEST RESULTS

The results of the four sled runs are summarized below:

Run #1 - (EAST) The test specimen was a rounded nose (1.12 inch diameter) radome in the "as cast" condition with a 0.350 inch wall. The thickness through the nose was 1.01 inches before the run. Approximately 0.40 inch of material was removed from the tip by the rain drops.

(WEST) The test specimen was a rounded nose radome that had been arc plasma glazed. The thickness through the nose was 0.87 inch before the test. The tip eroded back approximately 0.45 inch during the test.

Run #2 - (EAST) The test specimen was a pointed radome having a 0.350 inch wall and approximately a 1.5 inch thick nose. The entire surface was arc plasma glazed. The radome failed after traveling 200 feet through the rain field.

(WEST) The test specimen was a pointed "as cast" radome having a 0.350 inch wall and 1.50 inch tip. The tip eroded 0.60 inch during the run with minor

damage being evidenced to a point 4.5 inches aft of the tip. The radome was returned to GD/P where a steel tip, 0.90 inch in length and 0.70 inch in diameter was bonded to the radome.

Run #3 - (EAST) The test specimen was the reworked radome from Run #2 with the steel tip. The only visual damage was a very small increase in erosion aft of steel tip.

(WEST) The test specimen was a pointed radome that had its forward end plasma glazed. This item was 0.350 inch thick and had a 1.50 inch nose. There was no significant erosion on the test piece. The tip had eroded 0.10 inch with a few pits from 3 to 6 inches aft.

Run #4 - (EAST) The test specimen was a Corning Glass Works Multiform Fused Silica #7941 with a very deep glaze and wall of 0.250 inch. The radome failed in 1,000 feet of rain (station 3,000). Pieces were found at station 3,175.

(WEST) The test specimen was a pointed partially glazed radome that had survived run #3. Erosion was increased by 0.25 inch, resulting in total erosion for the two runs of 0.45 inch.

Photographs of the fused silica radomes before and after exposure to the rain field are shown in Figures 4 through 23, together with synchroballistic camera shots taken at 1975', 3175' and 4500', which are stations immediately before the rain field, approximately in the center of the rain field, and just past the rain field, respectively.

These photographs, together with the location along the track where debris was found, give a good indication as to where radome failure occurred. They also provide an insight into the rate of material erosion. For example, careful inspection of Figure 5 shows that most of the total erosion took place between 3175' and 4500'. This indicates that when erosion once starts it progresses quite rapidly. Figure 10 shows a similar effect with the pointed unglazed radome and also shows that the pointed glazed radome failed in the first half of the rain field. Figure 20 again demonstrates that most of the erosion occurs during the last half of the runs and also shows that the Corning radome failed in the rain field prior to 3175'.

DISCUSSION

In general, the rain erosion results on slip cast fused silica were quite encouraging. The effects of two important parameters, namely glazing and specimen geometry, were determined. In addition, the tests proved that the material is structurally adequate to withstand high vibrations (up to approximately 100g's) and that the bonded attachment used is satisfactory.

Perhaps the most significant factor learned from the tests was the great importance of specimen geomtry. Both radomes on run #1 had rounded noses and both encountered considerable erosion in the nose area. Approximately 0.50 inch of material was eroded from the nose of each radome irrespective of the surface finish (glazed or unglazed).

Significant improvement was found with the pointed radomes and in this case the surface condition did appear to be important. Whereas the pointed unglazed radome eroded back to a 0.50 inch diameter, the glazed radome underwent erosion of

less than 0.12 inch on the tip. When run for a second time, the latter radome eroded back to a 0.37 inch diameter. This demonstrated again that a point is very desirable from a rain erosion standpoint.

The unglazed pointed radome from run #2 was run again in run #3 after a steel tip had been added to it. The radome itself was prepared for the addition of the tip by sawing off the partially eroded tip at a diameter of 0.70 inch. The steel tip, having a base diameter of 0.70 inch and a height of 0.875 inch was bonded to the radome by means of an epoxy (Shell 901/B1). Very little, if any, additional erosion took place during the second run. It appears therefore that the addition of a metal or dense ceramic tip to a slip cast fused silica radome could be quite helpful, although not necessary, from a rain erosion standpoint.

Another interesting fact that was determined as a result of these tests is that unlike most brittle ceramic materials, slip cast fused silica can undergo considerable erosion without failing catastrophically. It is felt that the reason for this is the 10 - 14% porosity present in the fused silica. This porosity provides a means of stopping a crack that is propagating through the material as a result of rain impact. In a ceramic material of essentially theoretical density there is no provision to inhibit crack propagation once a crack has been initiated, and catastrophic failure results. The inherent porosity of slip cast fused silica is thus seen as a benefit from the standpoint of impact resistance.

CONCLUSIONS

As a result of these tests several conclusions can be drawn regarding the behavior of slip cast fused silica in a rain environment.

1. Slip cast fused silica will erode without undergoing catastrophic failure.

2. Glazing improves the rain erosion resistance of pointed slip cast fused silica radomes.

3. The erosion rate is affected greatly by specimen geometry, with pointed radomes showing the least erosion.

4. Erosion can be minimized by the use of a small metal or dense ceramic tip.

5. Slip cast fused silica has sufficient strength to withstand the vibration, accelerations and accoustics of a missile flight and launch.

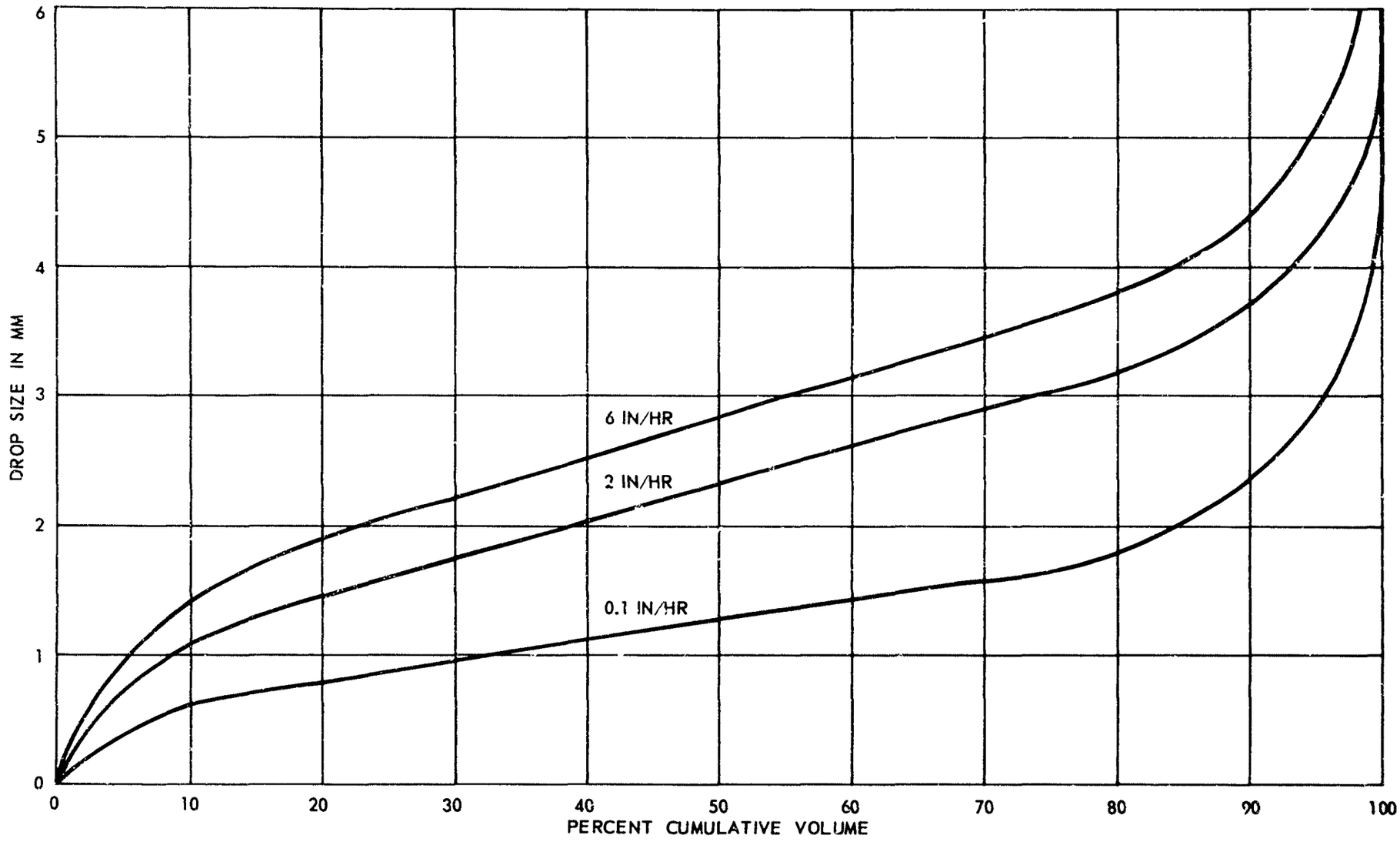

FIGURE 1 - Natural Rainfall Distribution

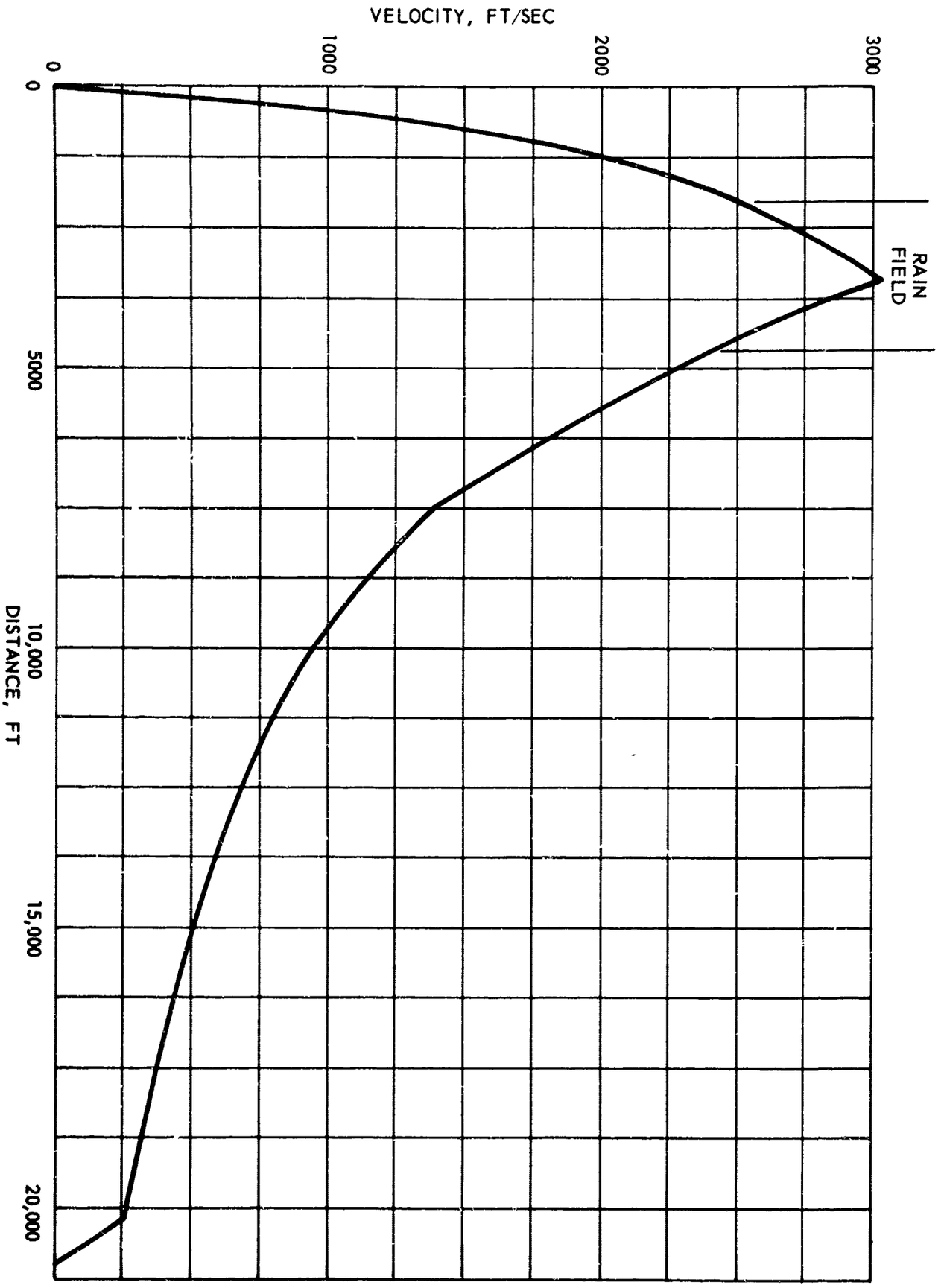

FIGURE 2 - Dummy Run of Rain Sled

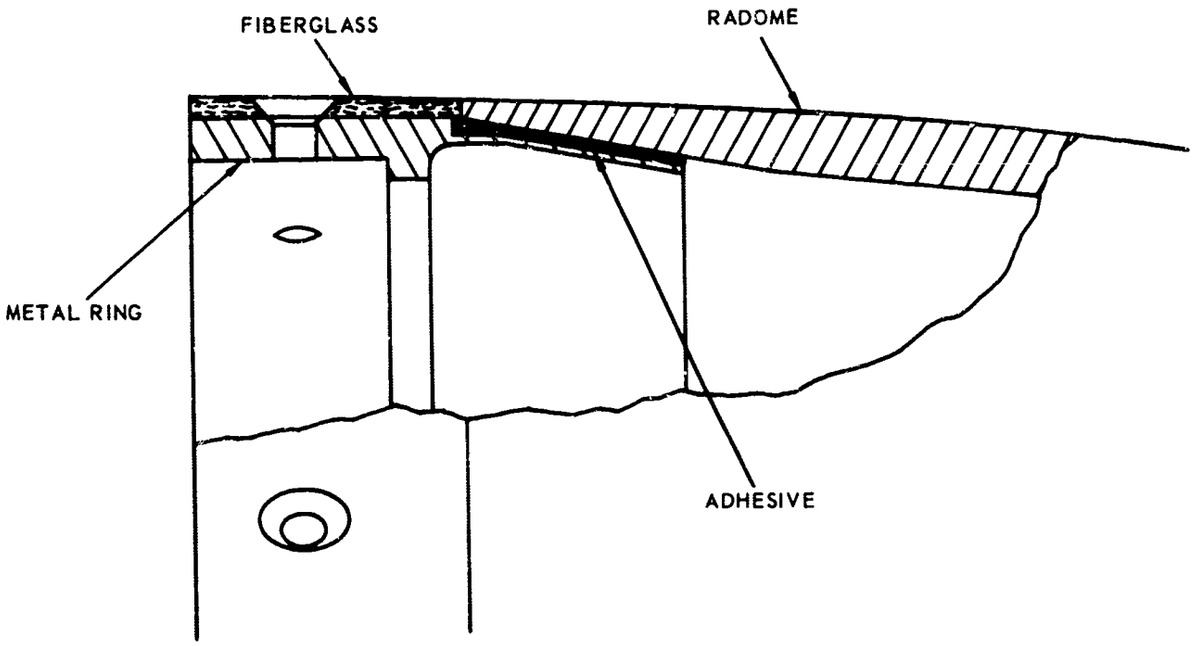

FIGURE 3 - Ring Attachment

Figure 7 - Hypersonic Shock Tunnel Model Before Run #1

Figure 8 - Hypersonic Shock Tunnel Model Before Run #4

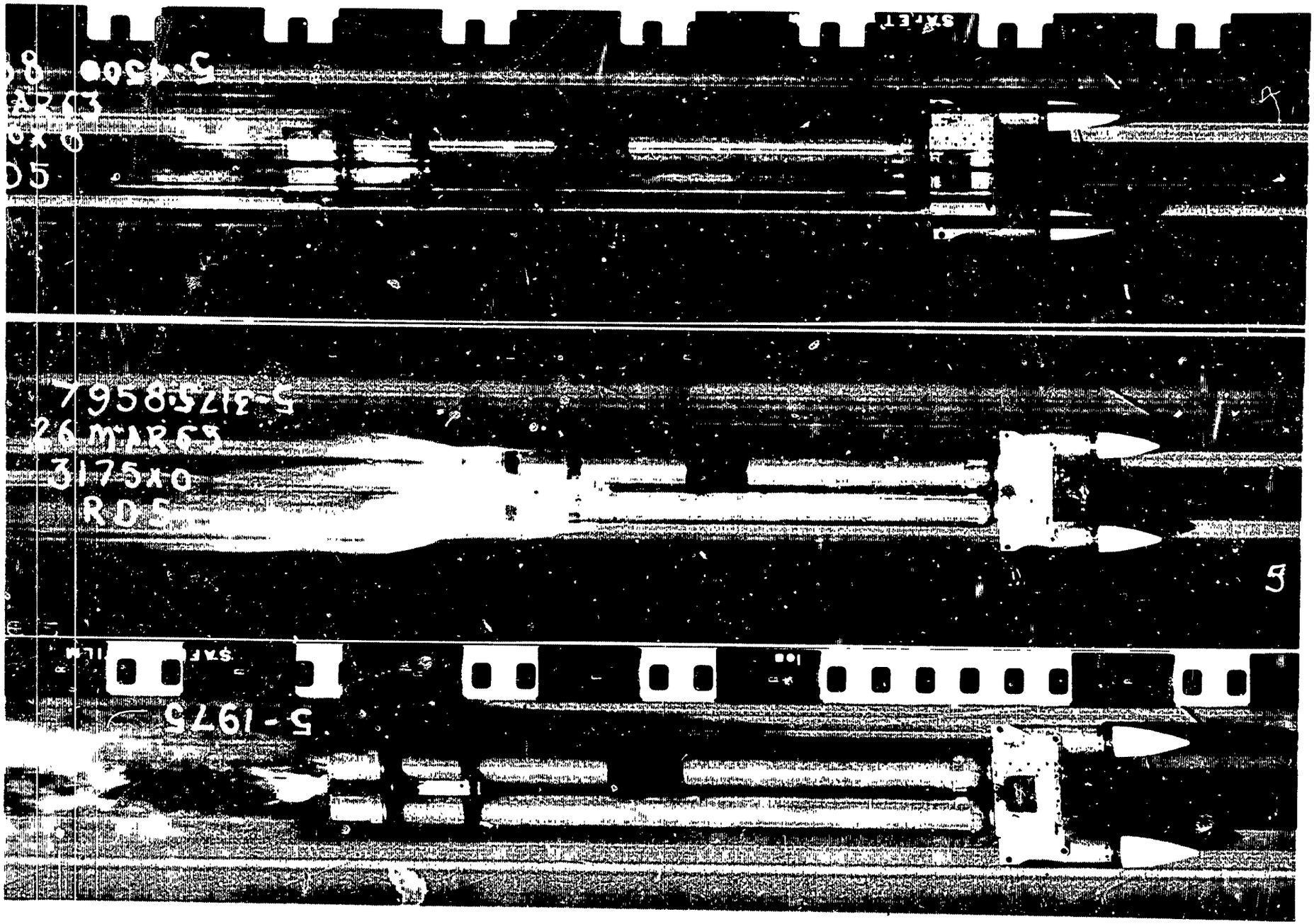

FIGURE 5 - Synchroballistic Camera Shots of Run #1

FIGURE 7 - Closeup of Unglazed Radome After Run #1

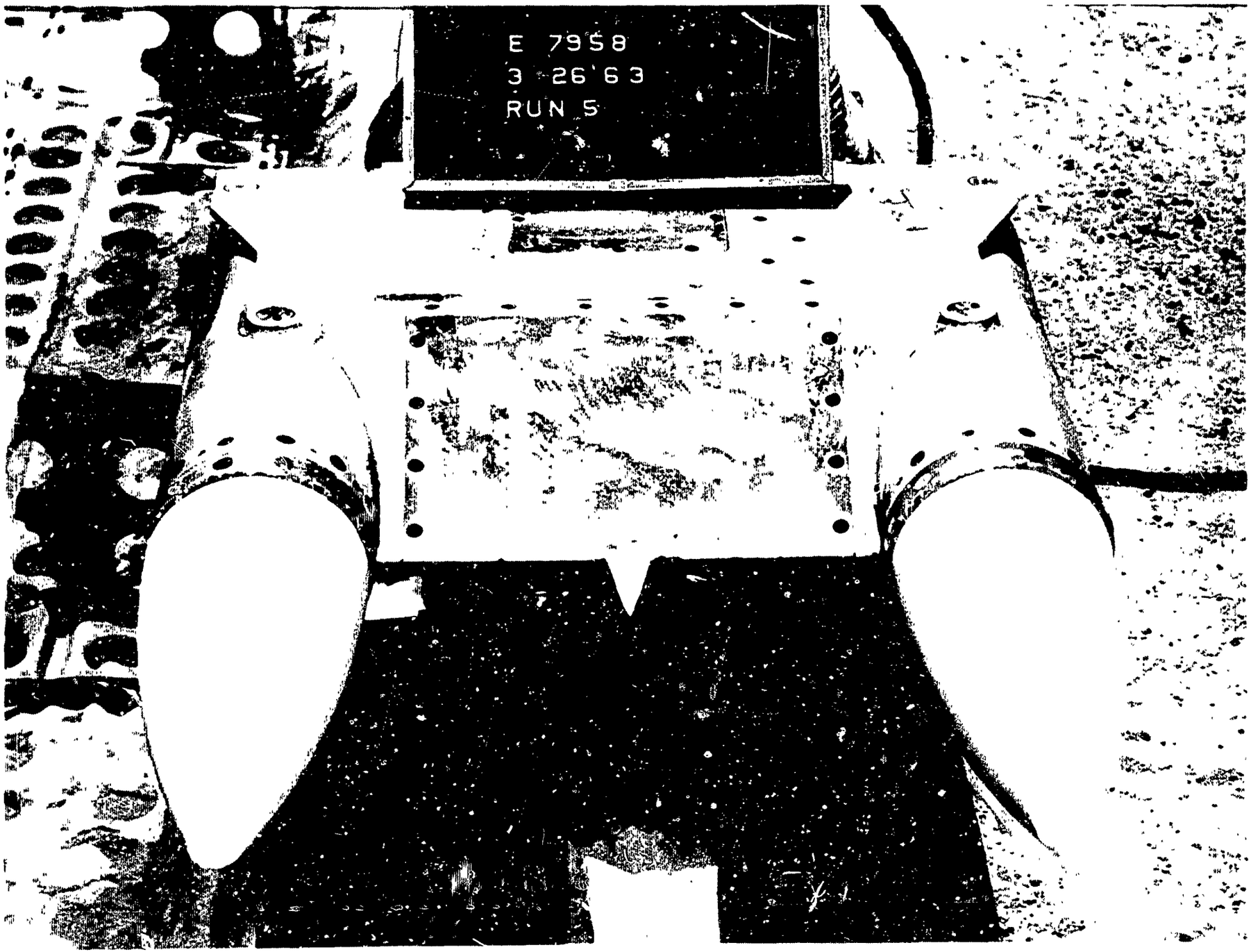

5 R

FIGURE 9 - Pointed Glazed and Unglazed Radomes Before Run #2

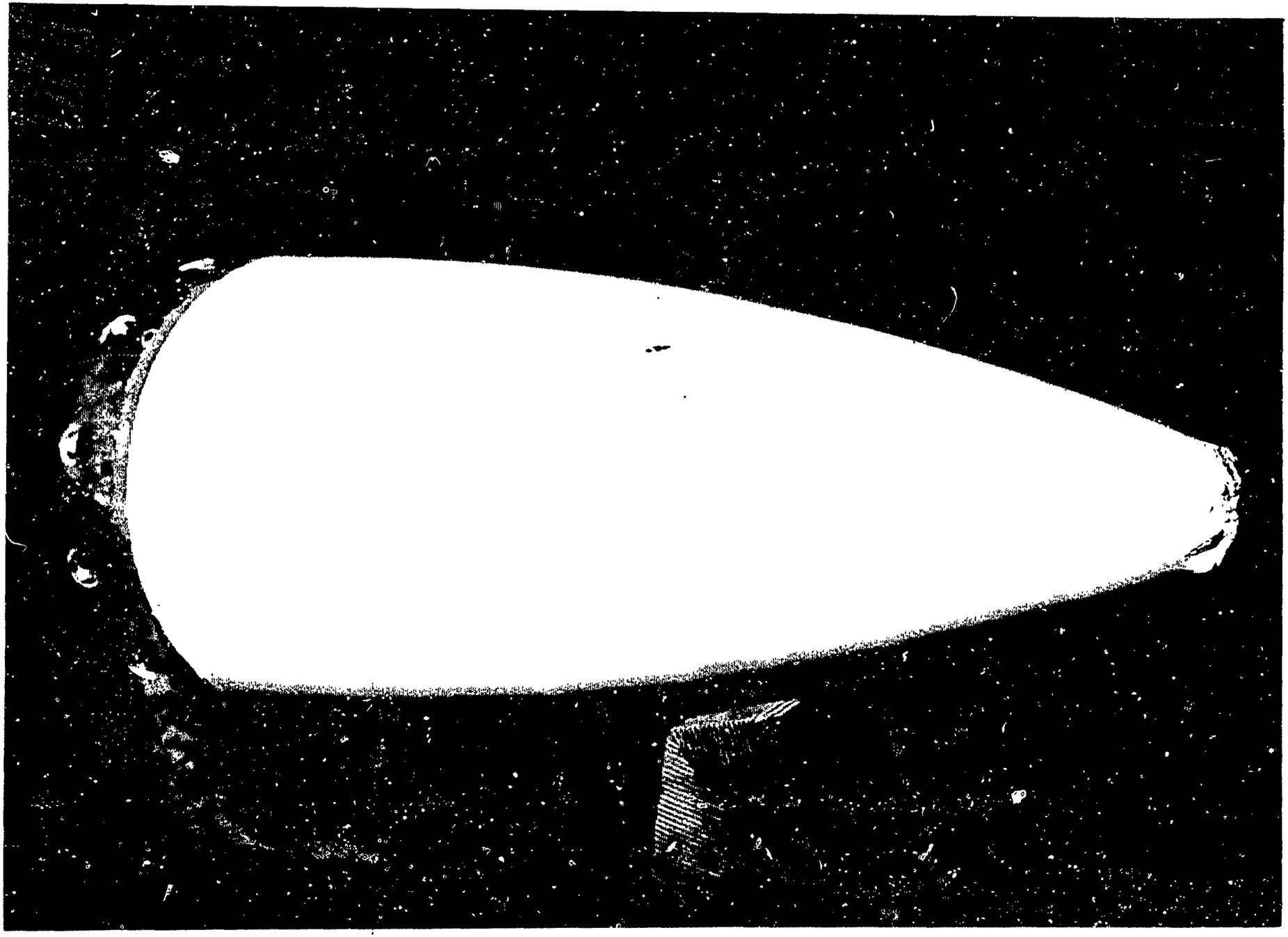

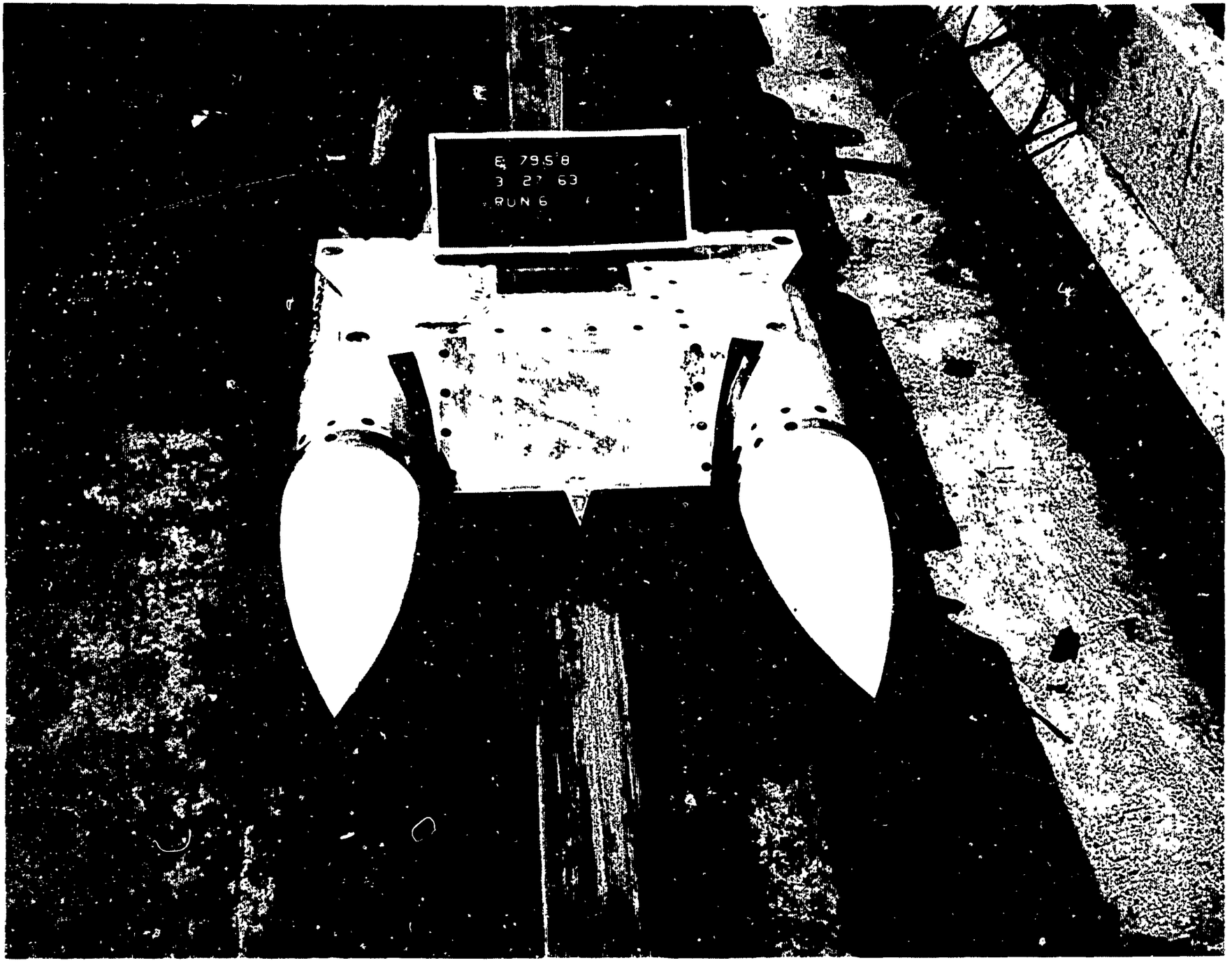
E 79.5'8
3 27 63
RUN 6

FIGURE 11 - Pointed Unglazed Radome and Attachment Ring of Glazed Radome After Run #2

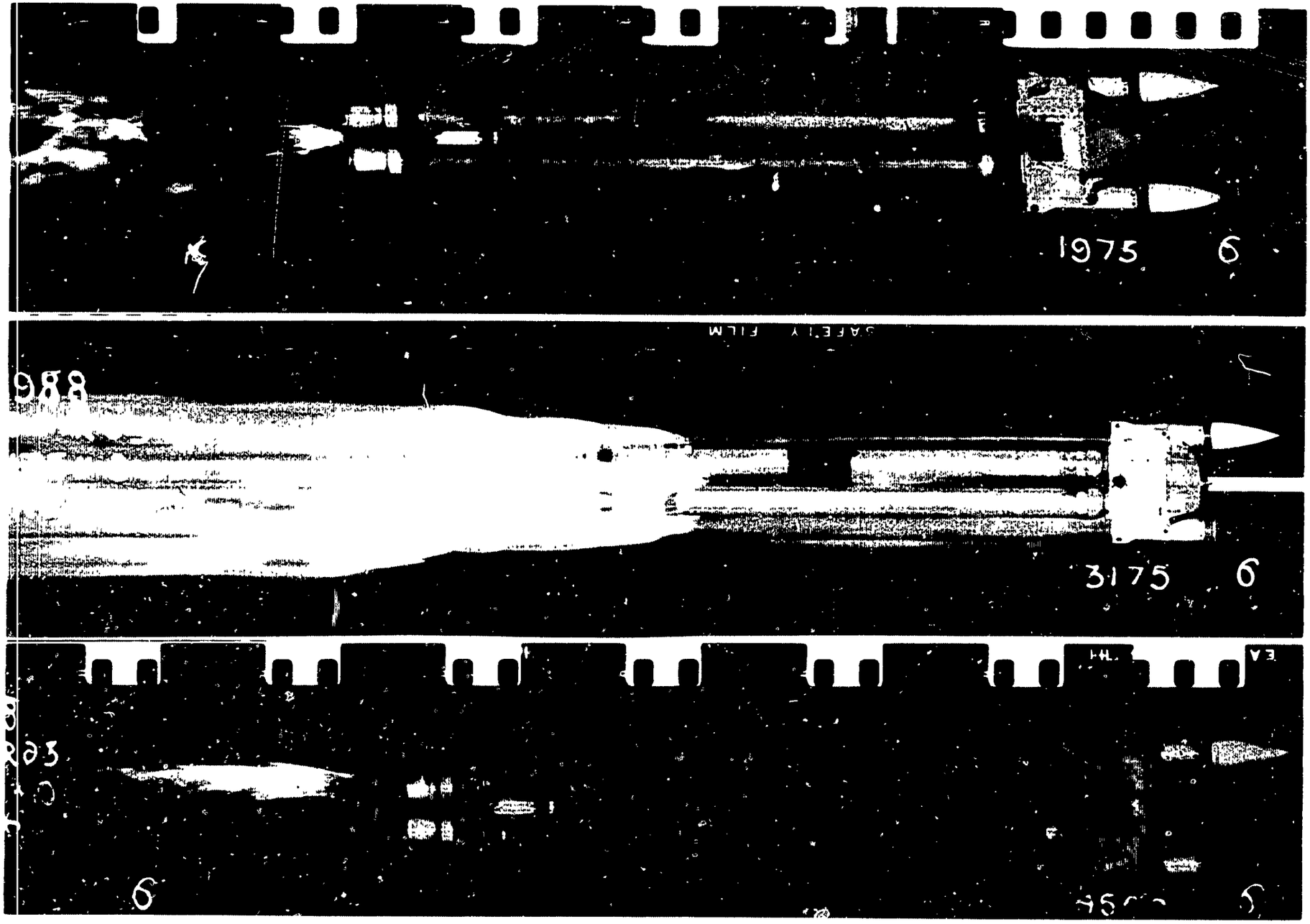

FIGURE 10 - Synchroballistic Camera Shots of Run #2

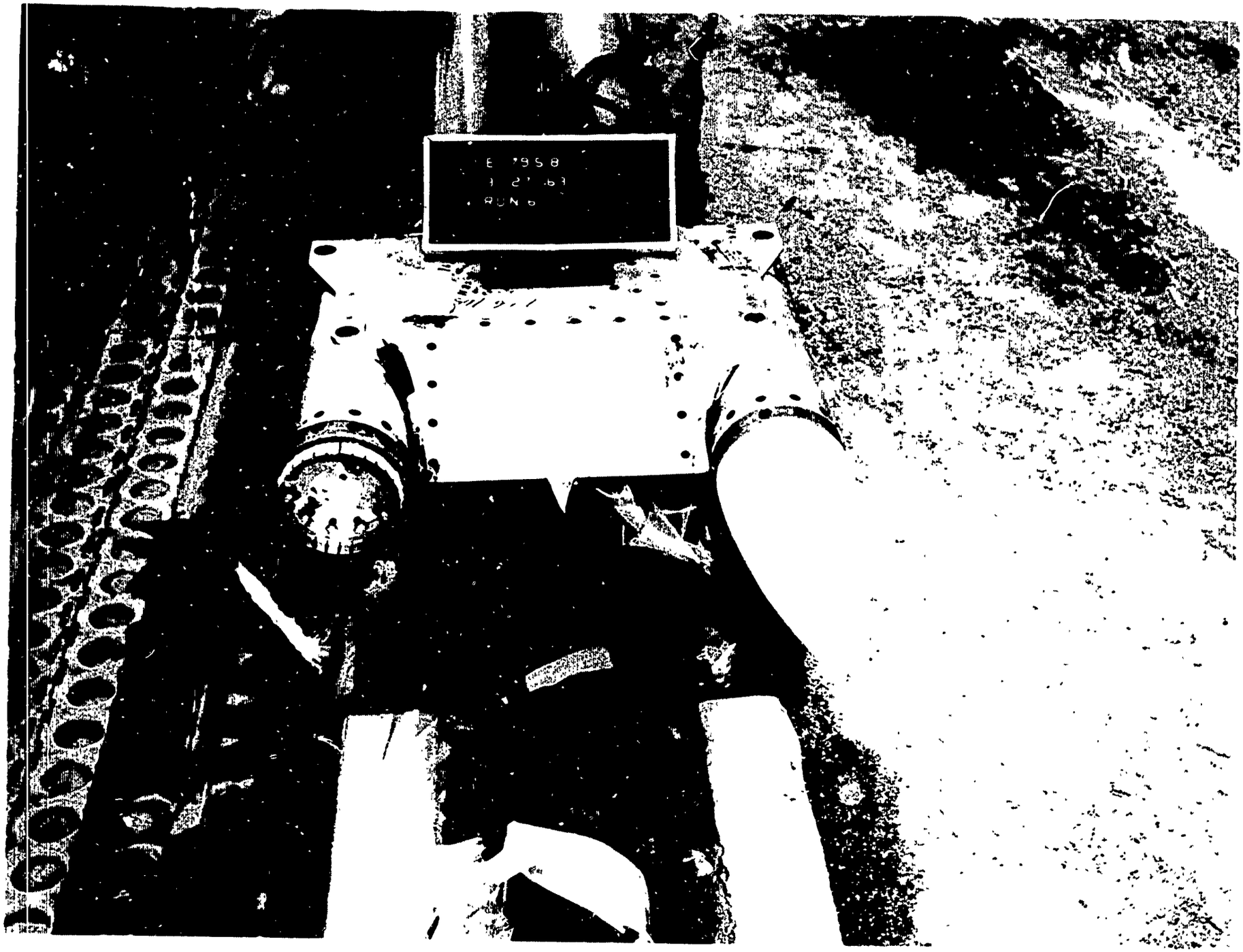

FIGURE 11 - Pointed Unglazed Radome and Attachment Ring of Glazed Radome

FIGURE 13 - Attachment Ring From Gl.. ed Radome After Run #2

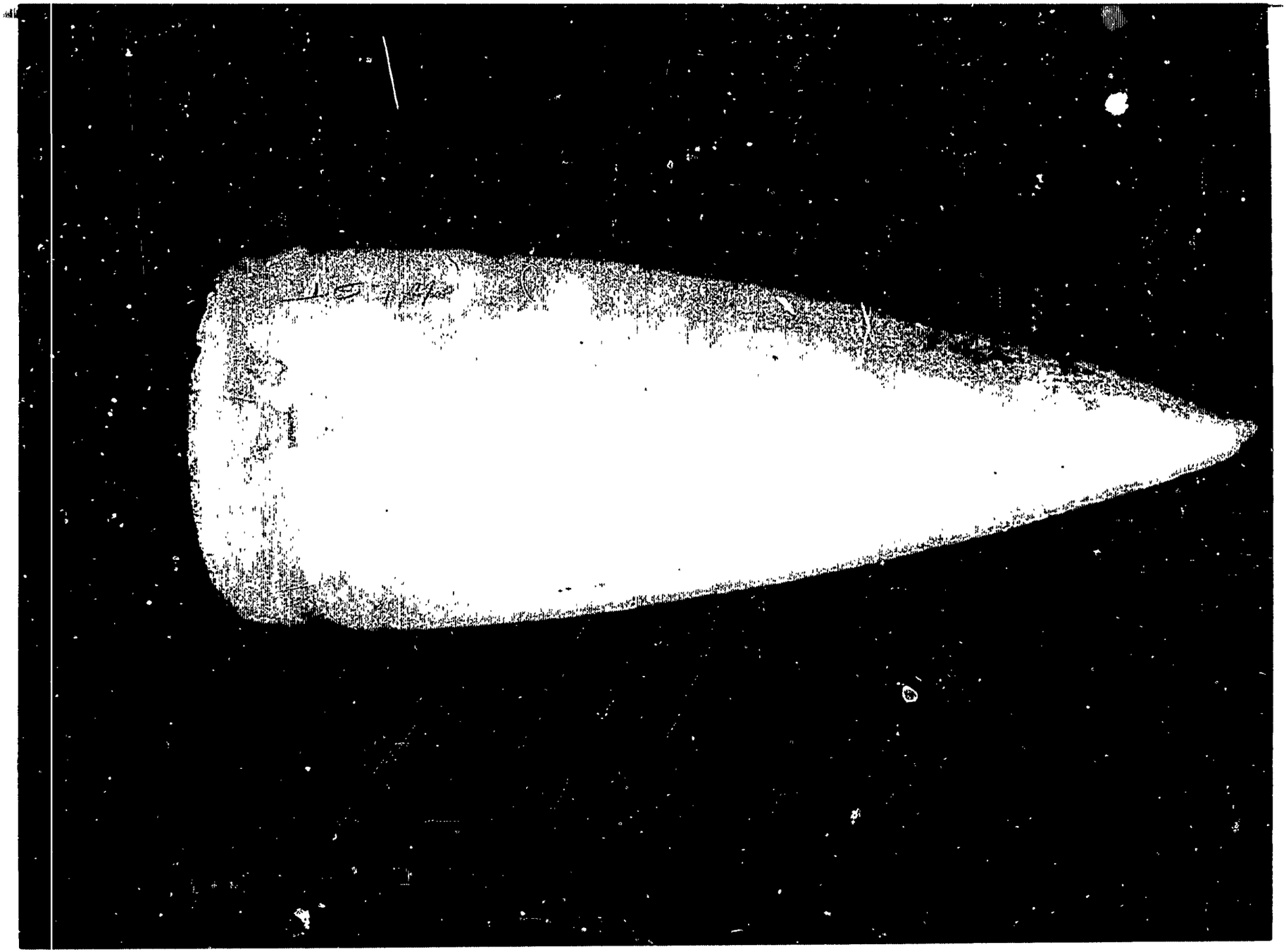

FIGURE 12 - Closeup of Unglazed Radome After Run #2

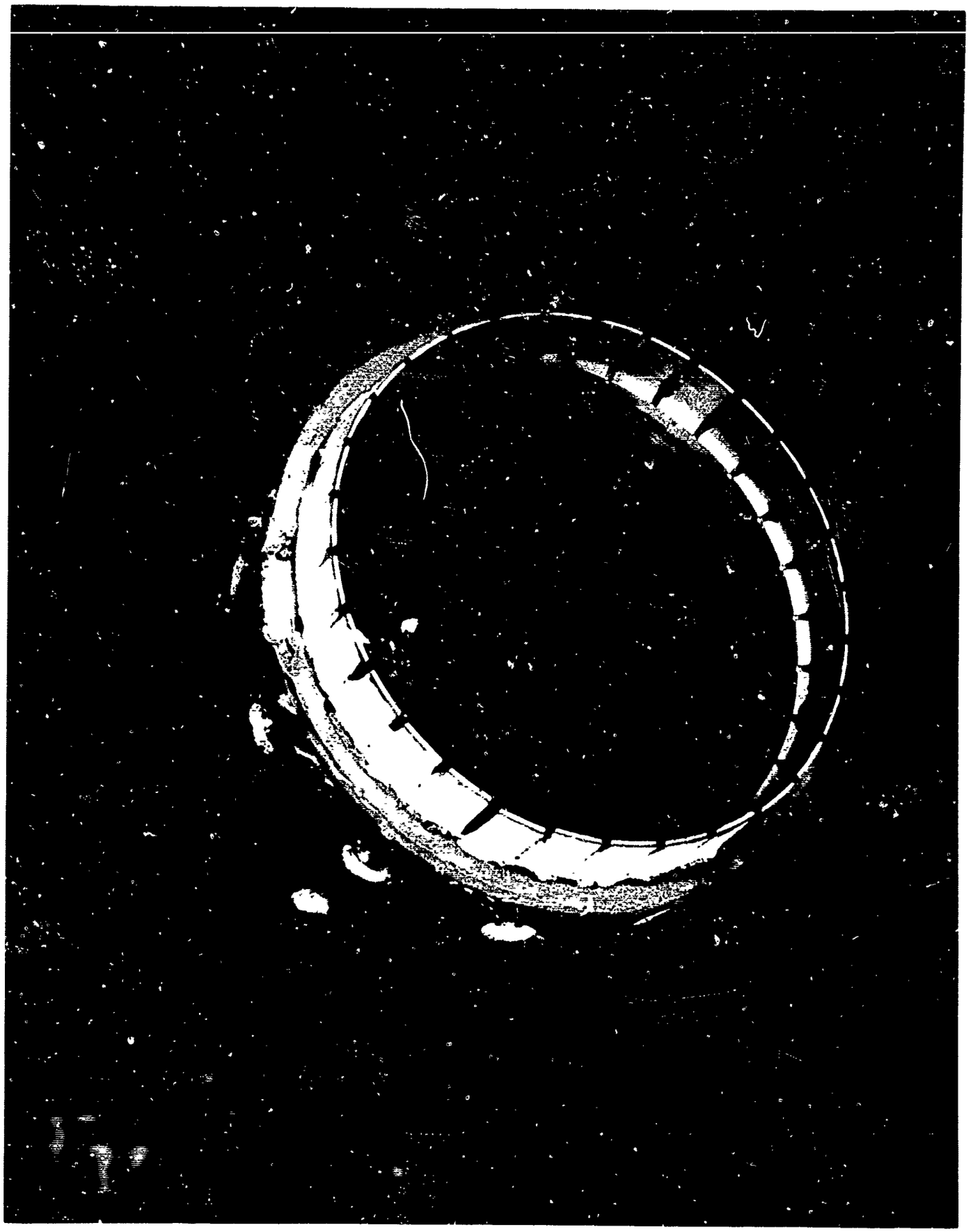

FIGURE 15 - Synchroballistic Camera Shots of Run #3

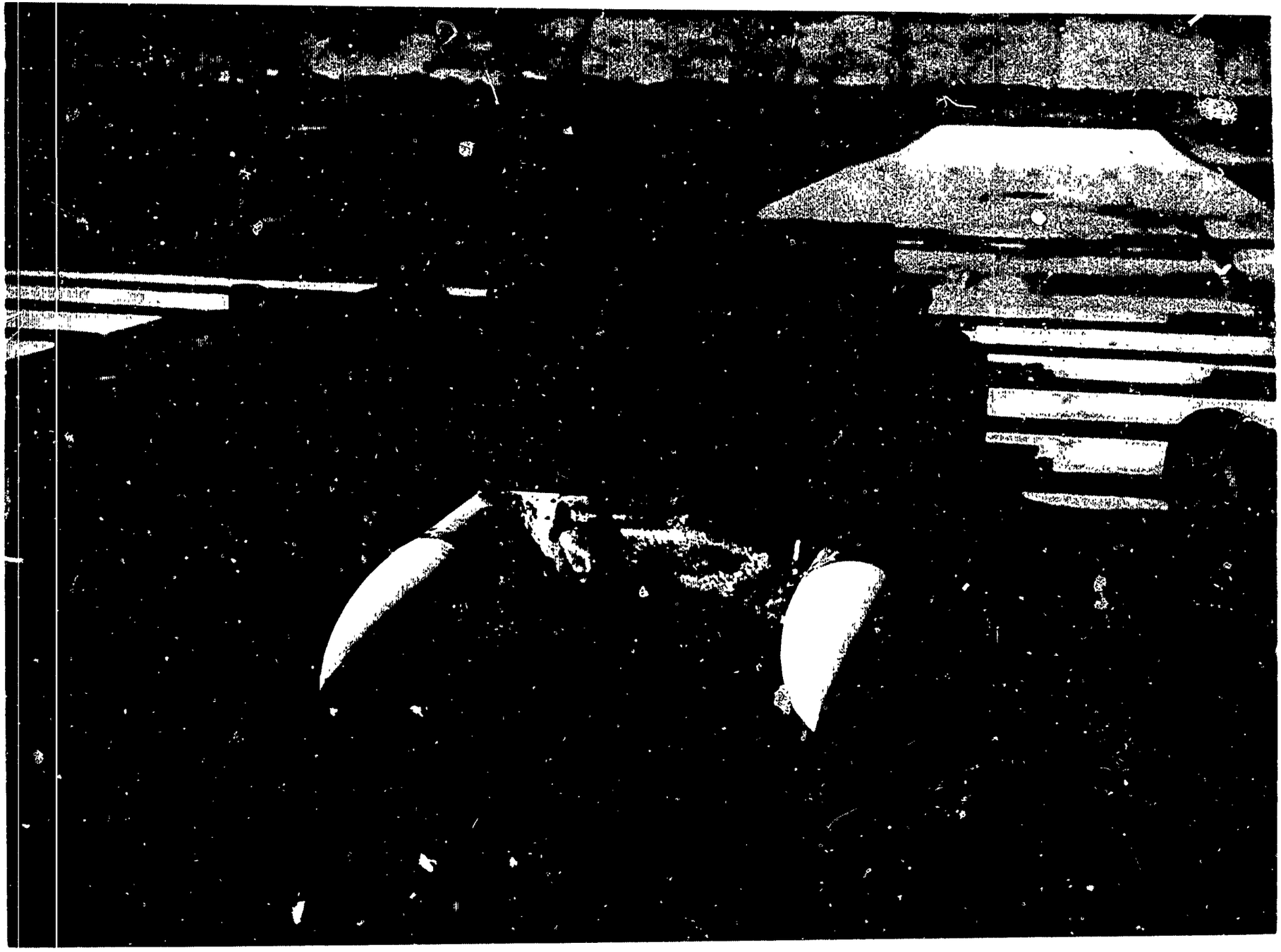

FIGURE 14 - Pointed, Tip Glazed and Steel Tipped Radomes Before Run #3

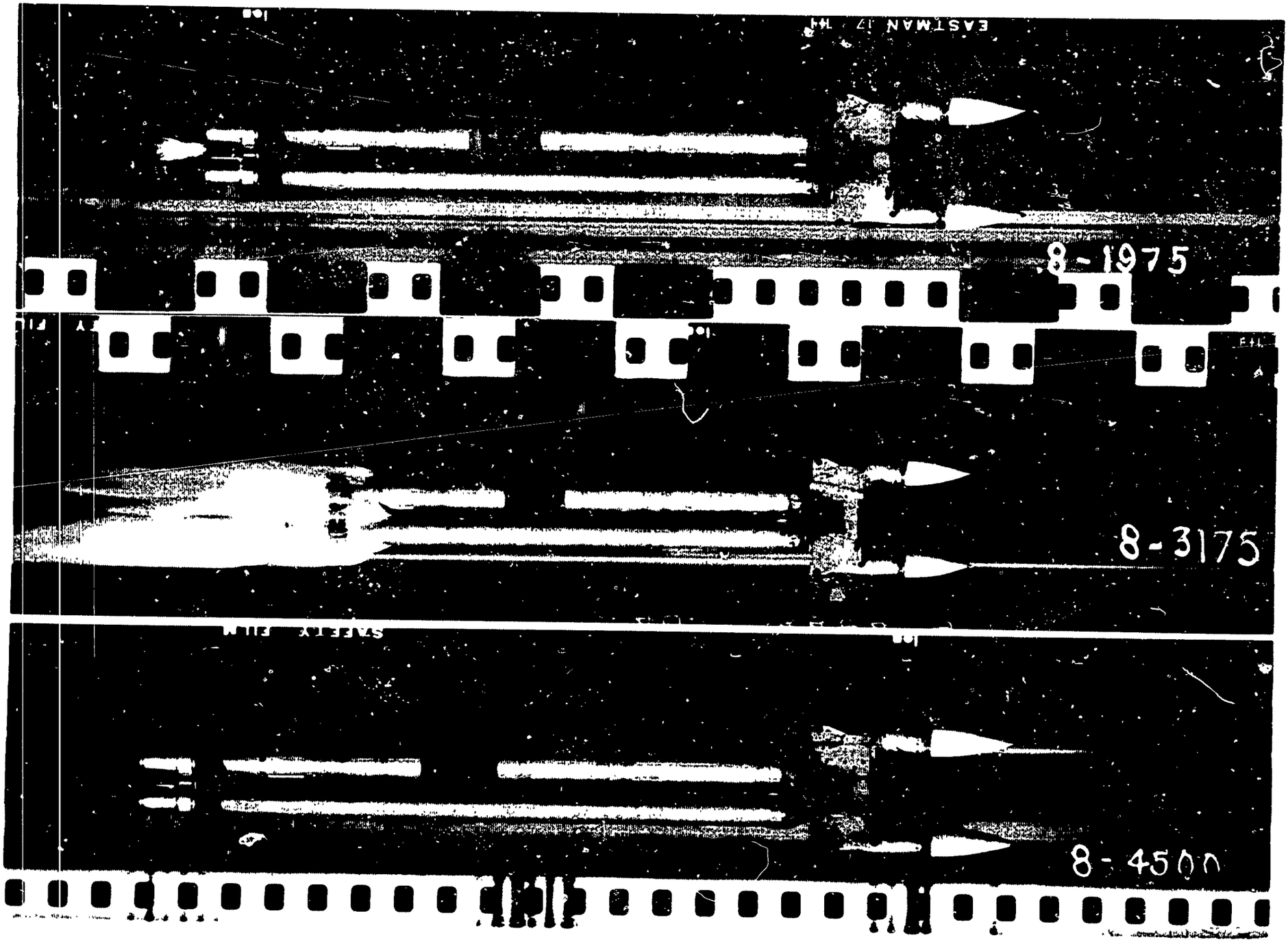

FIGURE 15 - Synchroballistic Camera Shots of Run #3

FIGURE 17 - Closeup of Pointed, Tip Glazed Radome After Run #3

FIGURE 16 - Pointed Radomes After Run #3

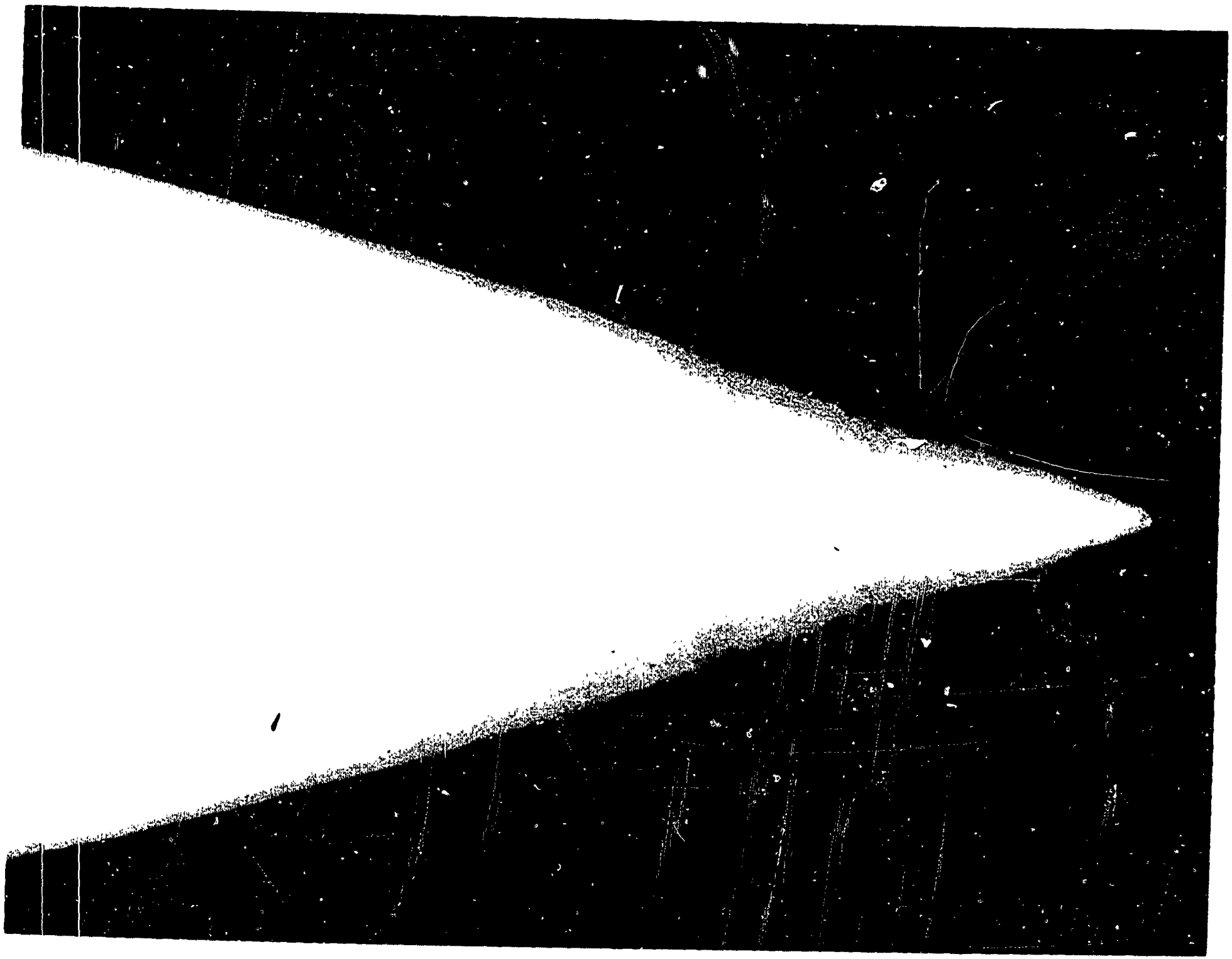

FIGURE 17 - Closeup of Pointed, Tip Glazed Radome After Run #2

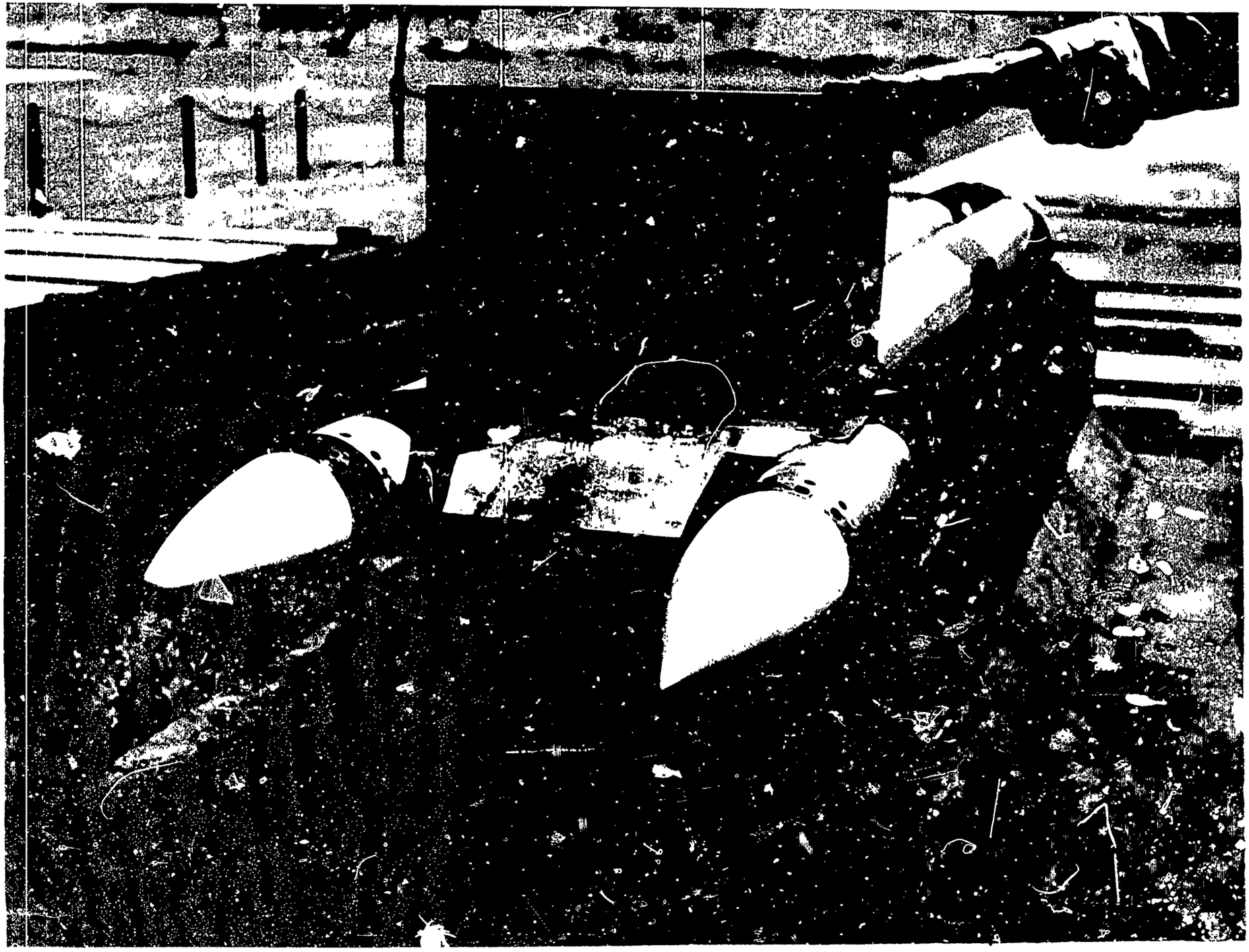

FIGURE 19 – Pointed, Tip Glazed Radome (Second Run) and Corning Fused Silica Radome Before Run #4

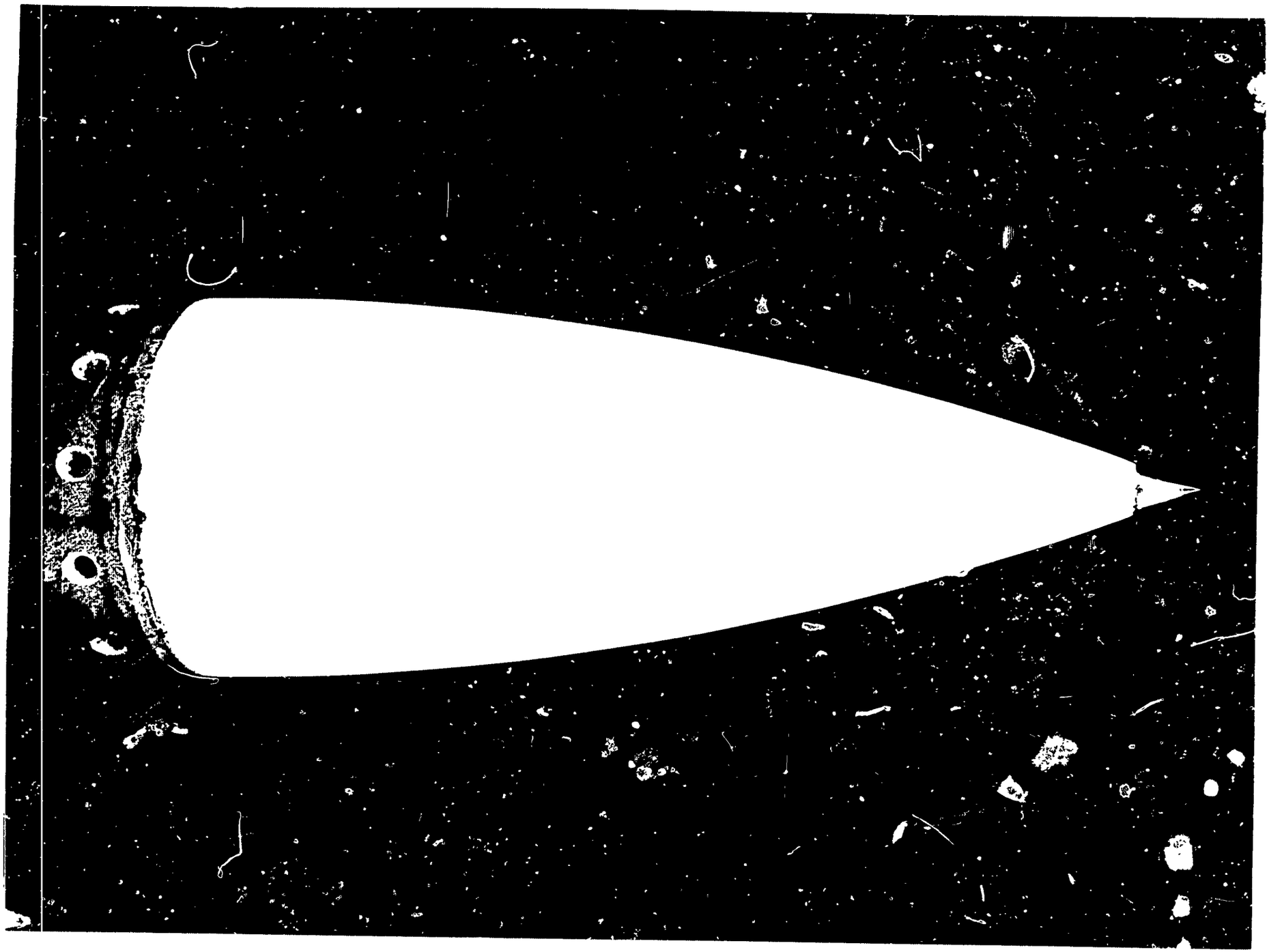

FIGURE 18 - Closeup of Steel Tipped Radome After Run #3

FIGURE 21 - Pointed, Tip Glazed Radome and Corning Attachment Ring After Run #4

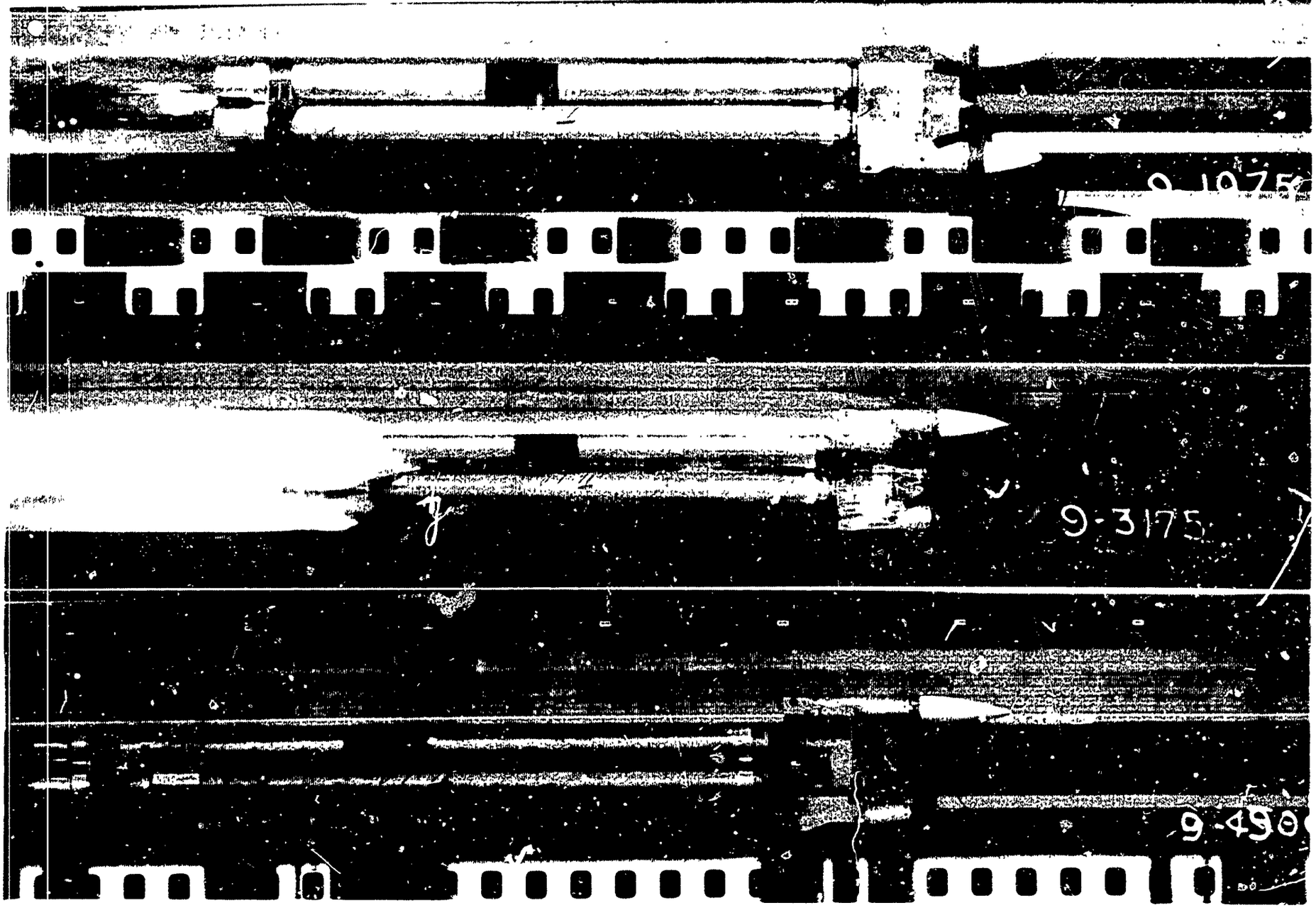

FIGURE 20 - Synchroballistic Camera Shots of Run #4

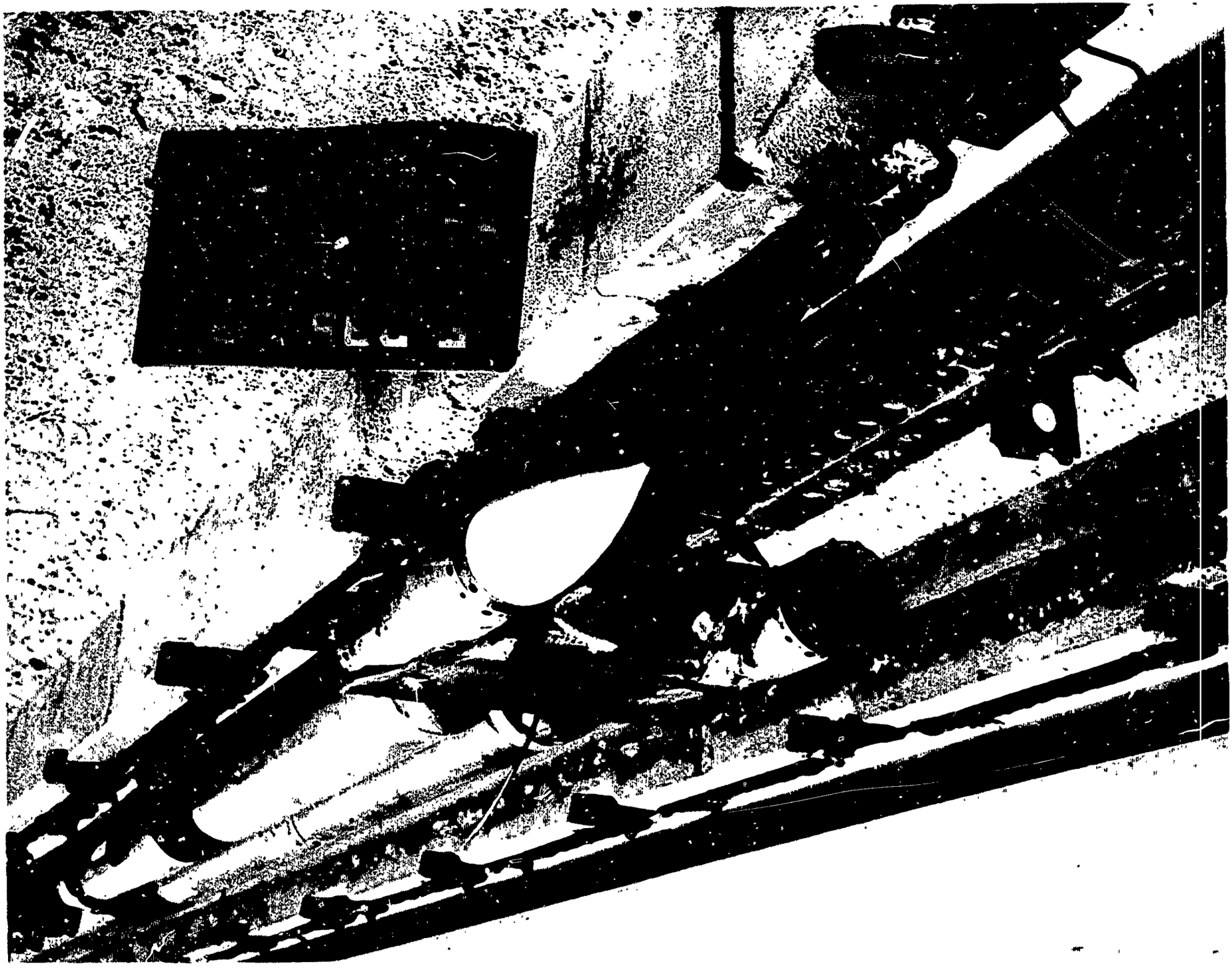

FIGURE 23 - Closeup of Corning Attachment Ring After Run #4

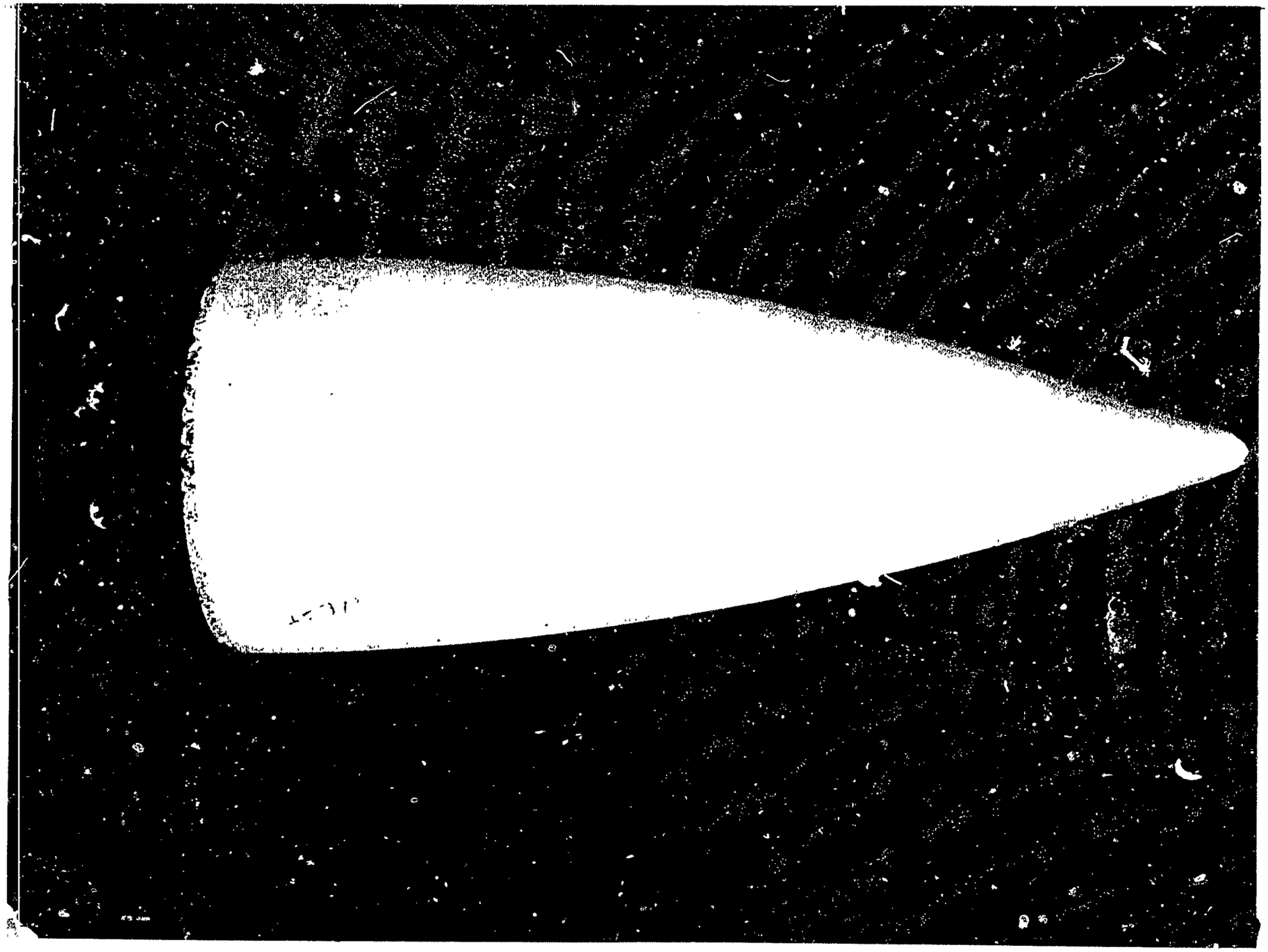

FIGURE 22 - Closeup of Pointed, Tip Glazed Radome After Two Runs (#3 and #4)

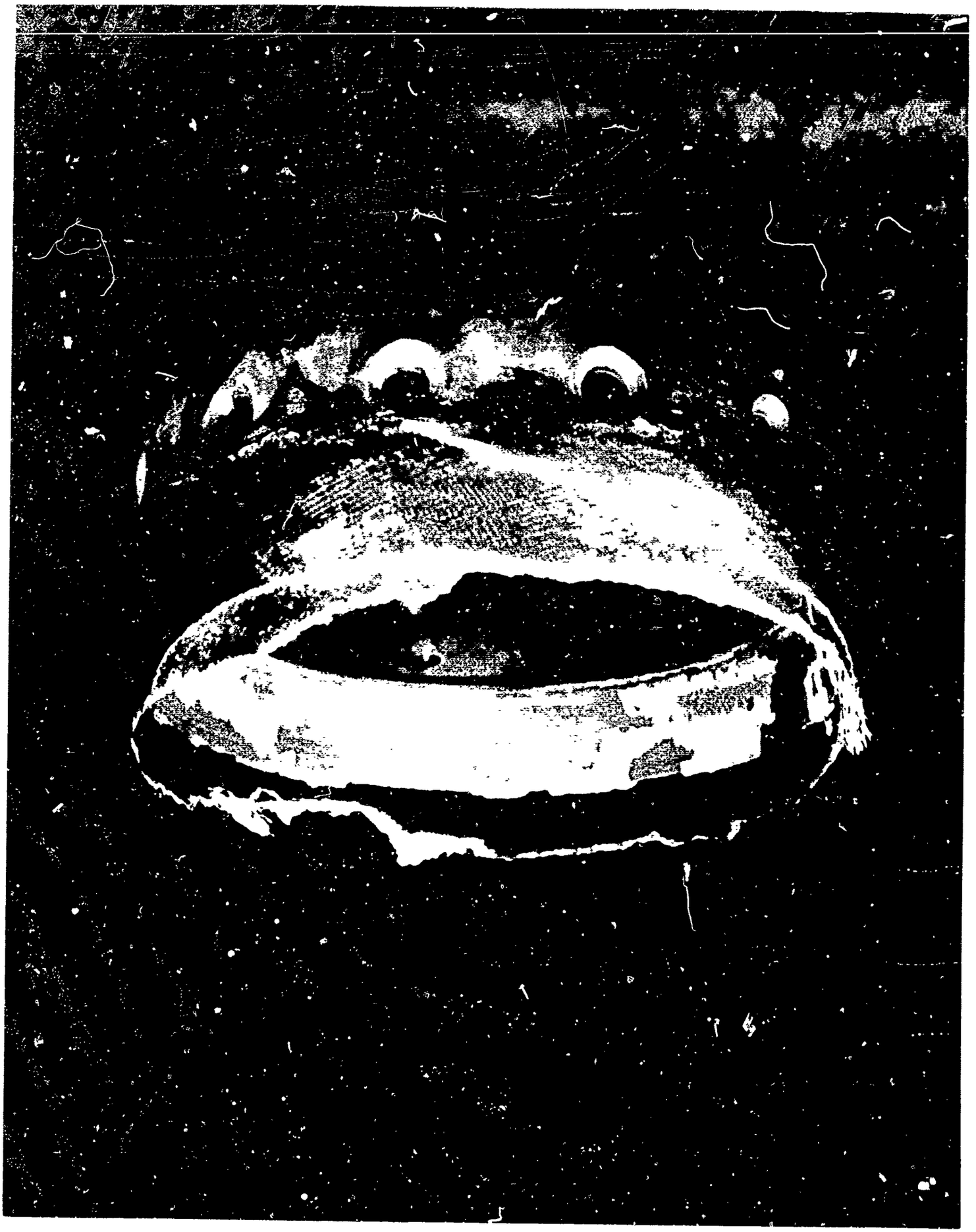

ADVANTAGES OF DUAL WALL RADOME CONSTRUCTION FOR TACTICAL RADAR SYSTEMS

WILLIAM M. FOSTER
SECTION HEAD
RADIATION DIVISION
SPERRY GYROSCOPE COMPANY

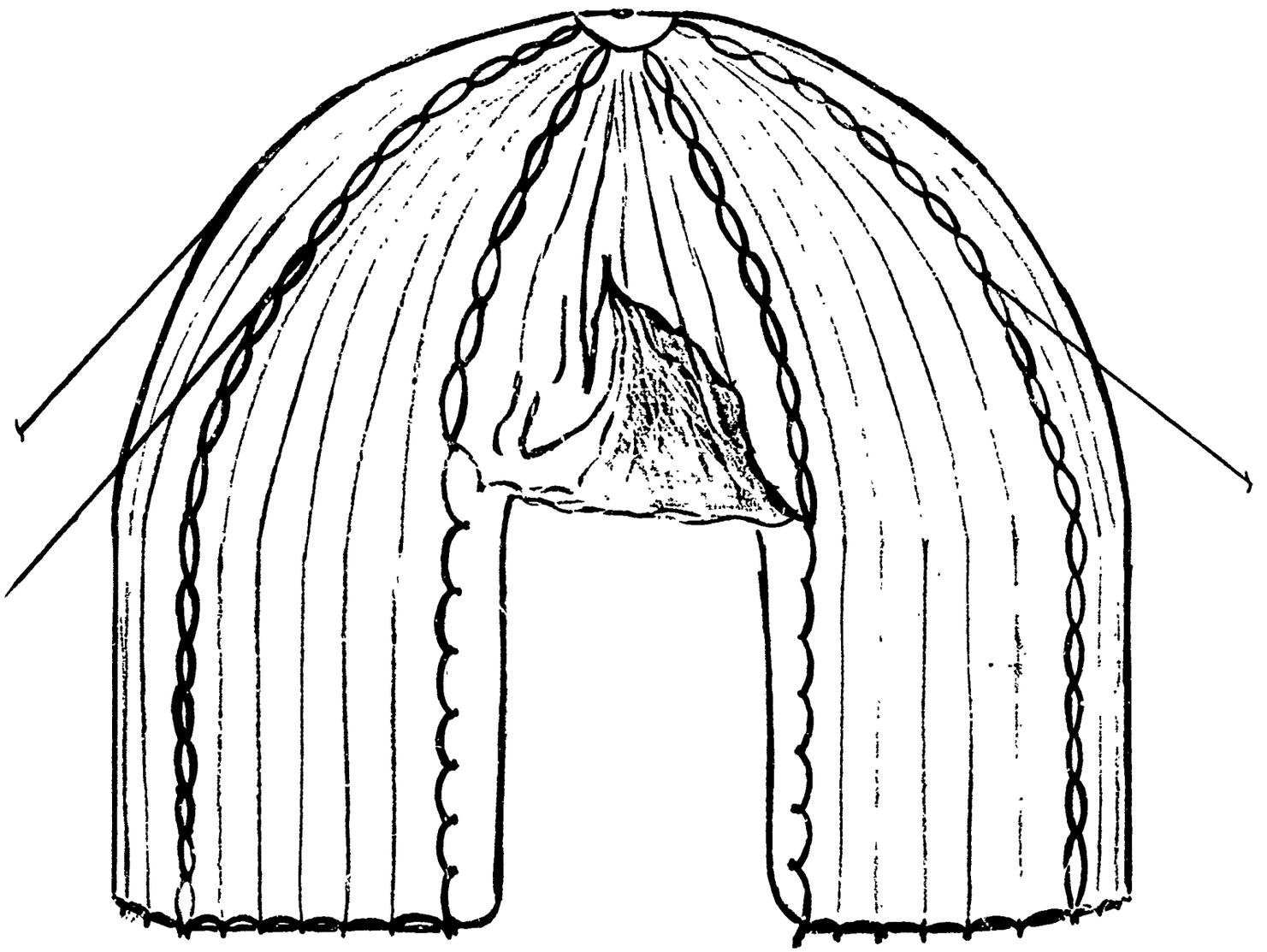

TPS-34 RADOME

INTRODUCTION

The dual wall air inflated structure has been developed to satisfy a need for a structure with capabilities that were not available in rigid structures or in the single wall air supported structures. The required capabilities were evolved from the needs of transportable, field equipment. The dual wall construction has been used both on shelters and radomes and provides the fast and easy erection, lightweight, minimum transport volume common to all air inflated or supported structures. The electrical characteristics of dual wall radomes are covered in the paper, "Transmission Characteristics of Ground Based Radomes)*. This paper will present the general structural aspects, with detail reference to the radome used with the TPS-34 Radar System.

General:

Description of the Dual Wall Air Inflated Structure

This type of radome consists of a rigidized wall structure where air is used to provide structural stiffness to the walls, rather than providing direct support as in single wall air supported structure design. It is this basic difference in construction that provides many of the desirable features of this design approach.

There have been a number of shelters and radomes built using this principle with the following common characteristics.

The air pressure is contained in a member with inner and outer walls which are prevented from billowing out by tie connections with a width set to achieve the required wall

* OSU Radome Symposium 1964 - J. D'Agostino - F. Rouffy

thickness. The structural member may be shaped to be flat or curved as required. The overall structure can be made as a composite of dual wall air inflated members and cloth or metal sections. The dual wall members can be considered as air beams rather than as sections of a membrane as with single wall construction. The following advantages are common to this type of construction:

1. The inside work area does not have to be pressurized as in single wall construction.

2. There is no need to provide a seal between the inside work areas and the radome exterior. This eliminates the need for keeping door areas small, the need for rapid opening and closing of doors, and the use of air locks.

There is no need to make the seams between sections air-tight. Therefore the section joints can be simple and can be designed for optimum structural efficiency.

3. Since the air is completely contained in a cell the air leakage rate is very low. Inflation blowers need only be run for a small percentage of the operating time, which increases their life and reliability of operation and decreases the electric power consumption. Small capacity blowers can be used. This factor is extremely important where the only source of electrical power supply is a large generator, which at times may be required only to provide power for the radome. Occasional operation of the generators reduces fuel consumption, and wear on the generators.

In the event of an electrical power failure or air supply failure the leakage rate determines how long the air inflated structure will maintain its structural capability. The low leakage rate of the dual wall construction may provide hours of standing time as compared to minutes for a single wall air supported structures.

4. The air beam construction permits a wide variety of shapes in order to best suit the system requirements. A single wall membrane structure must have a basic spherical shape with a possible partial cylindrical shape between spherical ends. On large structures with a height to diameter ratio greater than .75, the floor area is greatly reduced due to the curved in portions of the sphere. This limitation does not hold for the dual wall air beam, structure which may have cylindrical walls or if needed for added floor space, a connical shape.

5. The dual wall structure is composed of a number of separate air beams. Just as in a rigid structure, the design can provide for the removal of members, at least one at a time, without a serious loss in structural strength. This capability which is not present in single wall design, presents a number of attractive features, one of the most important is that failure of an individual member will not cause failure of the whole structure. Air inflated structures, particularly those used in field installations are subject to damage from accidents caused by operating personnel, flying debris, improper handling and poor maintenance, age or a

manufacturing defect. It is most probable that a failure caused by one of these conditions will occur when the winds are high. Loss of the radome may then result in complete loss of the system. These possible failures can be predicted and an added margin of safety incorporated in the design of the other beam members that will have to support the added load.

6. As part of the system installation it may be necessary to handle a large sized unit or during the course of operation a large sized unit may be added or replaced. In order to accommodate this situation, sections of the dual wall air beam structure may be deflated and removed or pulled back to achieve the required opening, and then resecured.

7. For system erection in inclement weather it is easier, faster, and safer to erect the equipment under shelter. In order to do this with a single wall shelter, the equipment must be piled up, the shelter cloth draped over, fastened and inflated. This procedure may be difficult and hazardous to the equipment and the radome. The alternative is a large airlock which is objectionable. In contrast the air beam structure can be erected without the system equipment inside, and may be erected, even before the equipment arrives at the site. A convenient opening may then be made by deflating certain sections to provide a sufficiently large opening for a truck, fork lift, crane car. On some installations it has been found that by providing a sufficiently deep opening, the equipment could be lifted by a crane off the truck, directly into position, without difficulty, risk or special erection equipment.

8. The repair of a beam section can be readily made in place if the damage is not extensive. This can be done because the damaged section can be deflated, removing the tension in the fabric, allowing proper curing of the bond.

If the section cannot be repaired in place, or not at all, the section can be removed and replaced without disassembly of the radome or the system equipment.

9. The dual wall area provides a high degree of thermal insulation. This is important in that high operating temperatures due to solar heating can be minimized, and that the interior can be easily and efficiently heated in cold climates.

The principles and advantages of dual wall construction were applied in the development of a radome for the TPS-34. Transportable Search and Height Finding Radar System, which was developed by Sperry for use by the Marine Corps.

The TPS-34 radome is a dual wall air inflated structure cylindrical in shape with a hemispherical shaped top. The inside diameter is 45 foot and the inside height to the crown is 41½ foot. The structure is divided radially into 8 similar sections for convenient handling of the individual sections. Each section is a separate beam structure in itself. The section shape is a section of a cylinder for a length of 19 feet which blends into a sector of a hemispherical cap. When inflated the section is approximately 18 feet wide. The inner and outer walls are connected by fabric ribs spaced every 1 ½ feet for a total of 12 per section. The ribs are vertical and aid in resisting the

bending moments in a manner similar to that of ribs in metal beam structures.

The ribs are 30 inches wide in order to provide a section adequate beam strength and stiffness.

The radome was designed to provide a weather tight enclosure and resist winds in excess of 90 mph. This capability was adequately tested by being in the path of hurricane winds with a speed of over 100 mph.

The unique properties of the dual wall structure were utilized for tactical advantages in the TPS-34 system, as follows:

1. The antenna size dictated the need for a minimum inside diameter of 45 feet and a minimum inside height of 41½ feet. With a single wall spherical radome the base diameter would be 24 feet. This would be inadequate for structural stability, installation, and maintenance of the system equipment. Enlarging the radome diameter sufficiently to obtain sufficient space would have been uneconomical and added other problems. With the air beam construction, there is no limitation on the shape of the radome from the top hemisphere to the ground. A cylindrical shape was chosen as providing adequate groupd space. If it were needed, a connical base could have been used.

With one section deflated and opened, a 18 foot opening is created which has been used to drive in with a truck and a crane car. The air beam construction provides sufficient structural rigidity with one section missing, to withstand winds over 60 mph.

Since the sections do not have to be sealed relative to each other, a simple fastener, spaced every 18 inches is used to join the sections together. This fastener can easily and quickly be connected and is relatively foolproof. The fasteners are part of a catenary rope assembly which is fastened to each side of the radome. The fastener connections serve as steps for climbing the radome. Unlike spherical radomes which have back slopes the TPS-34 has vertical walls, which are easy and safe to climb.

The inflation equipment is designed for rapid inflation during erection. Two blowers are used for increased reliability and more flexible operation. For the inflation during installation, both blowers are used in parallel in order to obtain a maximum flow rate to minimize the elapsed time. Approximately 20 minutes are required between the time the blowers are started and the radome is fully erected. After the radome is erected the leakage rate is so low that the blower need only be operated for less than five (5) minutes in every four (4) hour period. This extends the life of the blower equipment almost indefinitely. The original blower assembly has been in use six (6) years without any replacement. In order to stiffen the radome to resist the higher wind speed dynamic loads, the inflation pressure is increased by coupling the blowers in series by operating a connecting valve.

Since the lift forces are not excessive and a seal to the ground does not have to be attained, the ground anchorage is simple. The radome is anchored direct to the ground without recourse to rings or other supplemental structures. A steel

caternary cable is connected to the base of the radome by imbedding it in a fabric assembly which in turn is bonded to the radome section. Arrow head type ground anchors, spaced every 3 feet around the circumference of the radome base and connected to the caternary cable through hooks which are clamped to the ground anchor.

The radome has proved to be an excellent insulator. During cold weather test periods a 50,000 BTU/Hr heater was adequate for comfortable efficient work environment.

For hot weather operation with all equipment operating a vent was provided in the top. This vent with the assist of a small blower kept the temperatures down to an acceptable level.

The system is designed for installation without power equipment. All units are hoisted and positioned using simple block and tackle. The air beam construction allows connection of the block and tackle not only to the top center, but to any point along any section joint. The tackle is connected into the section fasteners. For most lifts a single block and tackle is adequate but for heavy lifts two and three are used together to share the load. Over 2000# lifts have been made with this arrangement.

The prototype of this radome was developed and built by Bird Air Structures of Buffalo, N.Y. This radome was used to develope erection techniques, evaluate the system, and function as a radome enclosure for a continuous period of over six (6) years. It is still in use with no indication of a limitation in its useful life. During the six (6) years of its operation, this radome has been used in a number of different sites in the continental U.S. with a wide

variety of environment conditions including two hurricanes.

In general dual wall construction is heavier and more expensive than single wall, due to the double walls and the interconnecting ribs, even though the individual walls are lighter than for a single wall. The added thickness of material may affect the electrical performance to a greater extent than single wall construction, when the structure is used as a radome.

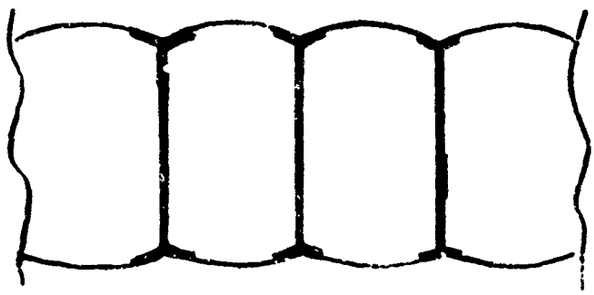

TYPICAL DUAL WALL CONSTRUCTION

Microwave Fields Near a Hollow Dielectric Wedge and Dielectric Slab

G. Tricoles and E. Rope

General Dynamics-Electronics, San Diego

I. INTRODUCTION

For some time there has been interest in predicting radome boresight errors, and, because practical antenna and radome configurations are not such that boundary conditions can be fitted, approximate methods have been devised. These methods can be put into two classes, scattering methods and ray tracing methods. It might be expected that the scattering methods would be more accurate because they appear to be more rigorously formulated; however, computational approximations made in the scattering procedures may limit their utility to idealized configurations.[1] On the other hand, a ray tracing method has lead to reasonable results for a radome enclosing an antenna of diameter sixteen wavelengths.[2] In this method the radome was approximated as locally plane. It is possible of course to make various approximations which would then give rise to other forms of ray tracing methods. Describing the radome as locally plane would seem to be more valid for larger radomes than for smaller radomes. In fact results for a radome of base diameter six wavelengths support this reasonable expectation.[3] Therefore it seems that consideration should be given to modifying ray tracing approaches to include more realistic descriptions of scattering mechanisms not contained in straightforward ray tracing.[4]

In this paper a description is given of measurements made on the fields propagated through a hollow dielectric wedge. These measurements were made to test the existence of a vertex scattered wave and of waves guided by the dielectric wall. Such waves are the sort of modification to ray tracing mentioned earlier.

II. APPARATUS AND PROCEDURE

A microwave interferometer was used for the measurements. A klystron generated microwaves at 9.409 Gc. The usual arrangement was used and is shown in Figure 1. Precision of measurements is ±0.1 db for power and ±1° in phase. Spacing was such that the $2D^2/\lambda$ criterion was well exceeded.

Measurements were made with the probe moved parallel to the walls of the dielectric wedge. Probing paths are shown as dotted lines in Figure 1. A set of parallel paths was used, each path being a fixed distance from the wall. Several different probes were used so as to find what effects might be caused by the probe. An open end waveguide, a balanced monopole, and a dipole with a reflector were used.

The dielectric wedge was made from two plexiglas sheets 18" square, and .250" ±010" thick. An edge of each sheet was beveled so as to form a sharp point at the vertex. The two sheets were glued together. Included angle was 60°. The wedge was placed with its axis of symmetry along the direction of propagation of the incident wave, which was polarized with the E vector along the vertex.

III. RESULTS OF MEASUREMENT

For a dipole probe spaced 0.125" from the walls of the wedge, measured results are shown in Figure 2. Data are shown for the probe behind the wedge and for the wedge absent. The probe was moved parallel to one wall and then parallel to the other. The y coordinate is that shown in Figure 1.

Measurements were repeated with the same probe at the same spacing after removing one of the walls of the wedge. A smooth surface resulted on separating the edges which had been glued together.

The single slab, which was one of the walls of the wedge, was turned about so that a square edge was placed at the original vertex region. Measurements were made using a monopole probe and are shown in Figure 4. The probe was set at various distances from the wall. The x coordinate is that shown in Figure 1.

IV. DISCUSSION

The deep minima observed behind the wedge and behind the single slab seem to be interference minima. These are interpreted as arising from interference of two waves. The first of these is transmitted through the sheet and travels in the direction of the incident wave. This wave can be described by refracted rays which emerge through the sheet. The second wave is guided along the dielectric surface. This wave would be a correction to ray tracing.

Note that the extrema are more pronounced behind the single slab than behind the complete wedge. However, spacing of minima is nearly the same in both cases. The notion of a guided wave is supported further by the rapid decrease of depth of minima with increasing distance from the sheet, as in Figure 4.

As a test of the preceding interpretation, a prediction can be made of spacing of the minima. Let the directly transmitted wave be described by a plane wave transmission coefficient T. For the wave guided by a dielectric wall let k_g be the propagation constant. For an infinitely long slab a propagation constant for a guided wave can be calculated from well known theory by solving some transcendental equations arising from matching boundary conditions. We use this value for the present slab of finite width.[5] For an incident wave of amplitude one, the field behind the wedge is then taken to be

$$E = Te^{ik_0 x} + Ae^{ik_g x/\alpha},$$

where x is cos ϕ_c, ϕ_c being half of the angle included by the wedge. A is the amplitude of the guided wave. An estimate can be made of A by comparing both the depths of minima and heights of maxima to the incident field. One obtains A = 0.4 or 0.5 for these cases. Spacing of minima follows from the condition that $(k_0 - k_g/\alpha)\,x$ is equal to a multiple of π. For a wall thickness of 0.250" and for plexiglass, measured and computed spacings of minima are shown in Figure 5. Spacings are given in terms of the wavelength at 9400Mc, λ_0. This value is 1.255". A dielectric constant of 2.6 was assumed.

The moderately good agreement of measured and computed spacings seems to support the preceding hypothesis.

Additional measurements have been made with hollow cones. These show results similar to the preceding.

V. SUMMARY

A description was given of the effects of finite dielectric slabs on propagation of nearly plane microwaves. Measurements showed a very deep minima behind the slab. Without the slab, the field was nearly uniform. It was assumed that the minima were produced by interference of a plane wave transmitted through the sheet and a guided wave propagated along the slab. Quantitative predictions were made of spacings of minima by using the propagation constants appropriate for a slab of infinite extent. Even with this idealization, measured and computed spacings agreed within a few percent.

For a hollow wedge formed by two slabs, similar minima were found; however, effects were less than for a single slab.

Very similar experimental and theoretical results have been found in more recent work on hollow dielectric cones.

VI. ACKNOWLEDGMENTS

For helpful discussions it is a pleasure to thank Professor J. H. Richmond of the Ohio State University, A. I. Mahan of the Applied Physics Laboratory at Johns Hopkins University, and Professor H. Booker of Cornell University. In addition Mrs. V. Woelber and Mrs. F. Hayes typed the manuscript and J. Austin made the drawings.

REFERENCES

1. G. Tricoles and D. Turley, "Radome Error Prediction", Aeronautical Systems Division Technical Report Number ASD TR 61-612, January 1962.

2. G. Tricoles, "Radiation Patterns and Boresight Error of a Microwave Antenna Enclosed in an Axially Symmetric dielectric Shell" to appear in Jour. Opt. Soc. Am.

3. G. Tricoles and D. Gelman, "Application of a Ray Tracing Method to Predicting Errors of a Small Radome", OSU-RTD Electromagnetic Window Symposium Proceedings, 1964.

4. G. Tricoles, "Radiation Patterns of a Microwave Antenna Enclosed in a Hollow Dielectric Shell", Jour. Opt. Soc. Am. 55, 535, (1963).

5. R. F. Harrington, Time Harmonic Electromagnetic Fields, McGraw-Hill Book Company, P165.

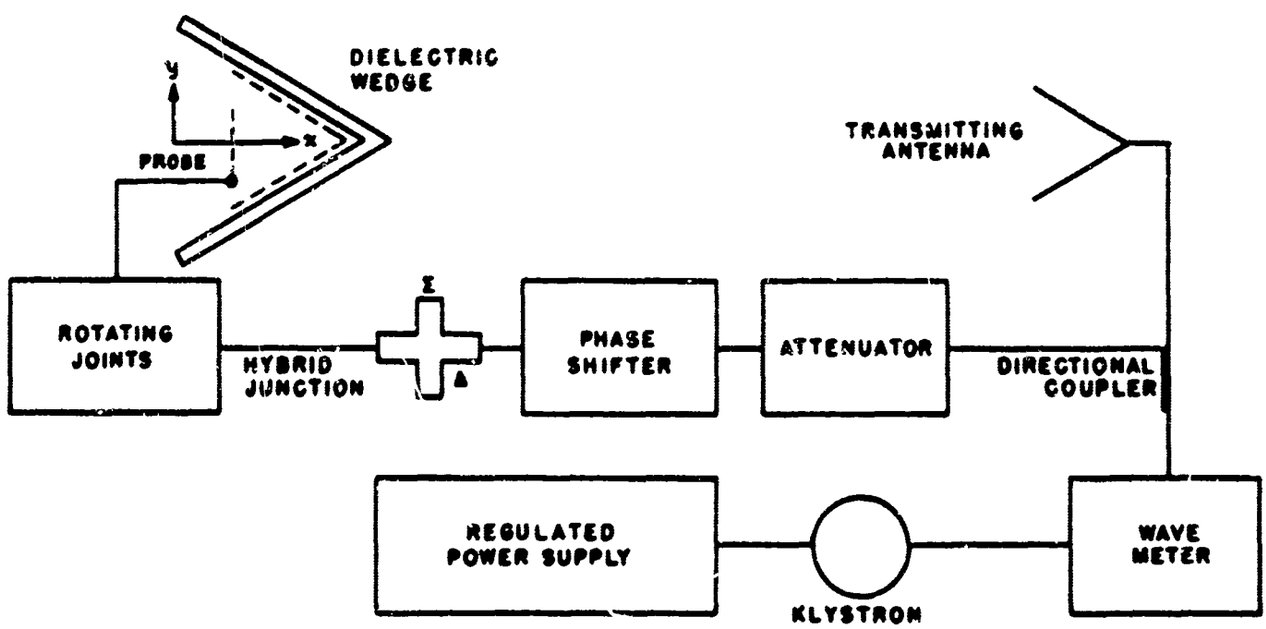

Figure 1. Microwave Interferometer. Probing Paths are Shown as Dotted Lines

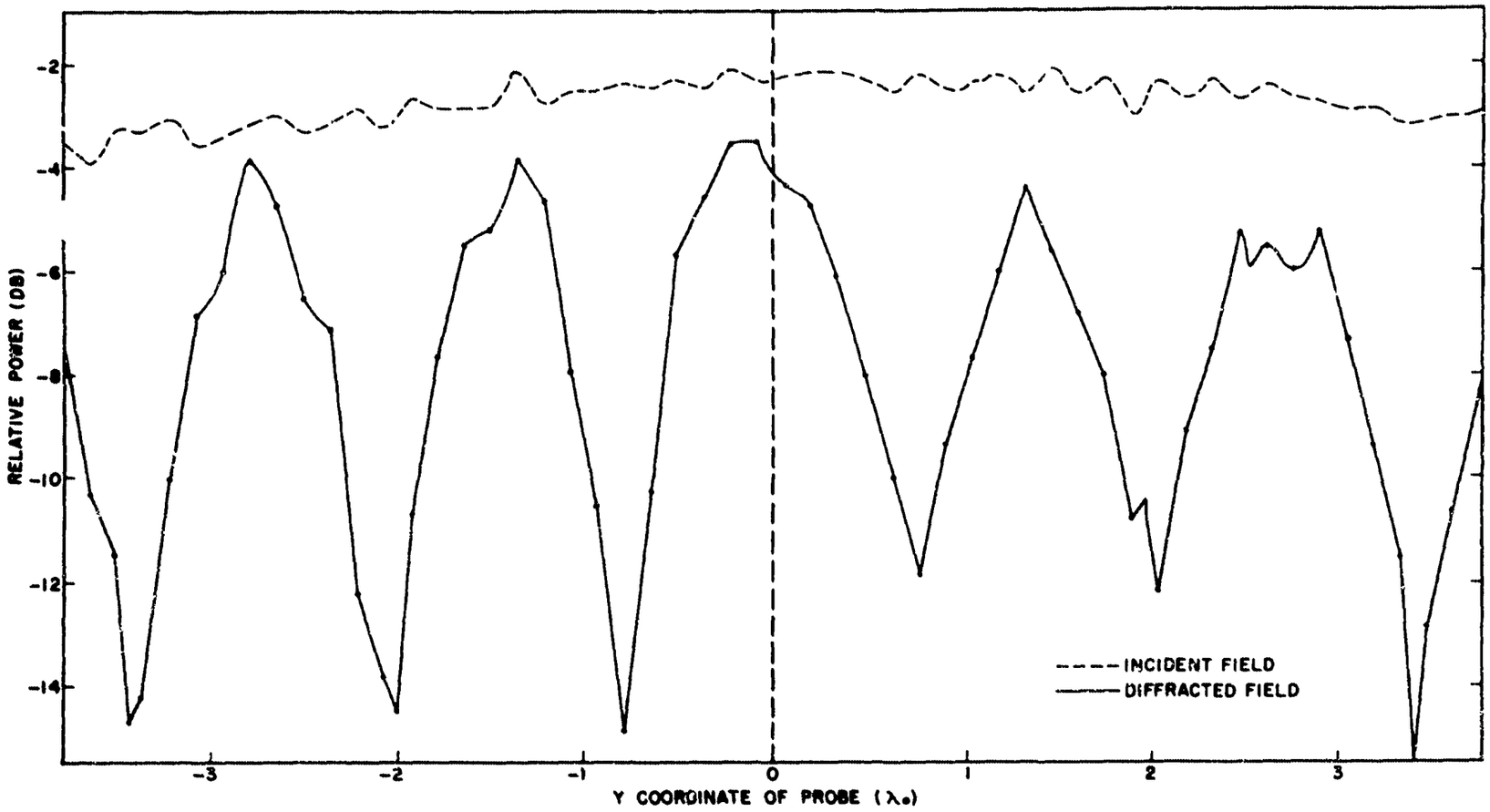

Figure 2. Relative Power Measured Behind a Hollow Plexiglass Wedge with a Dipole Probe Spaced 0.125" from the Walls. The Y Coordinate is Defined in Figure 1

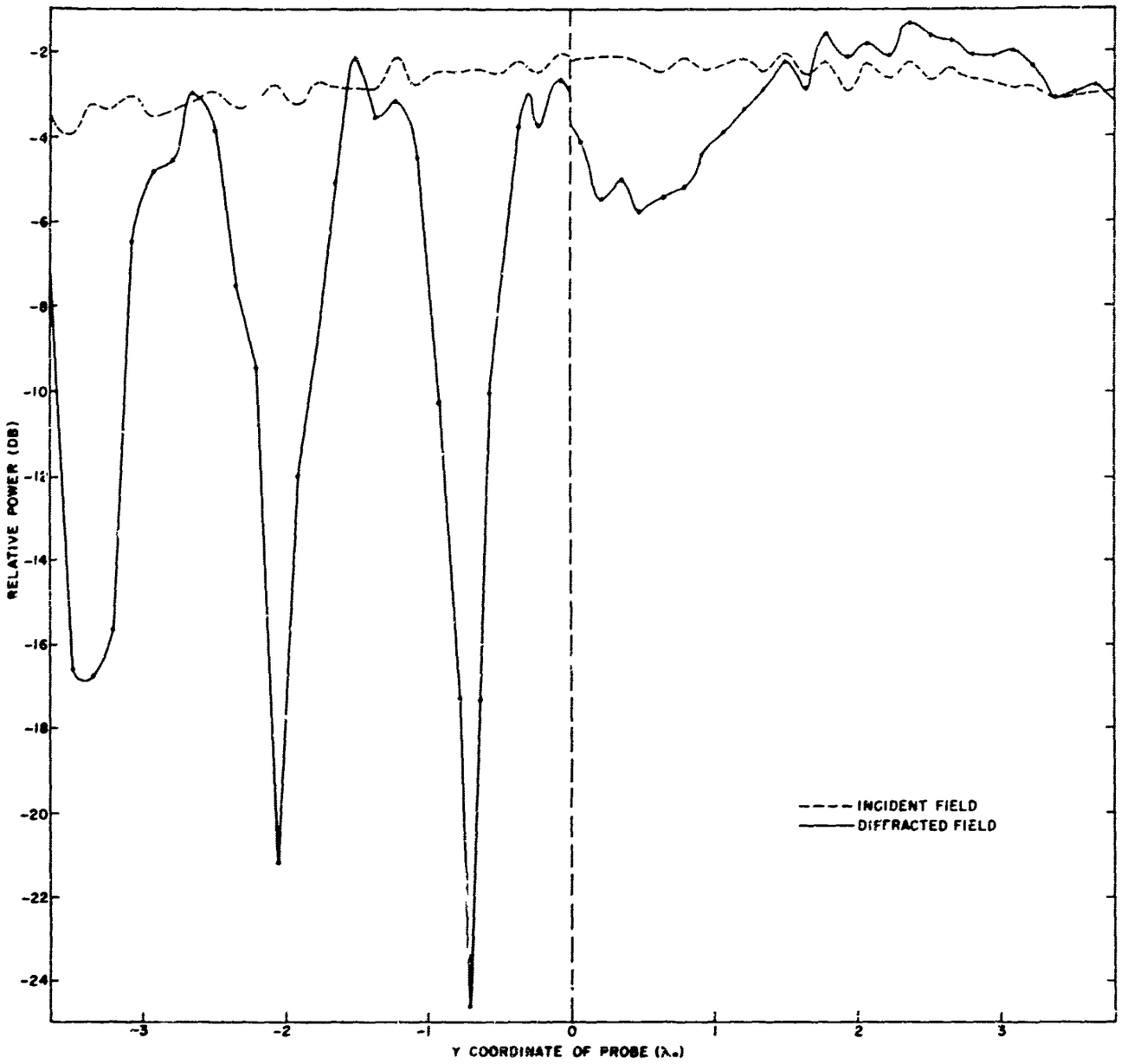

Figure 3. Relative Power Measured Behind a Single Slab of the Wedge with a Dipole Spaced 0.125" from the Walls. The Y Coordinate is Defined in Figure 1

Figure 4. Relative Power Measured Behind a Dielectric Slab with a Monopole Probe for Various Spacings of the Probing Paths

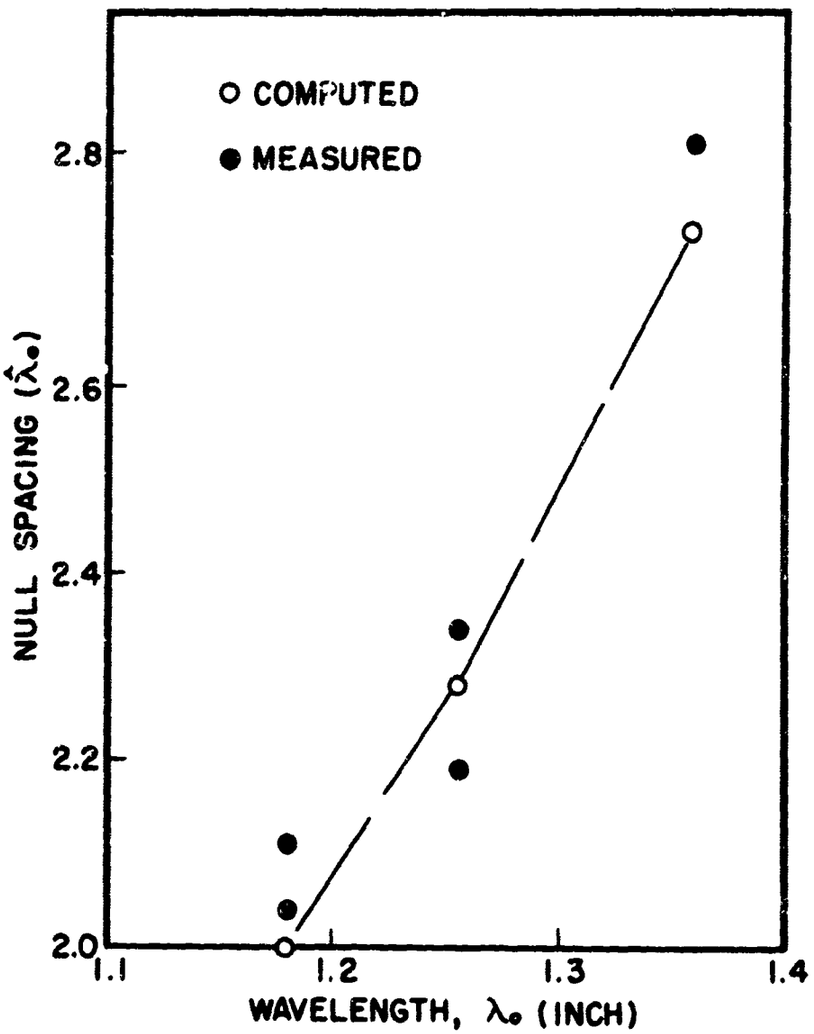

Figure 5. Measured and Computed Spacings of Minima

APPLICATION OF A RAY TRACING METHOD FOR PREDICTING RADOME ERRORS TO A SMALL RADOME

G. Tricoles and D. Gelman

General Dynamics-Electronics, San Diego and
General Dynamics, Pomona

1. INTRODUCTION

A description is given of application of a radome error prediction method to calculating the performance of a missile radome of diameter 6 wavelengths and length 12 wavelengths. These results are compared with measurements.

The theoretical basis for this work is approximate, being based on ray tracing and on aperture fields. This same method has been applied to design and correction of radomes for an interceptor [1], and in a less practical case, to a hollow dielectric wedge [2].

Theory is given in References 1 and 2; however, a short review of the theory will be given in the second section of this paper. In the third section, ray tracing is described. Radome error calculations based on approximating the radome as locally plane, will be described in section 4. Measurements are described in section 5. Additional calculations are described in section 6 assuming the radome vertex scatters energy.

An approximate description is used because the antenna dimensions were of the same order of magnitude as the wavelength. This theory is based on Schelkunoff's induction and equivalence theorems [1]. The basic calculation is of the complex valued

electric field received by an antenna in a hollow shell for a fixed incident direction of a plane wave. A ray tracing procedure is used to describe propagation of the incident wave through the shell. A ray is traced through the shell to some typical point near the aperture, using Snell's law, the multiple reflections in the curved shell are approximated by those in an infinite flat sheet. A transmission coefficient is evaluated, at the typical point, for an incident plane wave and a flat sheet. Parameters of this sheet are chosen so that the optical path of the rays in the flat sheet are the same as, or a multiple of, the optical path of the ray traced through the curved shell. This latter ray being that transmitted directly, i.e. not multiply reflected. This approximation was made so as to consider a wave incident at a general angle. Calculations have been made only for the normal to the incident wave being in the horizontal or vertical plane through the axis of symmetry of the shell. Moreover the aperture plane is rotated about an axis which can be in either of the two planes.

The electric vector of the incident field can be elliptically polarized in the theory but calculations are presented only for linear polarization. The dielectric shell produces ellipticity of polarization of the field propagated through it. An approximate description of this ellipticity is included. It is assumed that the antenna senses only the field lying along a single direction which is parallel to the aperture plane but otherwise arbitrary. Thus while depolarization is described, only the field components in a given direction are detected. This is in fact an approximation.

2. THEORY

Calculations are made in two steps. First for a linearly polarized plane wave, incident on the outside of the radome, the field propagated through the radome is found approximately. Then this field is coupled into the antenna. This second step can be made using an experimental approximation to the field produced, in the antenna transmission line, by a secondary radiator, a Huygens source, is called an aperture response function. Such a procedure has been used earlier.[1,2] In the present work a theoretically determined response function was used. This function was that used in designing the radar antenna and yields accurate diffraction patterns in Kirchoff integral calculations.

The radome antenna considered was a slot array consisting of four quadrants with 10 slots per quadrant. It is significant for understanding the calculations later that the quantities observed are the differences in the RF phase of the fields produced in opposite quadrants of the antenna. The difference between these phase values can lead to a guidance error in the presence of the radome. It is assumed this error is negligible in the absence of the radome.

For angular displacement of the antenna in the horizontal or the vertical planes, phase error is symmetric between two pairs of quadrants. These planes coincide with extremes of linear polarization relative to the plane of antenna displacement.

For receiving operation of the antenna assume an incident field in the form of a linearly polarized plane wave. Within the region bounded by the radome, the field is described through the complex valued transmission coefficients T_e described later. Field computations are made for certain points on a plane near the antenna and perpendicular to its axis, which in general does not coincide with the axis of the shell. This field is then considered a planar array of equivalent sources. Relative, complex valued field at a detector connected to the antenna is computed by integrating antenna response to each equivalent source over the plane. Antenna response to each equivalent source is obtained by first finding response to a known source as a function of position. This function is the aperture response function mentioned earlier. Antenna response to any equivalent source in the wave is then the product of the aperture function and the strength of the source at corresponding points; similarly, antenna response to the entire incident wave is then the integral of the product over the significant part of the wave front.

A basic computation is of the complex field corresponding to a fixed direction of the incident plane wave. For another wave propagation direction, the procedure is repeated. A new field is calculated and an integration is done over these new sources, using by assumption, the same response function as before.

Consider a plane wave incident on a radome housing an antenna, as in Figure 1.* In the region bounded by the radome, the field is computed at a point on a portion of a

plane near the antenna and perpendicular to the antenna axis. At a typical point, P_s, the field produced by the incident wave will be approximated as that which would result if the radome were replaced by an infinitely broad flat sheet chosen in the manner described below. Reradiation by the antenna will be ignored; in effect, scattering by an isolated dielectric object is being considered.

From P_o, in Figure 1, a ray is traced in the direction of $\underset{\sim}{1}_R$, a unit vector along the ray to P_i, and then to P_s.

The incident electric field at a point P is

$$\underset{\sim}{E}^I(P) = E_o^I e^{-i\omega t} \cdot e^{i\underset{\sim}{k} \cdot \underset{\sim}{r}(P)} \underset{\sim}{\hat{e}} \qquad (1)$$

Where

E_o^I is the scalar amplitude of the linearly polarized plane wave,

ω is the angular frequency,

i is $\sqrt{-1}$,

k is the propagation constant,

$\underset{\sim}{\hat{k}}$ is a unit vector in the direction of propagation,

$\underset{\sim}{r}(P)$ is the position vector to P,

$\underset{\sim}{\hat{e}}$ is a unit vector in the direction of the electric field.

* All figures are collected at the end of this report.

At P_o the field is resolved into components parallel and perpendicular to the plane of incidence which contains the ray and normal to the surface at P_o. Let $\underset{\sim}{1}_\perp$ and $\underset{\sim}{1}_\parallel$ be unit vectors perpendicular and parallel respectively to the plane of incidence. Let $\hat{\underset{\sim}{e}} \cdot \underset{\sim}{1}_\perp$ be α and $\hat{\underset{\sim}{e}} \cdot \underset{\sim}{1}_\parallel$ be β. Therefore, at P_o the incident field is

$$\underset{\sim}{E}^I(P_o) = E^I(P_o)\ \alpha\ \underset{\sim}{1}_\perp + E^I(P_o)\ \beta\ \underset{\sim}{1}_\parallel \ .$$

It is now assumed that the field at P_s can be described by replacing the curved radome by a flat sheet. This assumption is probably the most approximate in the procedure. Selection of the approximating flat sheet is made as follows. A ray is traced from a point on the antenna in a direction parallel to the incident wave. Note that the ray tracing is done from inside out now. This is done for convenience in numerical calculation and is an approximation. A ray is traced from P_i to P_o using the normal to the surface and Snell's law, assuming small absorption. The distance P_i to P_o is then calculated by solving simultaneously the equations of the refracted ray and outer radome surface.[3] Now the approximating plane sheet is chosen to have the same ray path as the distance $\overline{P_i P_o}$. Its thickness is $\overline{P_i P_o} \cos r$ where r is the angle of refraction calculated using the dielectric constant of the shell and normal to the surface at P_i.

It must be emphasized that this approximation is physical and clearly is not rigorous, for the multiple reflections in the flat sheet and in the curved shell will not be identical. For shells of sufficiently large radii of curvature this may be an acceptable approximation.

With this approximation, the field at P_i is then

$$E^R(P_i) = \left[\alpha\, E^I(P_o)\, |T_\perp|\, e^{i\Delta_\perp}\right] \underset{\sim}{1}_\perp + \left[\beta\, E^I(P_o)\, |T_\parallel|\, e^{i\Delta_\parallel}\right] \underset{\sim}{1}_\parallel . \qquad (2)$$

$T_\perp$ is a complex valued transmission coefficient for plane waves incident on infinitely broad plane sheets for perpendicular polarization.

In fact for a single layer

$$T_\perp = |T_\perp|\, e^{i\Delta_\perp}$$

where

$$|T_\perp| = t_{01}\, t_{10} \left[1 - r_{10}^2\, e^{i(2k_o Sd)}\right]^{-1} e^{ik_o Sd}$$

and

$$\Delta_\perp = k_o (S - \cos\theta_i)\, d .$$

Here k_o is the free space propagation constant, d is the thickness of the dielectric sheet, θ_i is the angle of incidence, κ is the relative dielectric constant. Further, t_{01}, r_{10} and t_{10} are Fresnel coefficients. Finally,

$$S^2 = \kappa - \sin^2\theta_i$$

$T_\parallel$ is defined similarly for parallel polarization.

Next, an assumption is introduced concerning polarization properties of the receiving antenna. Cross polarization effects depend on the symmetry of the antenna and on the symmetry of the polarization of the field propagation through the shell. Assume the receiving antenna responds only to a single, linear electric field component and let this

direction be parallel to that of a vector $\underset{\sim}{1}_D$. Then the electric field component of the incident wave transmitted through the radome and in the direction of $\underset{\sim}{1}_D$ is

$$E_D^R(P_i) = |T_e| \; E^I(P_o) \; e^{i(\arg T_e)} \; \underset{\sim}{1}_D \tag{3}$$

with

$$|T_e|^2 = (|T_\perp| \alpha \delta)^2 + (|T_\parallel| \beta \delta')^2 + 2|T_\perp| \, |T_\parallel| \alpha \beta \delta \delta' \cos \gamma \; , \tag{4}$$

where

$$\delta \text{ is } \underset{\sim}{1}_\perp \cdot \underset{\sim}{1}_D \; , \; \delta' \text{ is } \underset{\sim}{1}_\parallel \cdot \underset{\sim}{1}_D \; ,$$

and

$$\gamma = \arg T_\perp - \arg T_\parallel \; .$$

Furthermore,

$$\arg T_e = \underset{\sim}{\Delta}_\parallel + \tan^{-1} \left[|T_\perp| \, |\alpha \delta| \sin \gamma \left\{ |T_e|^2 - (|T_\perp| \, \alpha \delta \sin \gamma)^2 \right\}^{-1/2} \right] \tag{5}$$

At P_s the field propagated through the shell and parallel to $\underset{\sim}{1}_D$ is, using Figure 2,

$$\underset{\sim}{E}_D^R(P_s) = T_e \; E^I(P_s) \; (\underset{\sim}{e} \cdot \underset{\sim}{1}_D) \; \underset{\sim}{1}_D \tag{6}$$

The ray tracing procedure described above is approximate also because the ray was traced from inside out. The angle of incidence is evaluated at P_i. It would seem that this should be done at P_o, but at P_o the tangent plane is not parallel to the tangent plane at P_i. For small radii of curvature this procedure seems inaccurate. It seems more serious than this approximation that an exact ray tracing procedure is not used. The actual, finite sum of multiple reflections which would occur in the shell is approximated by an infinite series which would arise for the flat sheet. However, the series

is a geometric series in the square of the Fresnel reflection coefficients; rapid convergence is expected because the Fresnel coefficients are mostly less than about 3/4. While the replacement with flat sheets is questionable in principle, experimental results obtained earlier are acceptable for certain radome applications.

It should be noted that the present formalism permits variation of the direction of polarization of the receiving antenna independently of the incident linear polarization. Hence depolarization can be described.

Thus an approximation has been made to the field before the receiving aperture. It remains to describe coupling of this field into the antenna and transmission line. The procedure for doing this is again approximate. It has been described previously, but will be summarized briefly for convenience.[2]

A wavefront can be considered as an array of secondary sources. By Schelkunoff's induction theorem, each secondary source is a combination of electric and magnetic current elements the moments of which are proportional respectively to the magnetic and electric intensities tangential to the wavefront. For a wave in a homogeneous medium, the induction theorem becomes the equivalence theorem, and the densities of magnetic current M and electric current J are

$$\underset{\sim}{M} = \underset{\sim}{E}^{I} \times \underset{\sim}{n}$$

and

$$\underset{\sim}{J} = \underset{\sim}{n} \times \underset{\sim}{H}^{I}$$

where $\underset{\sim}{E}^{I}$ and $\underset{\sim}{H}^{I}$ are respectively the electric and magnetic intensities of the incident plane wave, and n is a unit vector normal to the wavefront. For a linearly polarized

wave with rectangular components E_x and H_y, each element of area dA on the wavefront is an elementary source, a Huygen's source.

For a wavefront propagated through the radome, in the volume bounded by the radome, each element of area is considered as an elementary source and, thus, is equivalent to an electric current J and a magnetic current J_m, where

$$\underset{\sim}{J} \propto \underset{\sim}{H}$$

and

$$J_m \propto \underset{\sim}{E}$$

Here E and H are respectively the electric and magnetic intensities tangential to the wavefront. Let the field components in the transmission line of the receiving antenna at P′, due to an element of unit strength at a point P, be

$$dE_G = F(P, P') \underset{\sim}{E}^R dA \tag{7}$$

where $\underset{\sim}{E}^R$ is given by Eq. (3). The point P here is a general point, not necessarily $P(x_s, y_s)$. The field component sensed by the antenna due to the entire incident wave is

$$E_G = \iint_{\text{aperture}} F(P, P') E_D^R(P) \, dA$$

Power patterns are obtained from $|E_G|^2$. The integral is over a region such that $F \neq 0$.

It is assumed that a reasonably accurate approximation to F can be obtained from the design distribution. Call this approximation F_m. In practice, a sum is made

$$E_G = \sum_j \sum_k F_m(P, P') E^R(P) \tag{8}$$

3. RAY TRACING

Evaluation of the transmission coefficients described in the preceding section requires evaluation of path lengths of the rays. These path lengths are found by solving equations of straight lines, the rays, and the equation of a surface of revolution, the radome wall.

First, the outside surface of the radome is a surface of revolution, in a rectangular coordinate system with coordinates (t, y, z),

$$y^2 + z^2 = \rho^2(t) .$$

The function ρ (t) defines the von Karman ogive which specifies the radome shape. Specifically

$$\rho = a\,(\varphi - \frac{1}{2}\sin 2\varphi)^{1/2}/\sqrt{\pi}, \tag{9}$$

where

$$\varphi = \cos^{-1}\left(\frac{2t}{L} - 1\right) ,$$

here a is the radius at the base and L is the outer length of the dome. Now a ray is traced from a point, at which a slot would be located, on the antenna through the shell. Thus an equation is necessary for the inside surface of the radome. Let d be the wall thickness. Then the inward pointing unit normal to the shell is in the t, ρ plane

$$\hat{n}_{in} = \hat{i}_t \rho' (1 + \rho'^2)^{-1/2} - \hat{i}_\rho (1 + \rho'^2)^{-1/2} .$$

Here ρ' is $d\rho/dt$.

Thus the inner surface is given as

$$y^2 + z^2 = r^2(x) \tag{10}$$

where

$$x = t + \rho' d\,(1 + \rho'^2)^{-1/2} \tag{11}$$

and

$$r = \rho - d\,(1 + \rho'^2)^{-1/2}.$$

Here d can be the variable sum of several thicknesses, should a multi-layer dome be under consideration. Finally

$$\rho' = a\,\varphi \sin^2 \varphi\,(\varphi - \frac{1}{2}\sin^2 \varphi)^{-1/2}/\sqrt{\pi}$$

where

$$\varphi = -2L^{-1}\{1 - [(2t/L) - 1]^2\}^{-1/2}$$

Next a ray is specified, because

$$\frac{x - x_p}{a_R} = \frac{y - y_p}{b_R} = \frac{z - z_p}{c_R}\,. \tag{12}$$

(x_p, y_p, z_p) is a typical point and (a_R, b_R, c_R) are direction cosines of the ray.

The simultaneous solution of equations 10 and 12 is required for the point of intersection of ray and radome. We have

$$\left[\frac{b_R}{a_R}\left\{\left[t + \rho' d\,(1 + \rho'^2)^{-1/2}\right] - x_p\right\} + y_p\right]^2 + \left[\frac{c_R}{a_R}\left\{\left[t + \rho' d\,(1 + \rho'^2)^{-1/2}\right] - x_p\right\} + z_p\right]^2 =$$

$$\left[a\sqrt{\pi}\left\{\cos^{-1}\left(\frac{2t}{L} - 1\right) - \frac{1}{2}\sin\left[2\cos^{-1}\left(\frac{2t}{L} - 1\right)\right]\right\}^{1/2} - d\,(1 + \rho'^2)^{-1/2}\right]^2 \tag{13}$$

This equation is solved numerically for t. From t, x is found from equation 11. Next y and z are found from equations 12.

So far a point has been found. At this point the normal to the surface is found, a right handed coordinate system is formed with two axis in the plane of incidence and a third perpendicular so that the incident electric field can be analyzed into parallel and perpendicular components. In fact for direction cosines of the normal we have

$$a_N = -\rho\rho'(\rho^2 + \rho^2\rho'^2)^{-1/2}$$

$$c_N = \pm(1 - a_N^2)^{1/2}\ [1 + (y/z)^2]^{-1/2}$$

$$b_N = y\, c_N/z\ ,$$

where all quantities are evaluated with the value of t found from equation 13. The ray and the normal to the surface define a third vector $(a_\perp, b_\perp, c_\perp)$ perpendicular to the plane of incidence. Thus the polarization angle is found because

$$\cos X = \sin \Lambda = a_E a_\perp + b_E b_\perp + c_E c_\perp\ .$$

Specific orientations of antenna and radome will be described later through the coordinate system of Figure 3.

4. CALCULATIONS BASED ON THE FLAT SHEET APPROXIMATION

Calculations were made, using the theory described in section 2, of the RF phase difference between diagonally opposed quadrants of the antenna by first tracing rays to each of the slots in each quadrant. The result was a complex valued RF field for each quadrant. The phase of this field for a given quadrant was compared with the phase for a diagonally opposed quadrant. The response function for each quadrant is given in Table I[4]. All line lengths of slots were assumed equal.

Table I Aperture Response Function

Slot #	Response Function
1	1.00
2	.751
3	.246
4	.924
5	.704
6	.268
7	.773
8	.545
9	.296
10	.240

Calculations were made for the antenna displaced, relative to the radome, both horizontally and vertically. These displacements are called azimuth and elevation

gimballing henceforth. Calculations were done at angles of 6°, 12°, and 18° between the radome and antenna axes for each plane of motion. Radome thickness was varied from $0.2269\,\bar{\lambda}_o$ to $0.2394\,\bar{\lambda}_o$, $\bar{\lambda}_o$ being the free space wavelength at the center of the frequency band of interest. Incident wavelength was also varied 5% above and 5% below the mid-band wavelength. In Figure 4 are shown computed values of the phase difference between quadrants for the three frequencies as well as the average difference, averaging being over the three frequencies.

It should be explained here that these calculations were made, for a particular gimbal angle, by assuming one plane wave incident along the axis of the antenna. No spread of angles was used as is done in calculating boresight error from antenna patterns.[2]

Now considering Figure 4, it can be seen that frequency averaging results in lower errors than the values computed for the extremes of the frequency band. This is quite reasonable since, near a good design thickness, errors reverse in sign through the band. Somewhat more interesting is that the mean error is lower in most cases than the error at the center of the band.

In addition to the phase difference between quadrants, the calculation of the resultant field leads to a calculation of the fraction of incident energy received by the radome, i.e., its transmission efficiency.

5. MEASUREMENTS [5]

Measurements were of two kinds. The first was of transmission percentage. Apparatus consisted of a klystron source energizing an antenna which illuminated the antenna housed by the radome. Without the radome in place a reference level was set on received power. With the radome over the antenna, power received in a quadrant was recorded continuously.

First for a radome of thickness $0.2346\,\bar{\lambda}_o$, $\bar{\lambda}_o$ being the thickness at the center of the frequency band of interest, measured and computed power is shown in Figure 5.

Most striking is the reception of over 100% of the incident power for a range of angles in both azimuth and elevation. Note the polarization dependence,with much more pronounced excess for elevation or predominantly parallel polarization than for azimuth. The assymmetry with angle seems caused by the fact that each quadrant is displaced from the radome axis. Calculations agree with measurements to within 5% for azimuth. For elevation, calculations and measurements differ more, by about 10%. In general, the form of the measured and computed curves agree. The measurements were made at the mid-band wavelength $\bar{\lambda}_o$.

Such measurements were made again with a thicker radome, mechanical thickness being $0.2394\ \bar{\lambda}_o$. These measurements were made at the low end of the band so that the radome thickness was $0.228\ \lambda_o$ with λ_o being the test frequency. Recall in the previous case the wall thickness was $0.235\ \lambda_o$, λ_o being the test frequency. This second radome presents a smaller thickness in terms of incident wavelength.

Results obtained are shown in Figure 6. These results are similar to those in Figure 7. Again, greater variations exist for elevation gimballing. Measurements are shown for two quadrants in the elevation case. By symmetry identical results should have been obtained, but for the region such that transmission exceeded 100%, precision seems to be only to ±10%. Generally computed and measured results agree, but no prediction of over 100% is possible with the theory of section 2.

There seems to be quantitative evidence here for an inadequacy in the theory of section 2; however, because of the results in Figure 6 no entirely clear indication exists. A description will be given next of phase difference measurements which support the view that this ray theory is not completely adequate for radomes of dimensions about 6 wavelengths at the base. Note that each quadrant is a collecting aperture of only about 2 wavelengths on a side.

In Figure 7 are shown measured and computed phase differences between quadrants for azimuth gimballing. It can be seen from Figure 7 that the form of the measured results agrees with that computed. Magnitudes of measured phase differences indicate discrepancies with computed phase differences of about 50%; however, the

small magnitude of the effect is at the lower limit of accuracy of the measurement method. Here a precision phase shifter was used to compare phase of the two quadrants so that an accuracy of 2° in phase is all that can be claimed.

In Figure 8 there are shown measured phase differences between quadrants for elevation gimballing. Note the large values observed for gimbal angles of 18°. These measured curves agree for small gimbal angles with those computed with the theory of section 2, but disagree for larger angles. Such measured behaviour seems to be a fact having been found some years ago in an entirely different radome design at another frequency band.[6]

6. CALCULATIONS BASED ON A VERTEX SCATTERED WAVE

In these measurements two nearly equal signals are compared using a microwave hybrid junction. The difference of these signals is observed. If a hypothesis is made that there exists a relatively small signal in addition to that described by the theory of section 2, reduced discrepancies can be obtained. Such a hypothesis, motivated physically, is that the vertex scatters energy. Total internal reflection, producing surface waves which reradiate seems a reasonable means for supplying and removing energy. While the mechanism is not established it seems that the fields can be described as though a vertex wave exists. In fact, using such a wave, reduced discrepancies have been found between measured and computed patterns of a horn in a hollow wedge radome.[2]

Suppose the vertex scatters a wave of amplitude -0.052. Then for a quadrant of the antenna, add such a field to that computed for a quadrant by tracing rays as in section 2, taking into account the path from the vertex to the phase center of each quadrant. The resulting phase difference is computed and shown in Figure 8. It can be seen that this last curve agrees qualitatively with the result. The vertex wave was assumed independent of angle. A more realistic form might produce even smaller discrepancies. However, it seems that a more realistic description of performance

in this radome is produced by adding a vertex wave to the fields computed with the flat sheet theory. The magnitude =0.052 used above was chosen because of the results described in References 5 and 6. Notes that this is of the order of magnitude of the fraction of antenna area shadowed by the common volume of the radome walls at the vertex.

7. SUMMARY

A ray tracing method has been developed for application to radomes which are surfaces of revolution defined by von Karman ogive curves. An approximate description was made assuming the radome to be locally plane.

For single layer radomes, computed and measured transmission agreed moderately well. Discrepancies were polarization dependent, being about 5% for displacement of the antenna in azimuth and by 10% for elevation. Measured transmittance exceeded 1.00 for some angles for elevation displacements. Measured and computed boresight error agreed moderately well for azimuth. For elevation discrepancies were large, and measured results and computed results were qualitatively different. By introducing the hypothesis of a vertex scattered wave discrepancies were reduced, and correct qualitative agreement was obtained between measured and computed boresight error. Transmittance discrepancies were reduced also. While discrepancies are reduced by assuming the field to be a plane wave on which is superimposed a spherical wave of small magnitude, this description does not provide justification for a scattering mechanism. Surface wave excitation and propagation may be the most reasonable explanation.

8. ACKNOWLEDGMENTS

The help of several people is acknowledge. Programming was done by William Talty and Ruth Hayward of the General Dynamics Astronautics' Computer Laboratory. Line drawings were made by J. Austin. Typing was done by F. Lowe and V. Woelber.

9. FOOTNOTES

1. G. Tricoles, Proceedings OSU-WADD Electromagnetic Window Symposium, June 1960

2. G. Tricoles, Jour. Opt. Soc. Am., 53, P. 545 (1963)

3. All computations are done numerically.

4. These data were provided by J. McSweeney of General Dynamics-Pomona.

5. These measurements were made at General Dynamics-Pomona mainly by Mr. D. Gellman.

6. G. Tricoles - Proceedings Ohio State Univ. - WADD Electromagnetic Window Symp., June 1960.

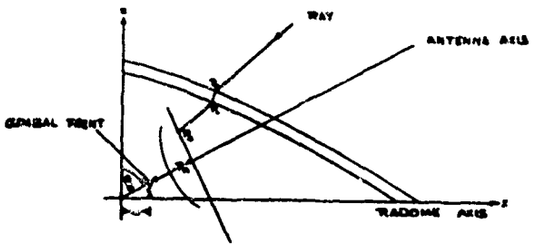

Figure 1. Ray Tracing Geometry

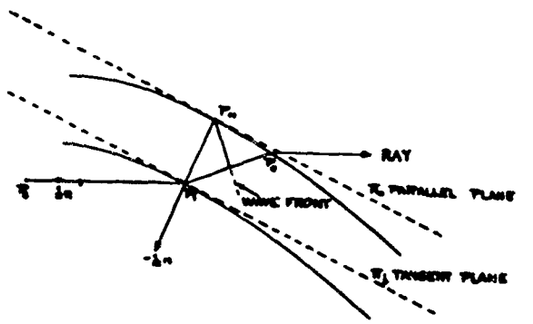

Figure 2. Plane Sheet Geometry

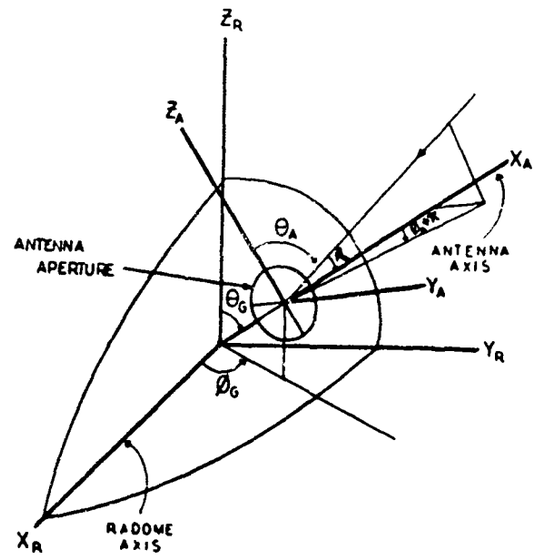

Figure 3. Coordinate Systems

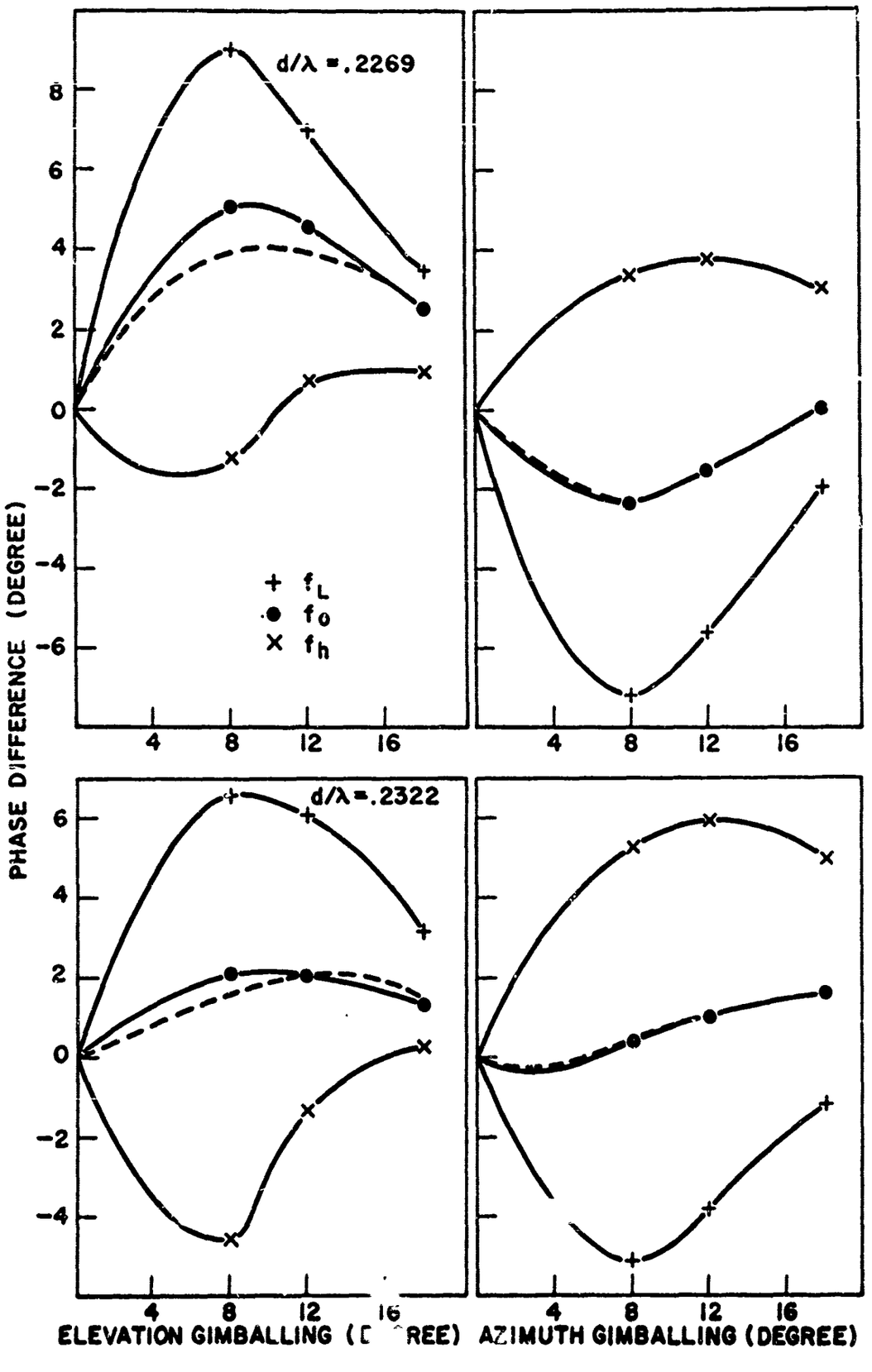

Figure 4. Computed phase difference between quadrants A&D for radomes of thickness .2269 $\bar{\lambda}_o$ and .2322 $\bar{\lambda}_o$.

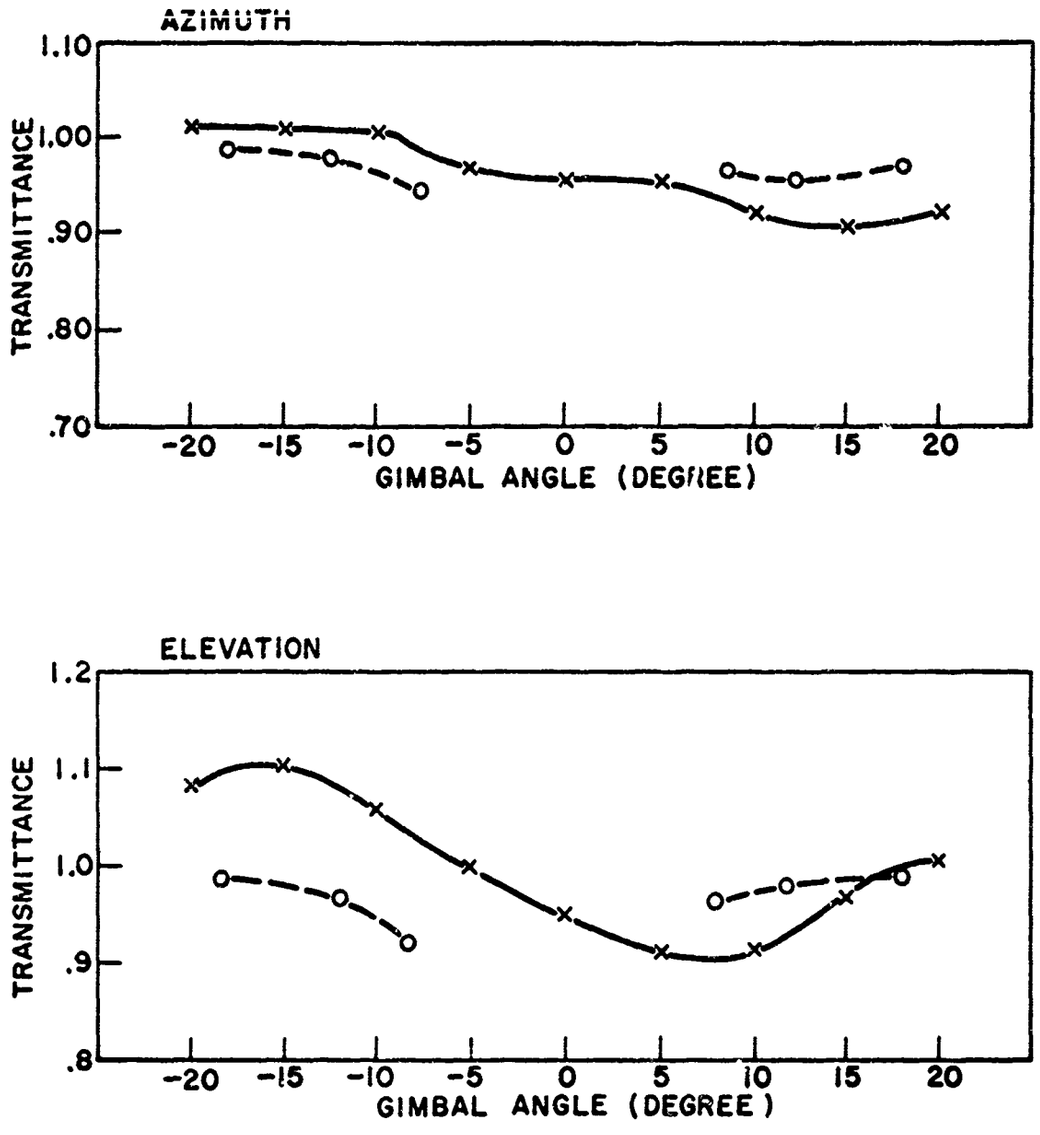

Figure 5. Measured and computed power transmission coefficient for quadrant A at the mid-band frequency. Radome thickness was .2269 $\bar{\lambda}_o$.

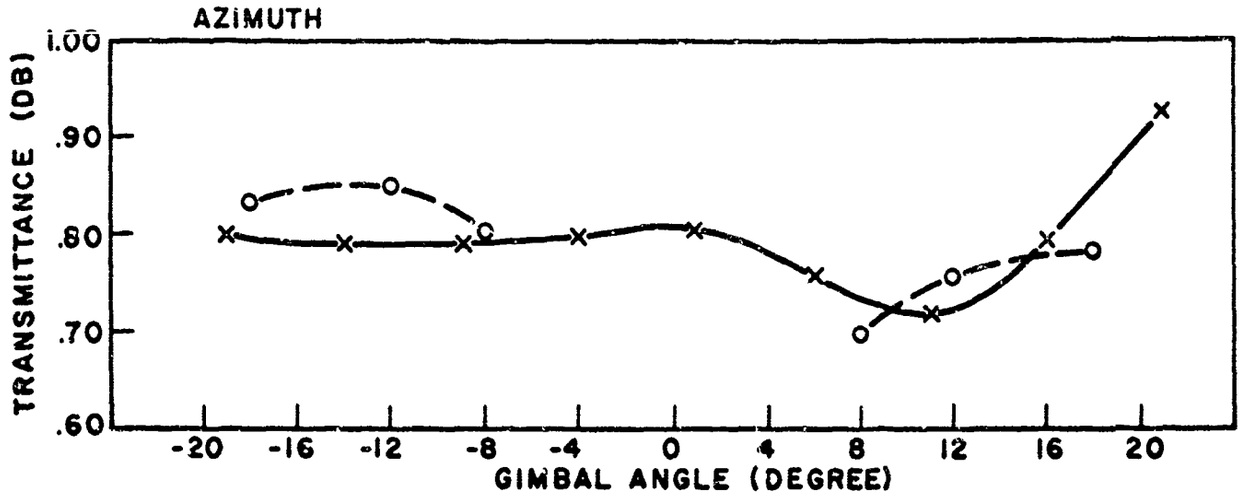

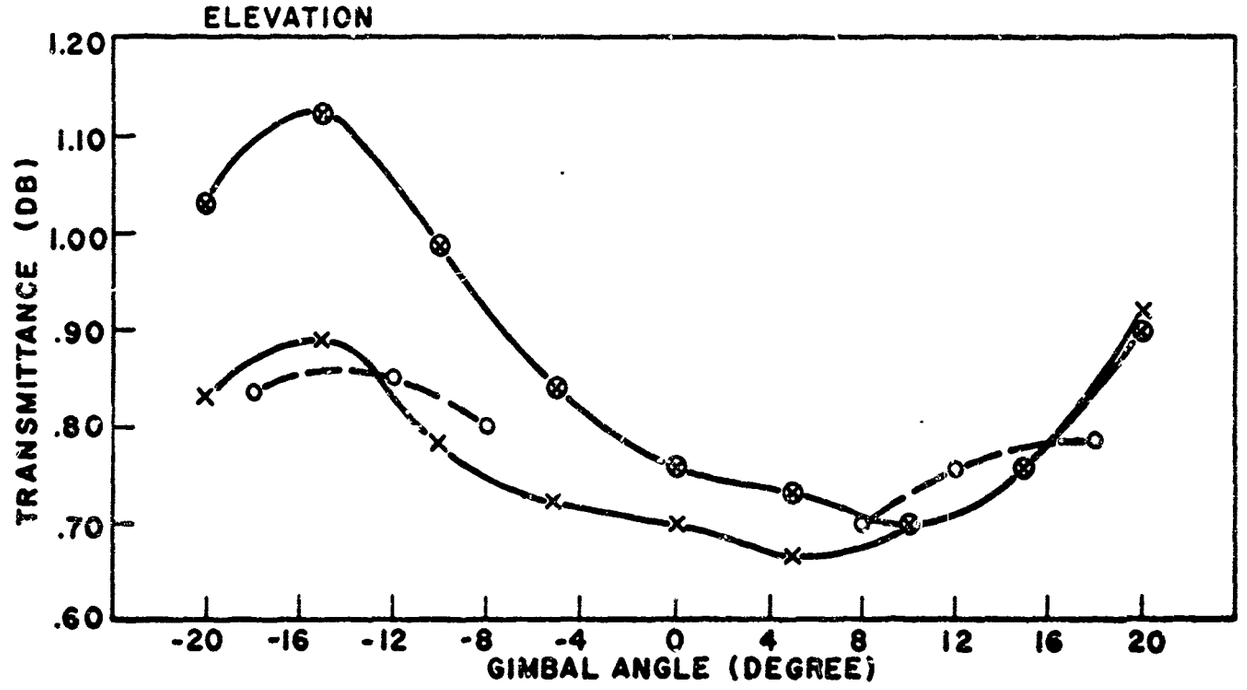

Figure 6. Measured and computed power transmission coefficient for quadrant A at the lowest frequency in the band. Radome thickness was .2322 $\bar{\lambda}_o$. The crosses denote measured data. The open circles denote computed data.

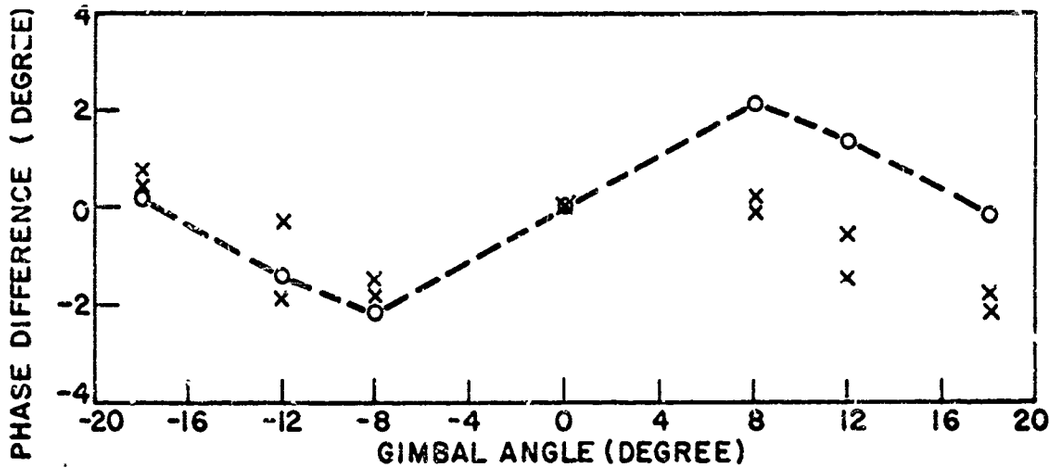

Figure 7. Measured and computed phase difference between quadrants A&D for azimuth. The crosses denote measured data.

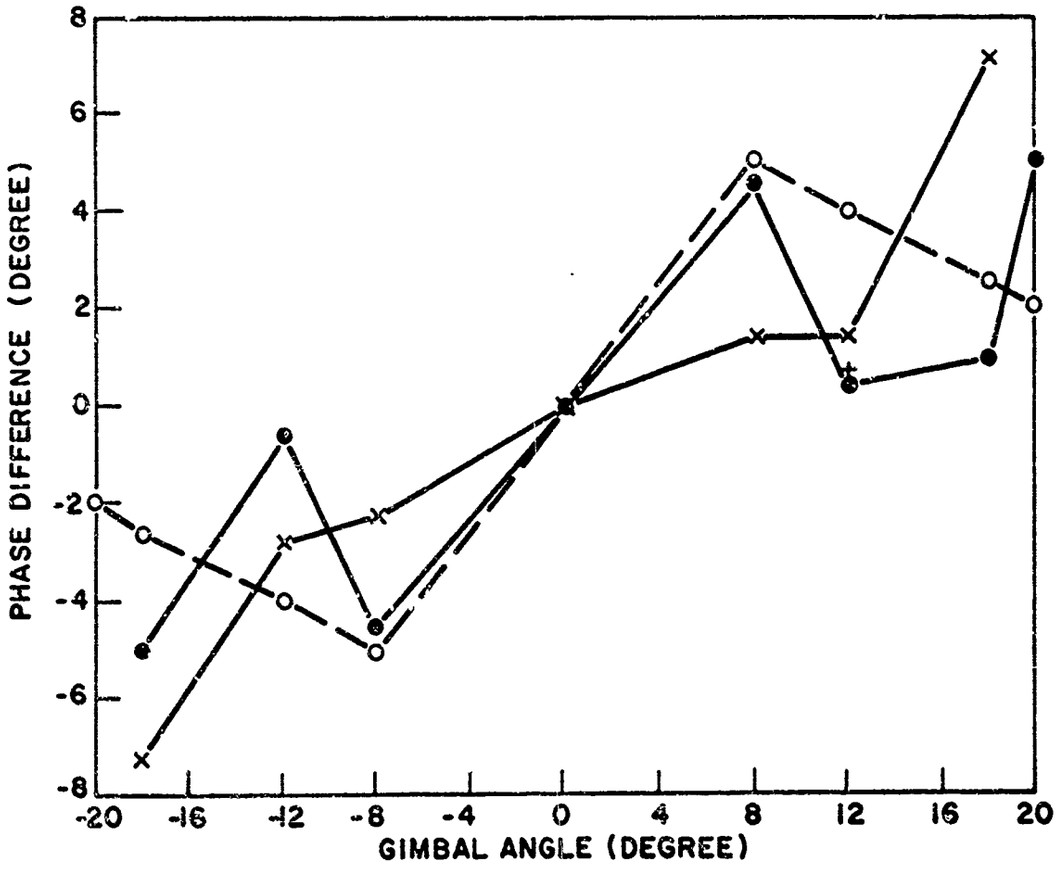

Figure 8. Measured and computed phase difference between quadrants A&D for elevation. Measured data is denoted by crosses. The open circles denote calculations on using the flat sheet assumption. The dots indicate data computed on assuming a spherical wave from the vertex. The radome thickness was 0.2269 λ_0 and measurements were made at the mid-band frequency.

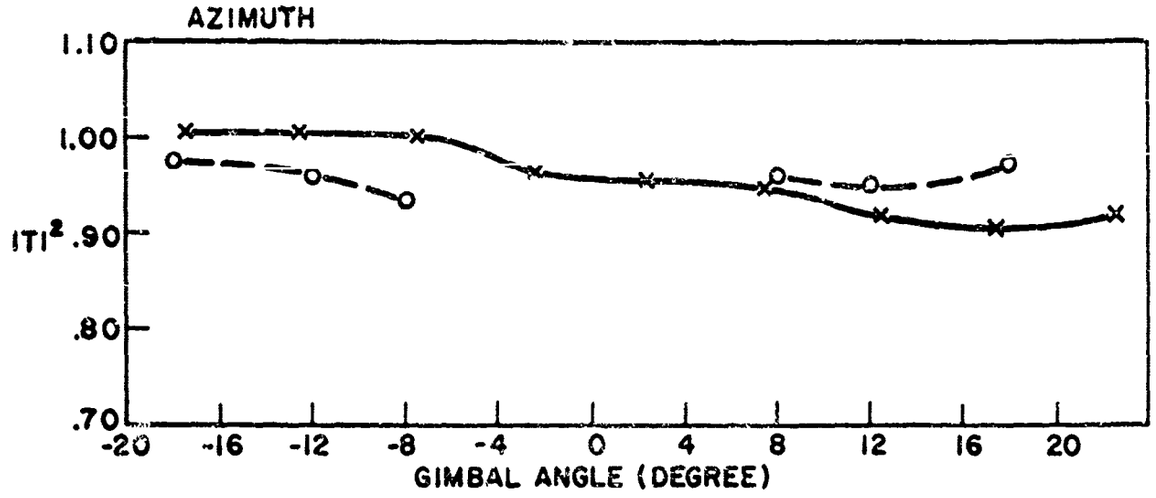

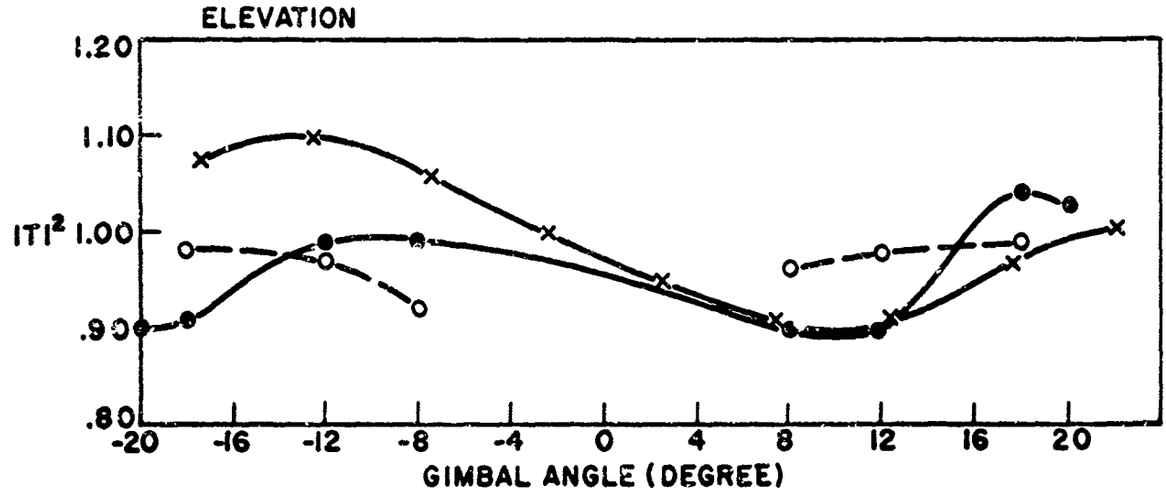

Figure 9. Measured and computed power transmission of a radome of thickness 0.2269 $\bar{\lambda}_o$. Open circles are for data computed with a vertex wave. Dots are for calculations made on assuming a vertex wave. The cross denotes measured data.

RADOMES FOR MICROWAVE APPLICATIONS

BY

A. G. HOLTUM, JR. & K. E. MCKEE

FOR

OSU - RTD SYMPOSIUM

ON

ELECTROMAGNETIC WINDOWS

JUNE 1964

RADOMES FOR MICROWAVE APPLICATIONS

By

A. G. Holtum, Jr.
Director of Antenna Design
Andrew Corporation, Chicago, Illinois

and

K. E. McKee
Director of Mechanical Design
Andrew Corporation, Chicago, Illinois

ABSTRACT

This paper describes and reviews radomes used for commercial microwave relay antennas. The technical requirements and related electrical and mechanical parameters are reviewed for a variety of radome types. Included are a summary of the design criteria and decisions with which the radome designer must become involved, together with tests, both electrical and mechanical, which are used to evaluate the material and the finished configuration. Attention in the paper includes loss, effect on VSWR, and effect on the radiation pattern of various radome configurations, materials, and material variations. With regard to mechanical aspects, wind, snow and falling ice are considered. The radomes considered range in size up to 15 ft. in diameter and are designed for frequencies from 2 GC to 12 GC.

I. INTRODUCTION

Some of the least esoteric forms of electromagnetic windows are radomes used in connection with microwave communication systems. Because of the commerical nature and relatively long history of this type of radome, a state of relative design stability has been reached. Current research and development for such radomes is concerned with improved electrical and/or mechanical performance, increased sizes, higher frequencies, and manufacturing costs. The question here is not can it be done, but rather what is the best way to do the job.

A radome is a shelter used to protect an antenna from the environment while allowing the antenna to operate. In the case of microwave radome, this environment is the relatively modest conditions associated with being out-of-doors. Consideration herein will be limited to radomes used on parabolic antennas which protect the feed and all or part of the antenna surface.

Specifically excluded from consideration are the larger bubble or space frame which encloses the entire antenna system. The information contained in this paper is applicable to this latter type of radome, but the specific details are different. Attention in this paper is therefore devoted to radomes which attach to the parabola and cover the antenna surface and feed. Figures I-1 and I-2 show examples of such radomes.

A radome for microwave application must resist conditions which would be encountered in actual service. Since we are considering a commercial product the design philosophy is to provide with a single design for the full range of likely or specified conditions. The actual design is a compromise of electrical performance, mechanical requirements, and cost. The final selection of the parameters for which a radome is designed depends on this compromise and obviously can vary substantially depending on the system requirements, customer, salesman, and other factors.

It is interesting to note that even the decision to use a radome is the basis of an optimization and compromises by the system engineer. Alternates in use include no protection, heated feeds, and heated dishes. As a matter of fact radomes are used on only about one-third of the microwave antennas. In the remainder of this introduction a tabulation of some of the design parameters effecting radomes will be made including a limited comment on each.

Windloads

One of the environmental conditions which must be resisted is the wind. Various wind velocities can be used for design with 100 mph being a reasonable level for most of the continental United States. It is interesting to point out that the presence of a radome on an antenna reduces the net force on the antenna due to wind and hence may reduce tower requirements and costs.

Ice and Snow

Accumulation of snow and/or ice on an antenna or radome causes a degrading of the signal. The presence of a radome minimizes this problem since it provides a shape less likely to accumulate ice or snow than an unprotected antenna. In addition, radomes may be heated to provide deicing or anticing protection or may be made flexible to discourage ice formation.

Falling Ice

For horizontally mounted antennas, ice falling on the radome can be a serious design input. Protection may be provided by the radome or an extra ice screen may be provided.

Accumulated Debris

Unprotected antennas, particularly those oriented horizontally, can serve as collectors for debris. Old newspapers, leaves, etc. may collect in the dish. Radomes minimize this possibility.

VSWR

Presence of the radome tends to reflect radiated energy from the antenna back into the antenna or by reciprocity, energy that might have been received by the antenna back into space. Its effect is to increase (degrade) the voltage standing wave ratio. To reduce this effect the radome must be designed so as to reflect as small amount of the electromagnetic energy impinging upon it as possible.

Radiation Patterns

The presence of the radome tends to reflect, scatter and absorb electromagnetic energy. Depending upon the severity of its effect, the radiation pattern of the antenna-radome combination will be altered. The design of the radome must be accomplished, therefore, to make it as trans-

parent or "invisible" as possible to the spectrum of electromagnetic energy being transmitted or received by the antenna.

Gain

This parameter is tied in with both the VSWR and the radiation pattern of the antenna-radome combination. The gain of an antenna is a function, in general, of its ability to radiate electromagnetic energy into space in as narrow a beam consistent with its aperture size as possible. The tendency of the radome to reflect, scatter and absorb a portion of this electromagnetic energy causes a degradation of the gain. Again, it behooves the antenna designer to make the radome as invisible as possible while retaining mechanical adequacy to satisfy the environmental parameters. He must effect these appropriate comprovises of conflicting requirements within the framework of economic feasibility.

This paper is divided into six sections. Section II discusses various types of microwave radomes. Section III describes electrical parameters and Section IV discusses electrical tests. Section V considers mechanical tests, including using examples. Finally, Section VI summarizes the state-of-the-art regarding microwave radomes. The Bibliography is collected at the end of the paper.

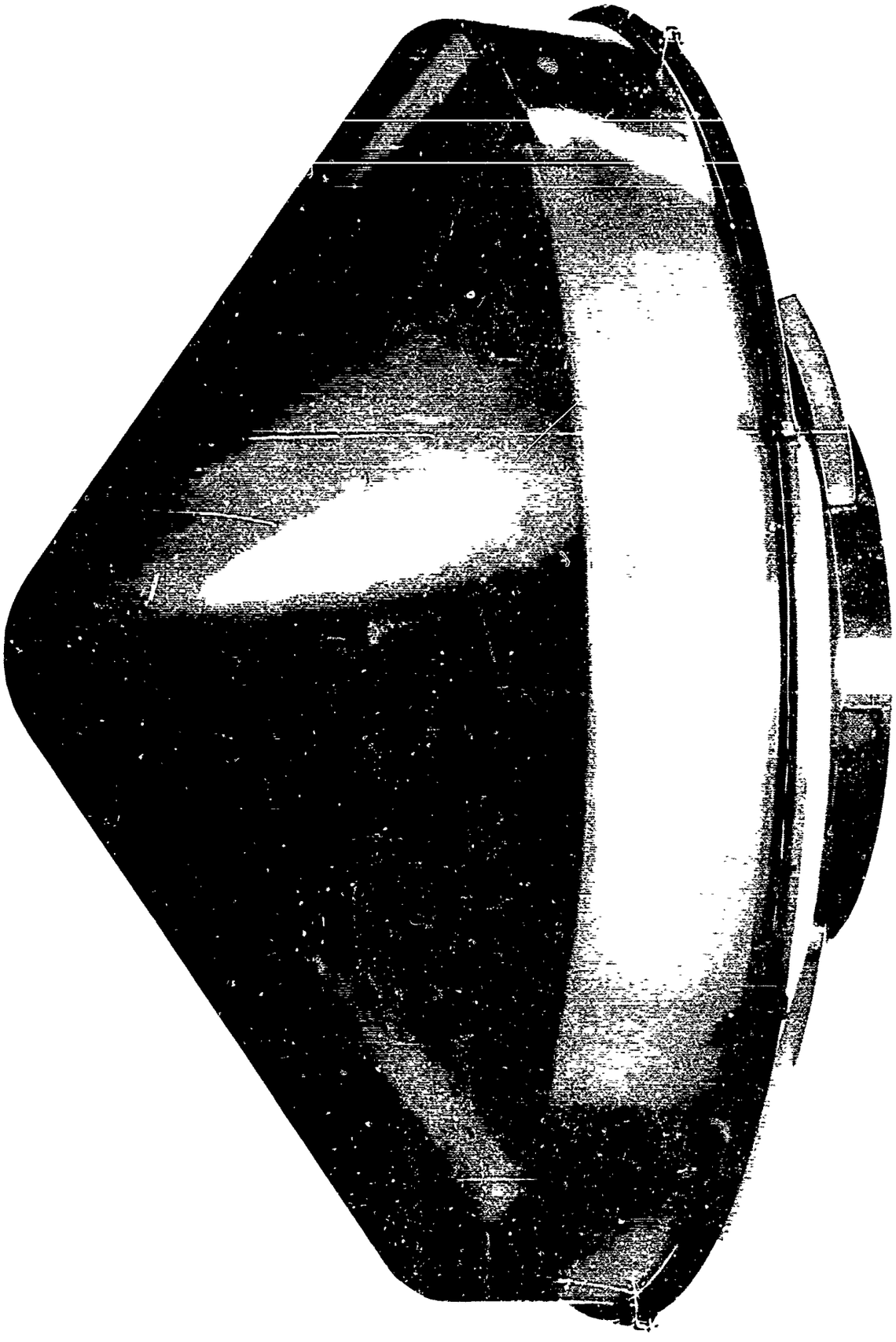

Rigid (Single Wall) Fiberglas Radome

Fig. I-1

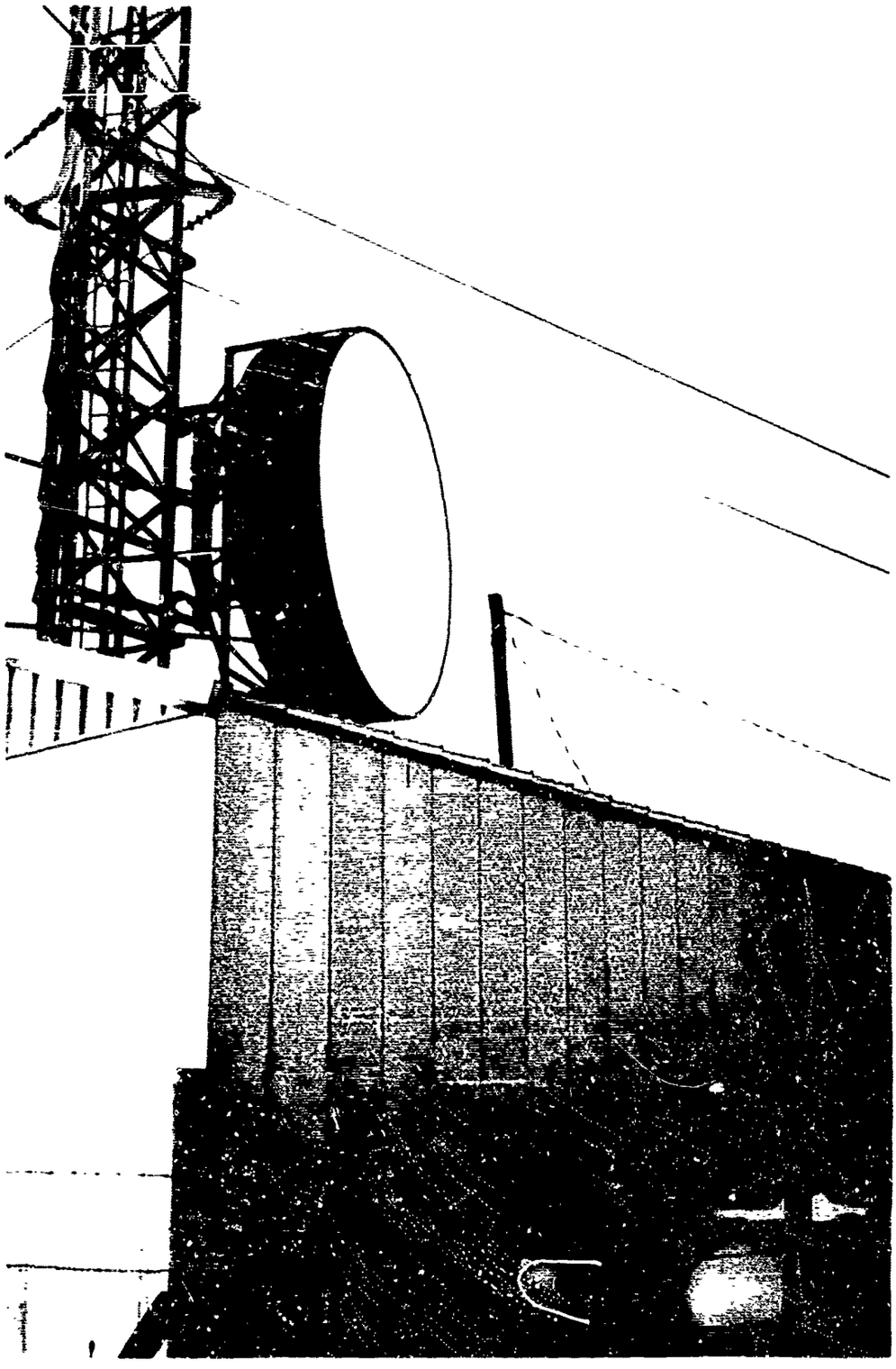

Membrane Type (Flat) Radome

Fig. I-2

II. RADOME TYPES

It is convenient for the purposes of discussion to consider three generic classes of radomes: rigid, flexible, and semi-rigid. Many types are in fact some combination or subclassification of these three. Under each classification some of the possible variations will be mentioned.

Rigid Radome

Figure I-1 is an example of a rigid radome. By rigid, reference is made to construction which is self-supporting and which carries the full load. The radome picture in Fig. I-1 is sprayed-up Fiberglas. This type of construction depends on radomes made of low loss materials which have sufficient strength and stiffness to carry the loads. Obviously, the larger the antenna the more difficult it is to carry the load and hence the thicker the radome must be if the same material is used and therefore the greater the loss. There is obviously no limitation, other than strength, electrical characteristics and environmental requirements to the materials which can be used for the radome. In practice, Fiberglas sprayed-up or hand layed-up has been more common with other dense plastic also being used and more recently radomes being made of foamed plastics.

The conical shape as illustrated by Fig. II-1 has been commonly used although there is no fundamental limitation. Hemispherical radomes as sketched on Fig. II-2 have also been used. Current development on high performance antennas is also considering the use of a flat plate rigid radome as sketched on Fig. II-3. Radomes normally cover the entire antenna, but occasional use has been made of radomes covering only a portion of the surface, see Fig. II-4. This technique may be particularly useful for larger antennas although the configuration has some of the disadvantages of the unprotected antennas, e.g. wind forces and pockets for the accumulation of snow or debris.

Flexible Radomes

By flexible radomes, reference here is made to membrane-like material, e.g., Hypalon. The classical example of such radomes are the large air-inflated used to protect entire antenna systems. This concept has been discussed for microwave applications, i.e., an air inflated bubble covering the antenna surface but to the best of the

authors' knowledge has never been used. The reasons for this lack of use include the need for a continually running blower and the possibility of malfunction due to relative modest damage to the radome. Since many microwave antennas are located at remote sites these features make the reliability questionable, and hence have been the basis for rejecting this approach. A membrane-type radome which has been used on a large number of antennas is shown on Fig. I-2 and sketch on Fig. II-3. The membrane here is a flat membrane placed over a shrouded high performance antenna. The wind load is taken here by deflections of the membrane and no internal pressure is required.

Semi-Rigid Radome

Both rigid and flexible radomes depend on making the entire radome of a dielectric material suitable for electrical transmission. Particularly, for large antennas and/or extreme environments the structural requirements are inconsistent with the electric requirement. In these instances, a supporting structure which hold suitable dielectric material can be used--this is referred to as semi-rigid. The actual construction can use a metal or plastic frame to which membrane or suitable rigid plastic sheets are attached. Fig. II-5 shows a picture of a 15 ft. antenna with a tepee type Hypalon radome. The Hypalon is supported on eight aluminum struts. Alternate approaches can make use of three dimensional space frames to support the dielectric material. The actual material in the supporting structure can be aluminum, steel, or dielectric. One other approach which has been used when improved electrical performance is required is to use a rigid radome as shown in Fig. I-1, remove segment of this radome and cover the holes with a membrane type material.

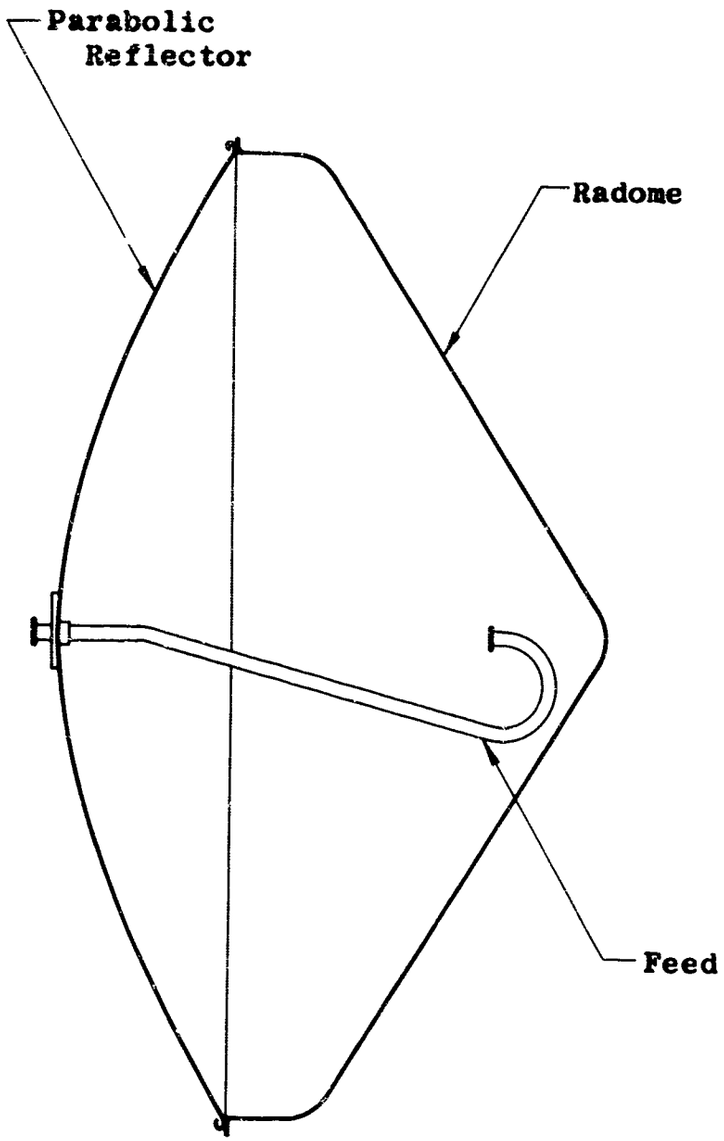

Rigid Radome

Fig. II-1

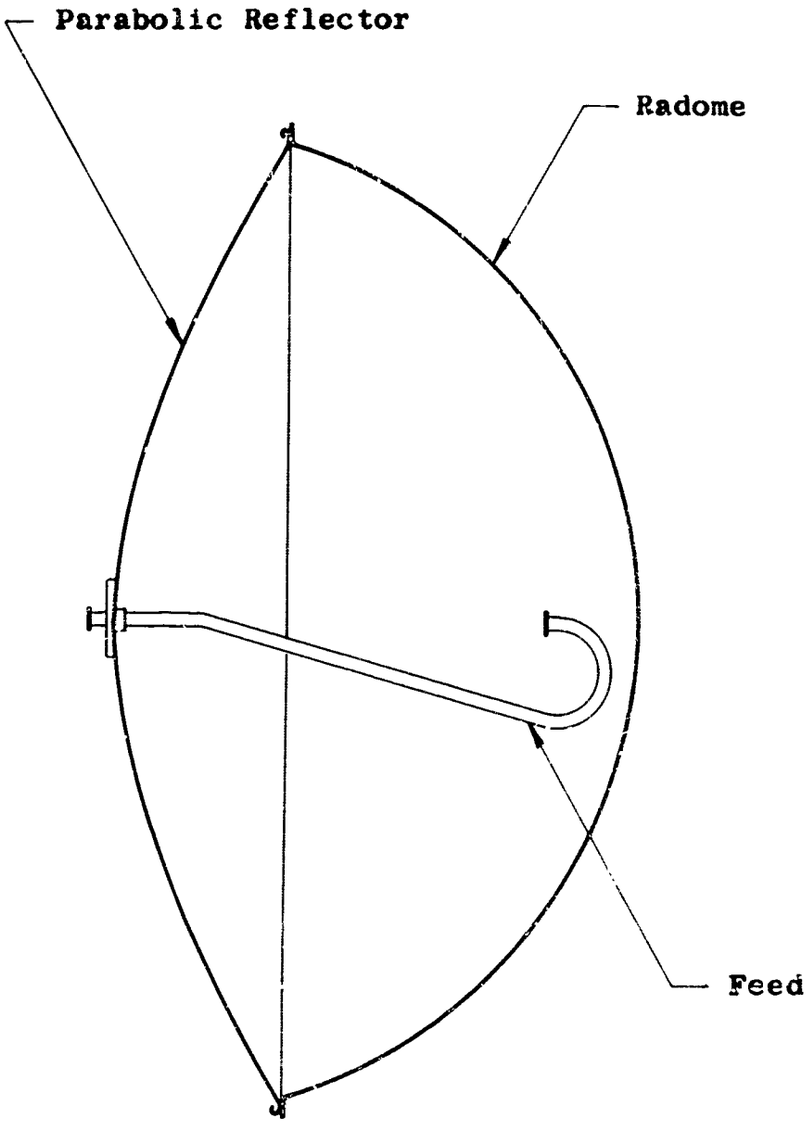

Spherical Radome

Fig. II-2

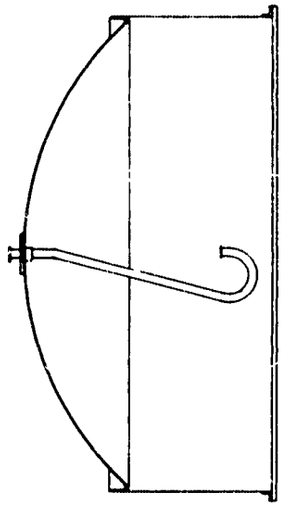

Flat Rigid
Radome

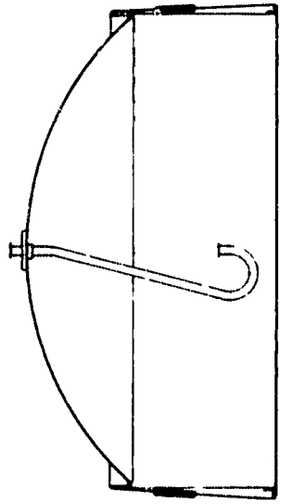

Flat Membrane
Radome

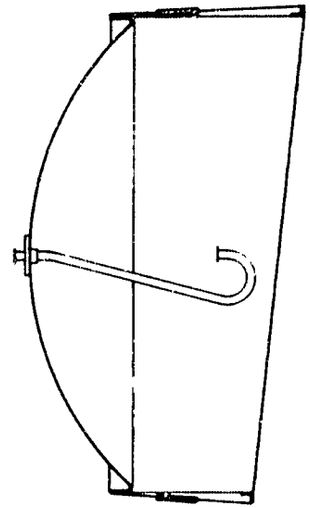

Flat Membrane Radome -
Tilted to Mitigate Effect
on VSWR

Flat Radomes

Fig. II-3

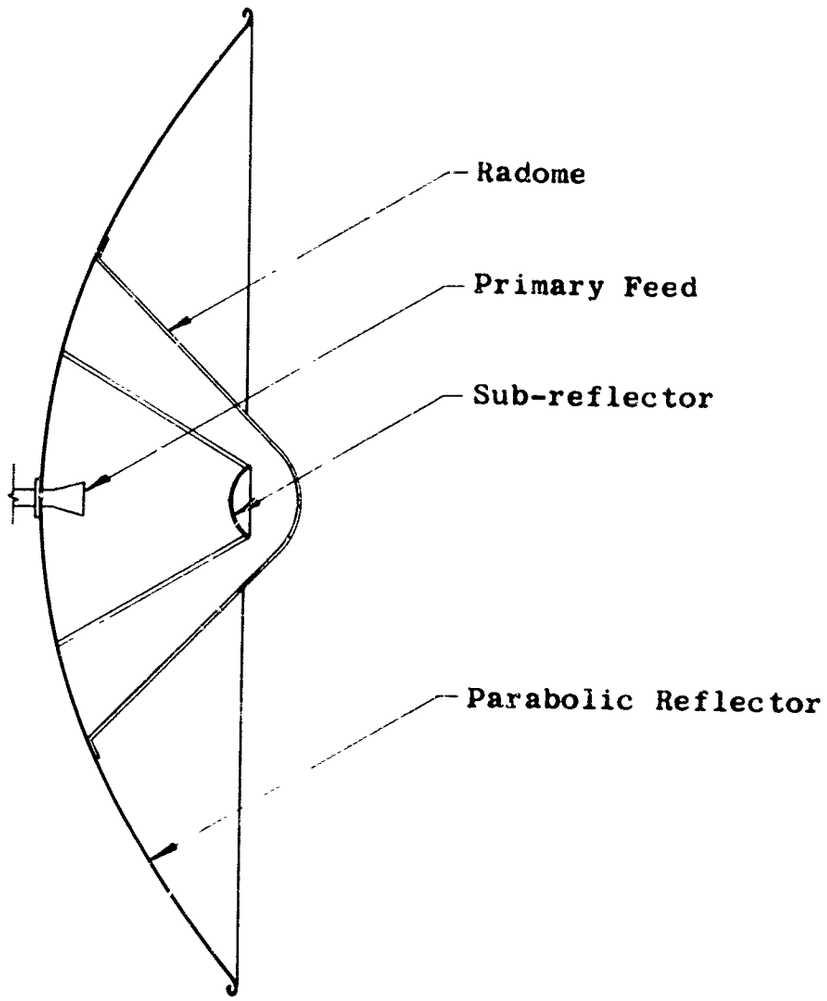

Partial Radome

Fig. II-4

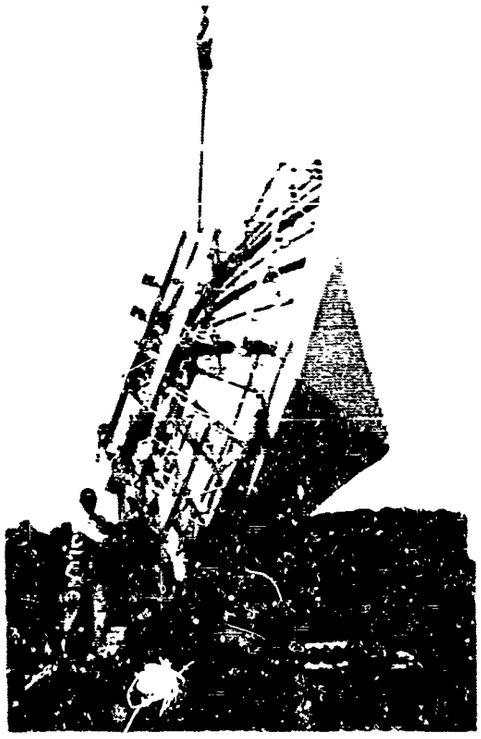

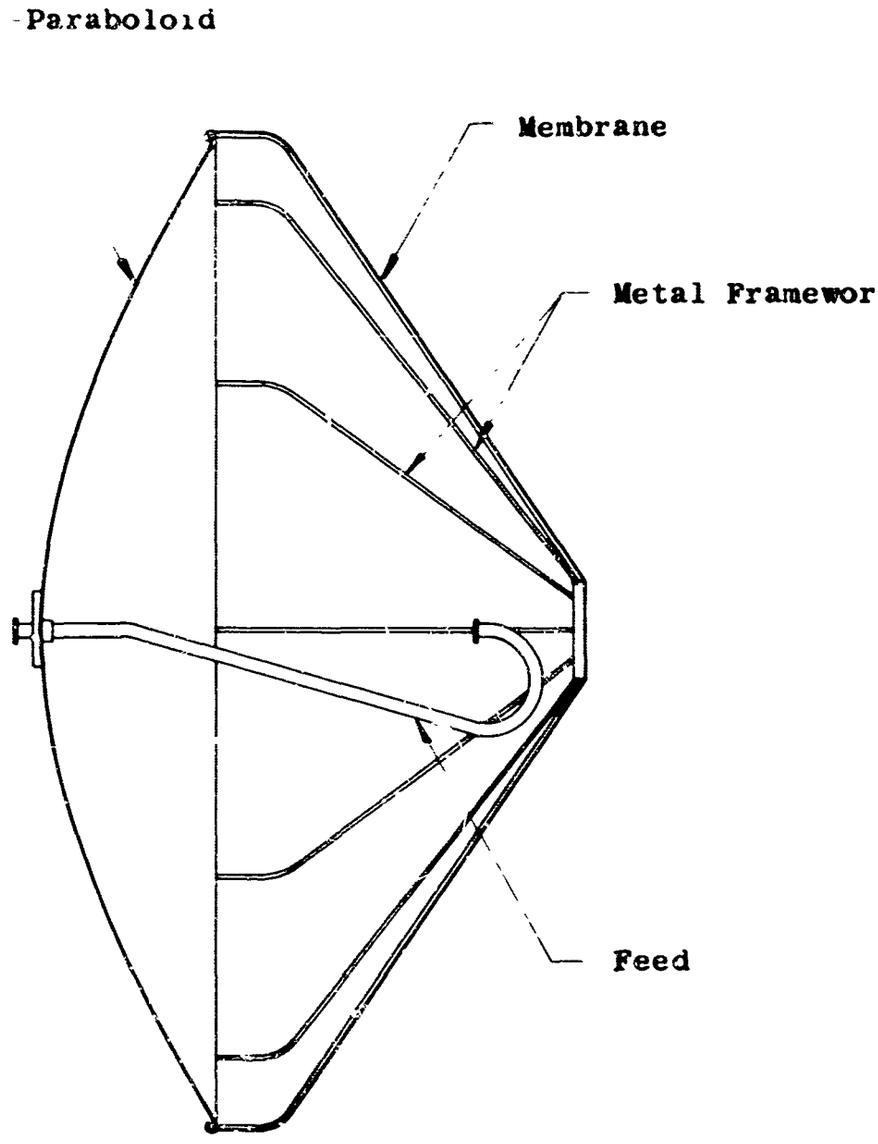

Membrane Supported by Metal Structure
"Tepee Type"

Fig. II-5

III. ELECTRICAL PARAMETERS

An ideal radome would be one which was invisible to the electromagnetic energy incident upon it. The ideal radome is, of course, not realizable because of its tendency to reflect (scatter), refract, and absorb a portion of the energy incident upon it. The radome designer must, by means of techniques and materials available to him, minimize the reflection, refraction and absorption to effect maximum transmission with the least perturbation of antenna pattern. He minimizes the reflection by proper choice of dielectric constant and thickness of the radome wall. He minimizes absorption by a choice of material
work which has a low conductivity or loss tangent at the frequency of operation. The refraction and pattern perturbation is kept to a minimum by the use of a configuration of uniform thickness which keeps the angle of incidence near normal incidence. The effect of these factors, viz., reflection, refraction and absorption, is to reduce the gain of the antenna. The goodness or merit of a radome is usually expressed, therefore, in terms of loss in db it imposes on the antenna it protects.

The literature[1,2] contains many techniques and approximations for the relationship of the reflection and transmission coefficients of the radome wall to the complex dielectric constant of the material of which the radome is fabricated. These basic relationships will be summarized and their relevancy discussed in the next few paragraphs.

Loss Due to Reflection

The reflection coefficient is a measure of the ratio of field strength reflected to the field strength incident on a given surface or discontinuity. In the case of the wave traveling from free space or air and impinging on an infinite slab of dielectric, see Fig. III-1a, the reflection coefficients for the cases of the electric vector being perpendicular to the plane of incidence and parallel to the plane of incidence may be expressed:

$$\frac{E'_\perp}{E_\perp} = R_\perp = \frac{\cos i - \sqrt{k_* - \sin^2 i}}{\cos i + \sqrt{k_* - \sin^2 i}}$$

$$\frac{E'_{\parallel}}{E_{\parallel}} = R_{\parallel} = - \frac{k_* \cos i - \sqrt{k_* - \sin^2 i}}{k_* \cos i + \sqrt{k_* - \sin^2 i}}$$

where

$$k_* = \frac{\epsilon'}{\epsilon_o} - j \frac{\sigma}{\omega \epsilon_o}$$

$$k_o = 1$$

σ = conductivity in mhos/meter

$\epsilon_o = 8.85 \times 10^{-12}$ farads/meter

$\omega = 2\pi f$

f = frequency in cycles/second.

The magnitudes of these coefficients are plotted in Fig. III-1b for various values of k_*, where $k = \frac{\epsilon'}{\epsilon_o}$ for an ideal dielectric, $\sigma = o$.

For normal incidence the expressions above simplify to:

$$|R| = \frac{\sqrt{k_*} - 1}{\sqrt{k_*} + 1}$$

At normal incidence the reflection coefficient for a field parallel to the plane of incidence becomes the same as for the expression for the electric field perpendicular to the plane of incidence. The apparent ambiguity in sign can be resolved by examining the geometry. Fig. III-3 is a plot of the reflection coefficient of a semi-infinite dielectric at normal incidence assuming a loss tangent of 0 (or $\sigma = 0$), and various dielectric constants.

In the case of the radome wall the electromagnetic energy must travel from free space or air into the dielectric and then from the dielectric into free space again. In its journey it meets two interfaces or discontinuities as shown in Fig. III-2. The derivation of the expression which yields the reflection coefficient of the total reflected field to the incident field may be handled as a boundary value problem or a transmission line analogy[3]. At normal incidence it is:

$$R^{(T)} = \sqrt{\frac{2|R|^2\left[1 - \cos\frac{4\pi a}{\lambda}\right]}{1 - |R|^2 \quad 2\left[\cos\frac{4\pi a}{\lambda} - |R|^2\right]}}$$

Assuming symmetry, i.e., the reflections at the interfaces are equal; referring to Fig. III-2:

$$|R| = \frac{|E_1|}{|E|} = \frac{|E_{T2}|}{|E_{T1}|}$$

$$R^{(T)} = \frac{|E_R|}{|E|}$$

This particular expression relates the total reflection coefficient $R^{(T)}$ to the thickness of the radome wall and the reflection coefficient at the interfaces. It is plotted in Fig. III-4.

Fig. III-6 is a plot of the loss in db imposed by a radome wall at normal incidence, assuming a dielectric constant of 3.5 and a loss tangent of 0 for 6 GC and 12 GC, two common carrier bands.

Loss Due to Absorption

So far we have considered the loss due to reflection at or near normal incidence and not taking into account the absorption of the energy during its journey through the radome wall. To illustrate the effect of such absorption for various thicknesses of radome wall at normal incidence, Fig. III-5 has been plotted which graphs the percent transmission vs. the thickness of the radome wall in wavelengths for various values of the loss tangent. Note that for low loss materials it may be desirable to use a radome wall which is one-half wavelength in thickness. At 6 GC this would result in a wall thickness of about one-half inch which would be rather heavy and expensive; however, at frequencies of 12 GC and higher the thickness would be of the order of one-quarter inch or less, which might make it economically feasible. An obvious disadvantage of this technique is that it renders the radome more sensitive to frequency.

Loss Due to Refraction or Pattern Perturbation

For a radome wall of uniform thickness and uniform dielectric properties, the angle of arrival of an incident wave will equal to the angle of departure of that same wave after it has been transmitted through the radome. The effect of nonuniformity in wall thickness will be somewhat like that of a lens which, by virtue of its effect on phase, may send the energy off into unwanted directions. Care must be taken to maintain uniform thickness in the material used for the radome wall so that this does not happen.

Another source of error introduced by the phase shift is the multiple reflections occurring between the interfaces of the dielectric[2]. This error becomes more severe with increasing angle of incidence, as does the magnitude of the over-all reflection coefficient. The radome engineer strives, therefore, to maintain angles of incidence as close to normal as possible. A reasonable criterion is $i \leq 30^{o}$. On the other hand, for severe requirements the voltage standing wave ratio of the antenna, exact normal incidence is to be avoided because the reflected energy is sent directly back into the feed.

Other Configurations

So far we have considered radome walls consisting of a single layer of dielectric material. The limitations using such a configuration are that the dielectric constant, loss tangent, and thickness must be considered very carefully so that the combination will yield a structure which is mechanically adequate and yet be of minimal loss. Other techniques to reduce the reflection coefficient without a severe limitation on thickness are feasible electrically and mechanically and have been used in many applications w' re cost is not one of the primary considerations. Two of these special configurations are sandwich type radomes and foam type radomes. As the technology of materials advances and techniques of bonding become available to the microwave radome designer, he will incorporate these configurations to microwave radomes for commercial applications.

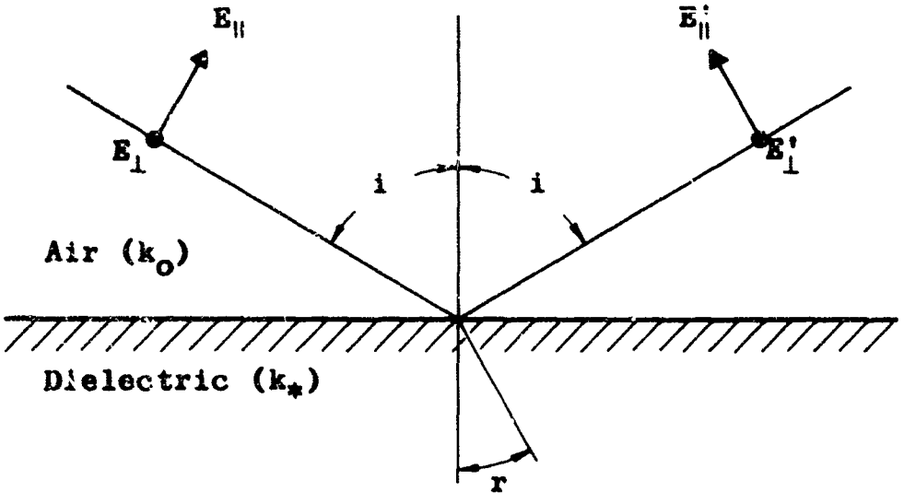

$$\frac{E'_{\perp}}{E_{\perp}} = R_{\perp} = \frac{\cos i - \sqrt{k_* - \sin^2 i}}{\cos i + \sqrt{k_* - \sin^2 i}}$$

$$\frac{E'_{\parallel}}{E_{\parallel}} = R_{\parallel} = - \frac{k_* \cos i - \sqrt{k_* - \sin^2 i}}{k_* \cos i + \sqrt{k_* - \sin^2 i}}$$

where

$k_* = \frac{\epsilon'}{\epsilon_o} - j \frac{\sigma}{\omega \epsilon_o}$

$k_o = 1$

σ = conductivity in mhos/meter

$\epsilon_o = 8.85 \times 10^{-12}$ farads/meter

$\omega = 2\pi f$

f = frequency in cycles per second

Reflection from Semi-Infinite Slab of Dielectric

Fig. III-1a

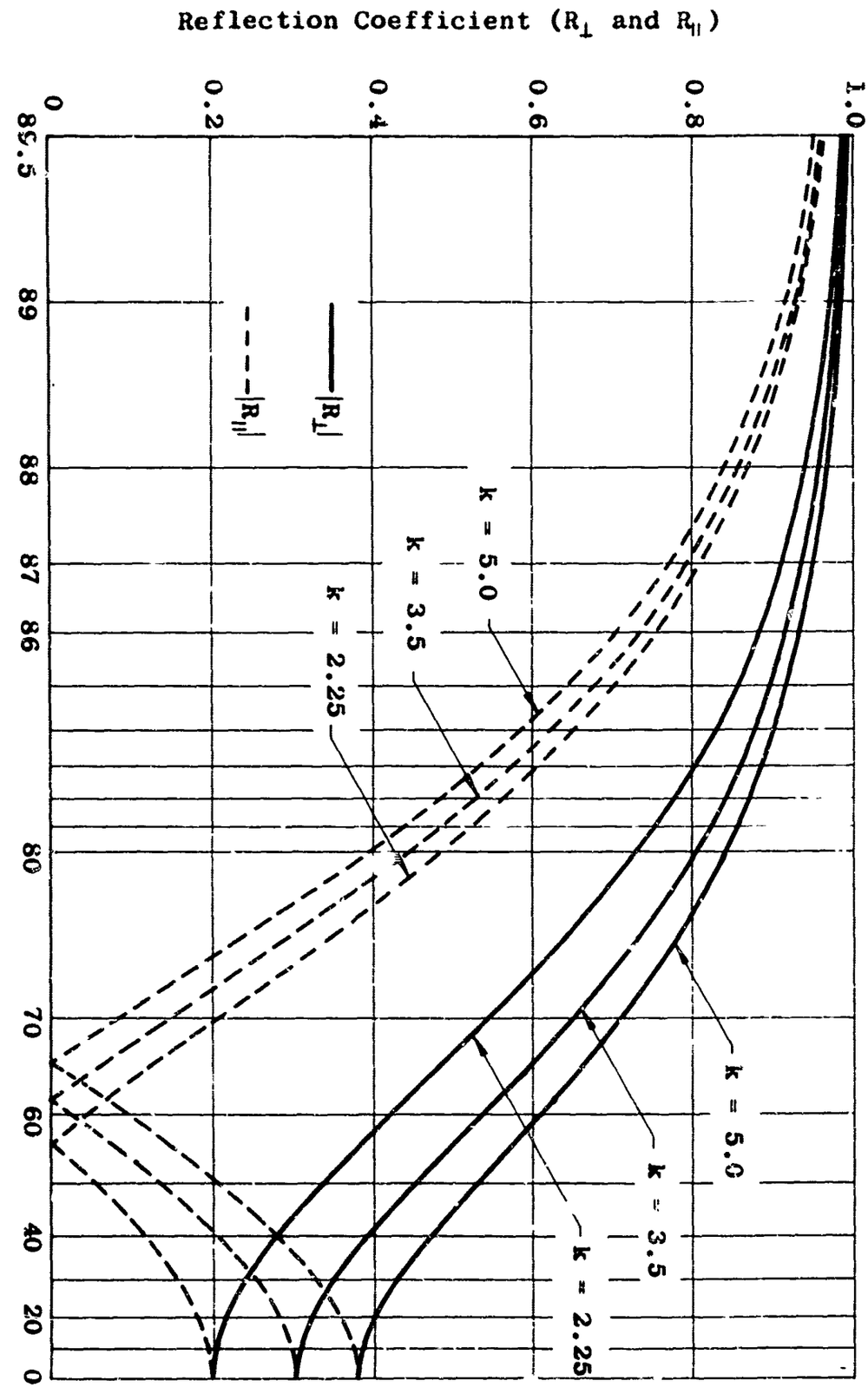

Reflection coefficient vs. angle of incidence for various dielectric constants assuming $\sigma = 0$, or $\tan \delta = 0$.

Fig. III-1b

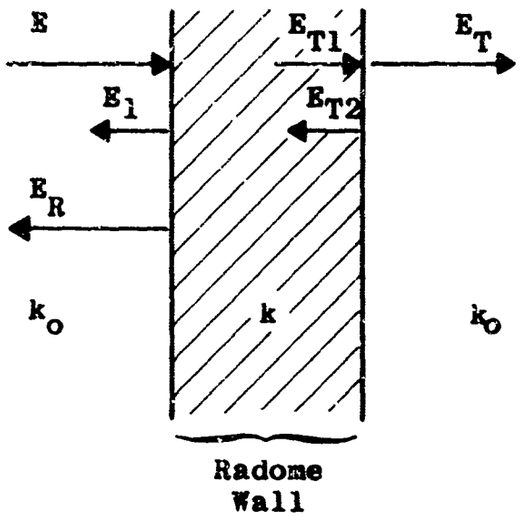

E = Incident electric field.

E_1 = Electric field reflected at first interface.

E_{T1} = Electric field transmitted through first interface.

E_{T2} = Electric field reflected at second interface.

E_T = Electric field transmitted through wall.

E_R = Total electric field reflected.

Surface Discontinuities

Fig. III-2

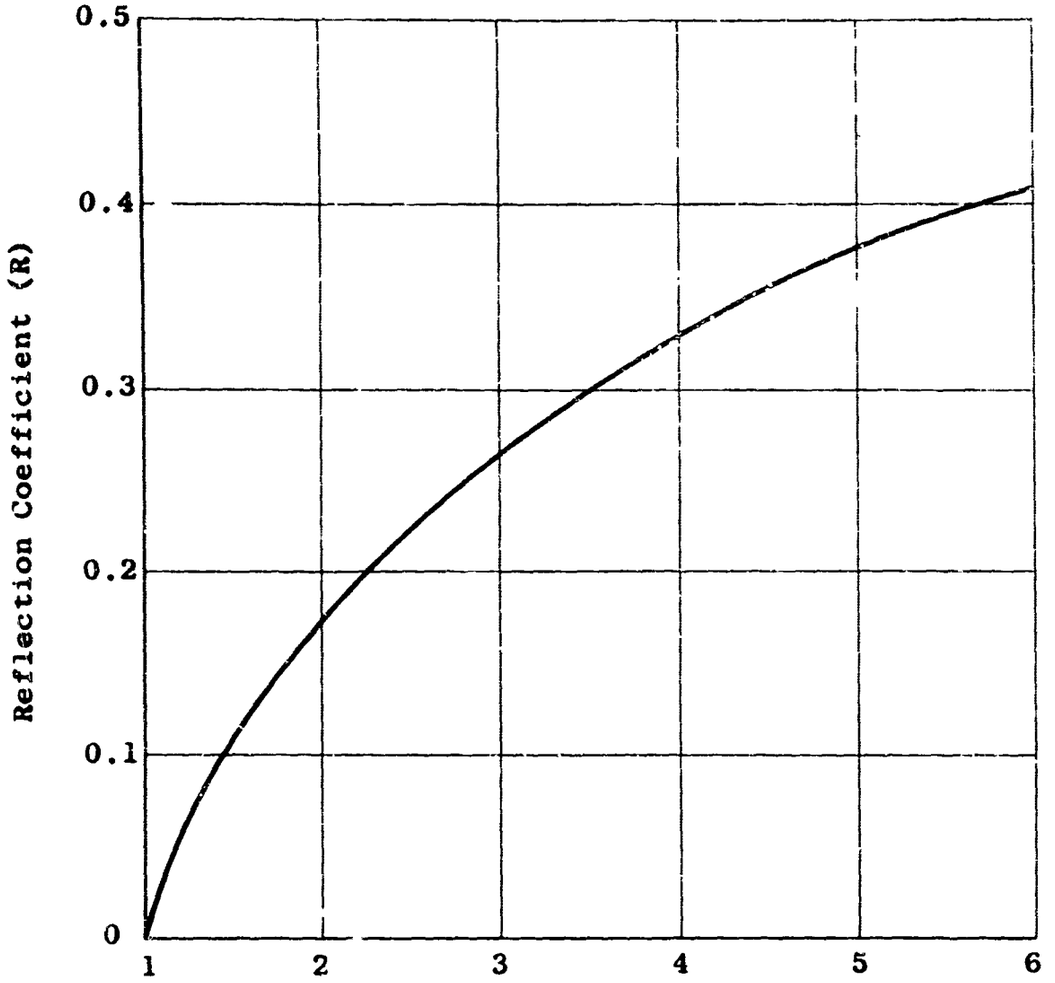

Reflection coefficient at normal incidence.

Fig. III-3

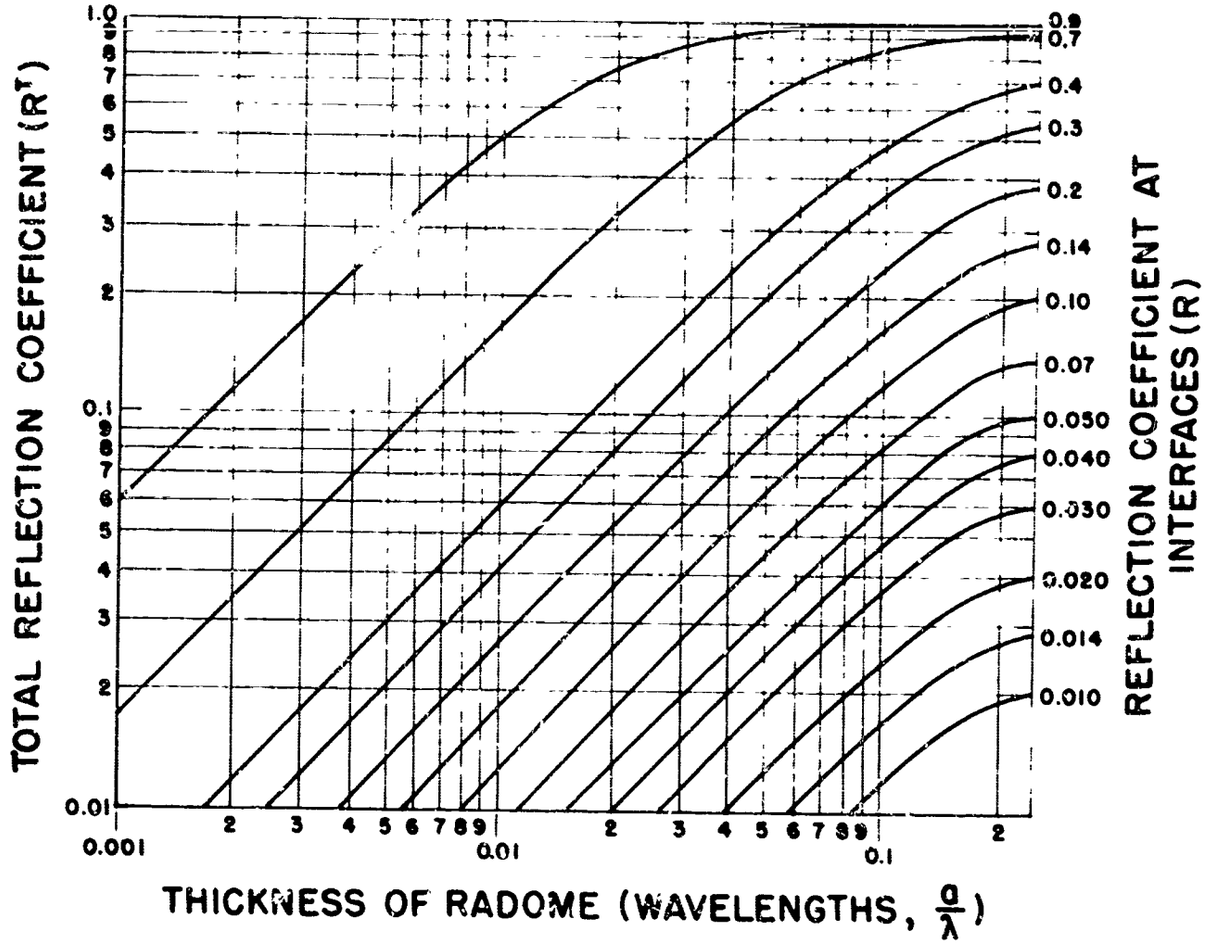

Reflection coefficient of radome wall at normal incidence vs. wall thickness for various interface reflection coefficients. Values neglect loss, i.e. $\tan \delta = 0$.

Fig. III-4

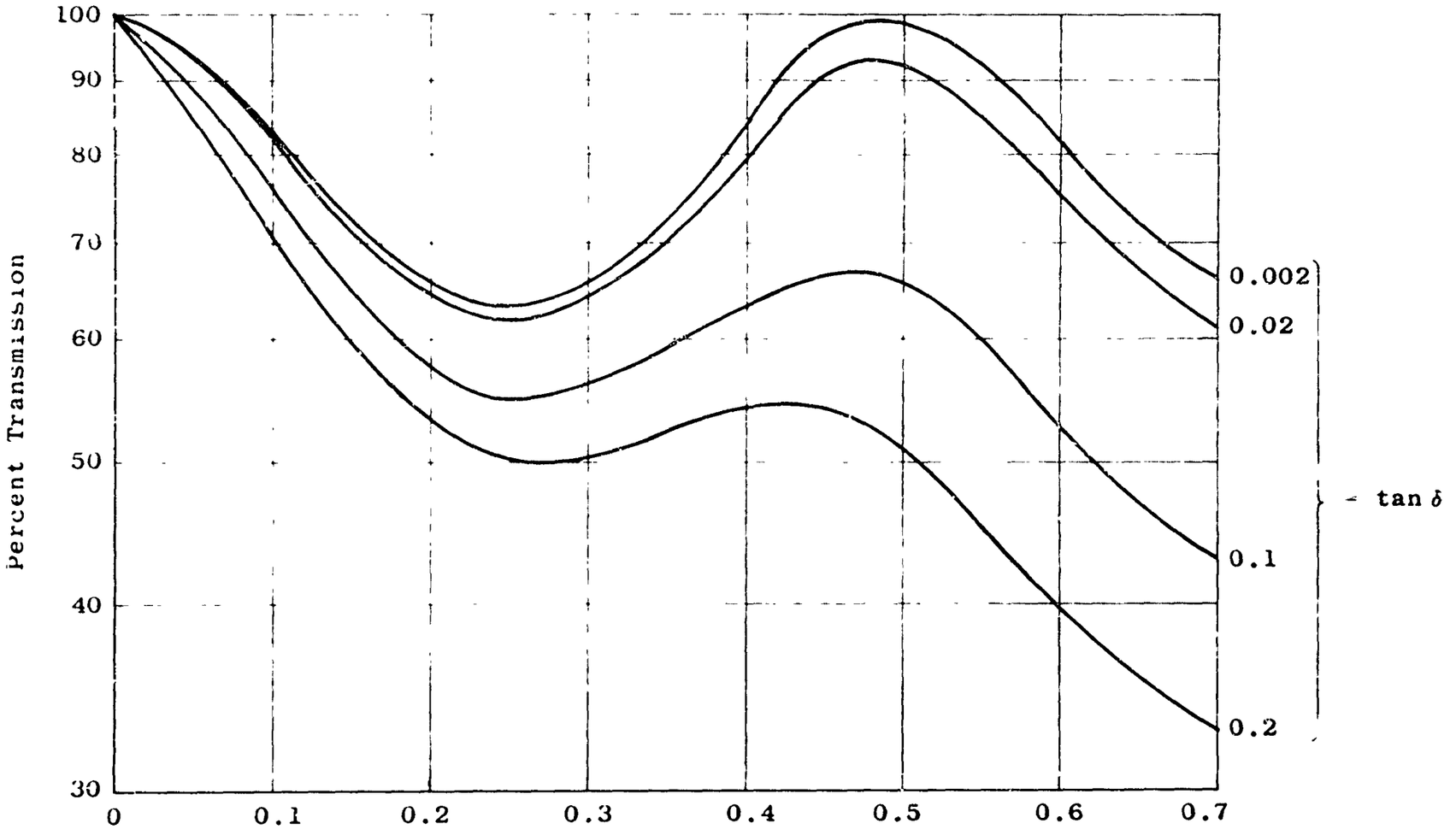

Thickness of Radome
(Wavelengths, $\frac{a}{\lambda}$)

tan δ (loss tangent) = $\frac{\epsilon''}{\epsilon'} = \frac{\sigma}{\omega\epsilon'}$; $\frac{\epsilon'}{\epsilon_o} = 4$

Percent transmission through radome wall
of various loss tangents at normal incidence.

Fig. III-5

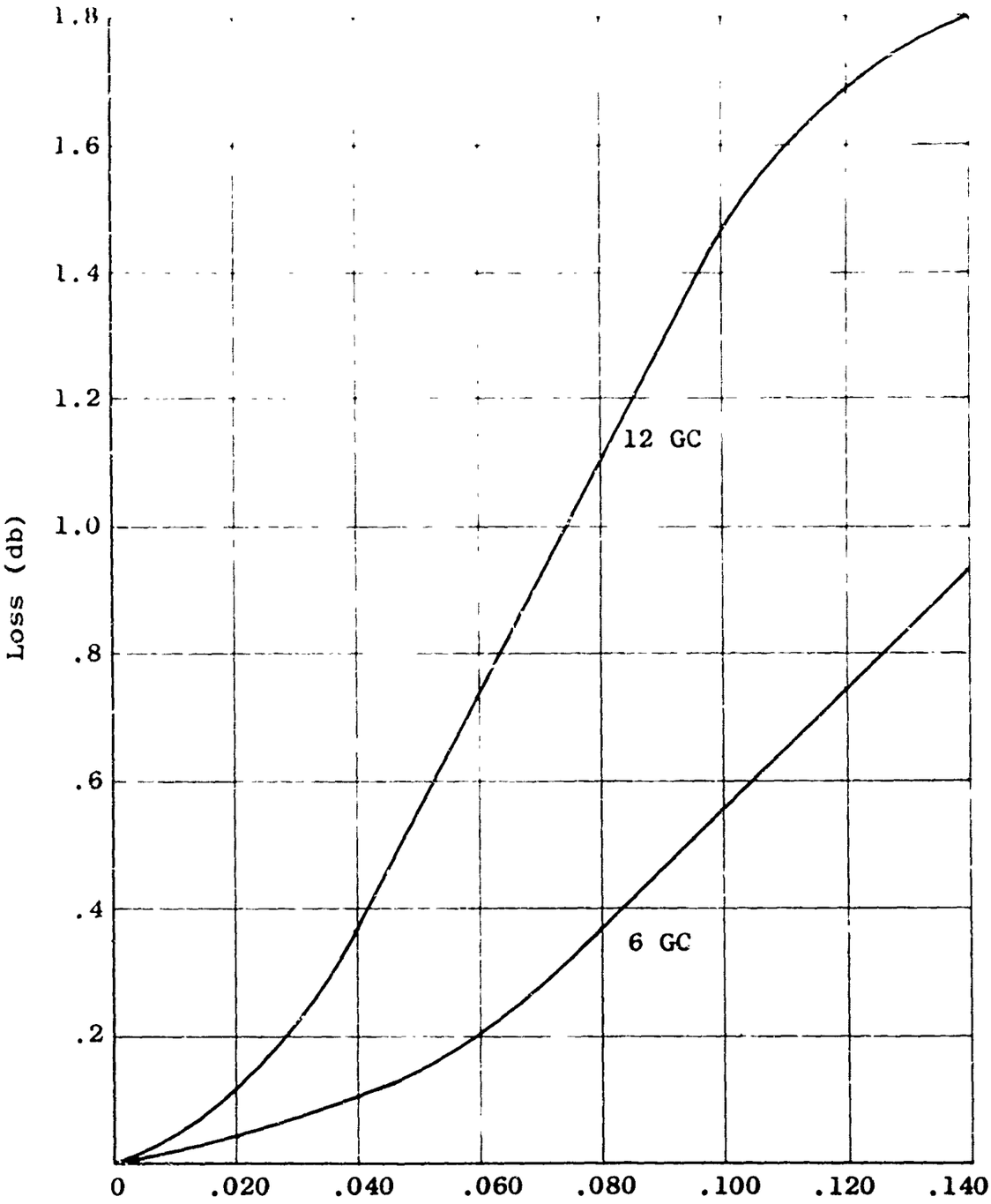

Loss of radome due to reflection.
(Assuming $\frac{\epsilon'}{\epsilon_o} = 3.5$ and $\tan \delta = 0$.
at 6 GC and 12 GC).

Fig. III-6

IV. ELECTRICAL TESTS

To help the radome designer do his job, it is necessary that he have at his disposal a method of measuring the complex dielectric constant of the radome material as well as a technique for evaluating its total performance such as degradation of gain and effect on antenna pattern.

Many techniques for the measurement of the complex dielectric constant of low loss materials are contained in the literature[4,5,6]. The one employed at Andrew Corporation is illustrated in Fig. IV-1. It consists of measuring one or more thicknesses of the radome material in the end of a shorted waveguide section. If sufficient care is used in the preparation and mounting of the sample, accuracies of the order of $\pm$ 1% can be obtained for dielectric constant values and accuracies of the order of $\pm$ 5% or $\pm$ .0005 (whichever is greater), can be obtained for loss tangent values.

To measure the effective loss in db a given radome imposes on an antenna, Andrew Corporation employs a direct measurement technique as illustrated in Fig. IV-2. Using this setup the source antenna and test antenna are aligned for maximum signal together with a monitor antenna as shown. Before the radome is placed in position on the test antenna the ratio meter and attenuator is set for a zero reading. The radome is then placed on the test antenna and the attenuation read directly in db on the ratio meter. This procedure is repeated a number of times to insure consistency of results.

In cases where the antenna and radome specifications impose severe requirements on the sidelobe and the wide angle radiation structure of the antenna pattern, the antenna pattern is measured with and without the radome in place. This measurement may be correlated with the loss measurement described in the preceding paragraph by integrating the gain from the patterns taken with and without the radome.

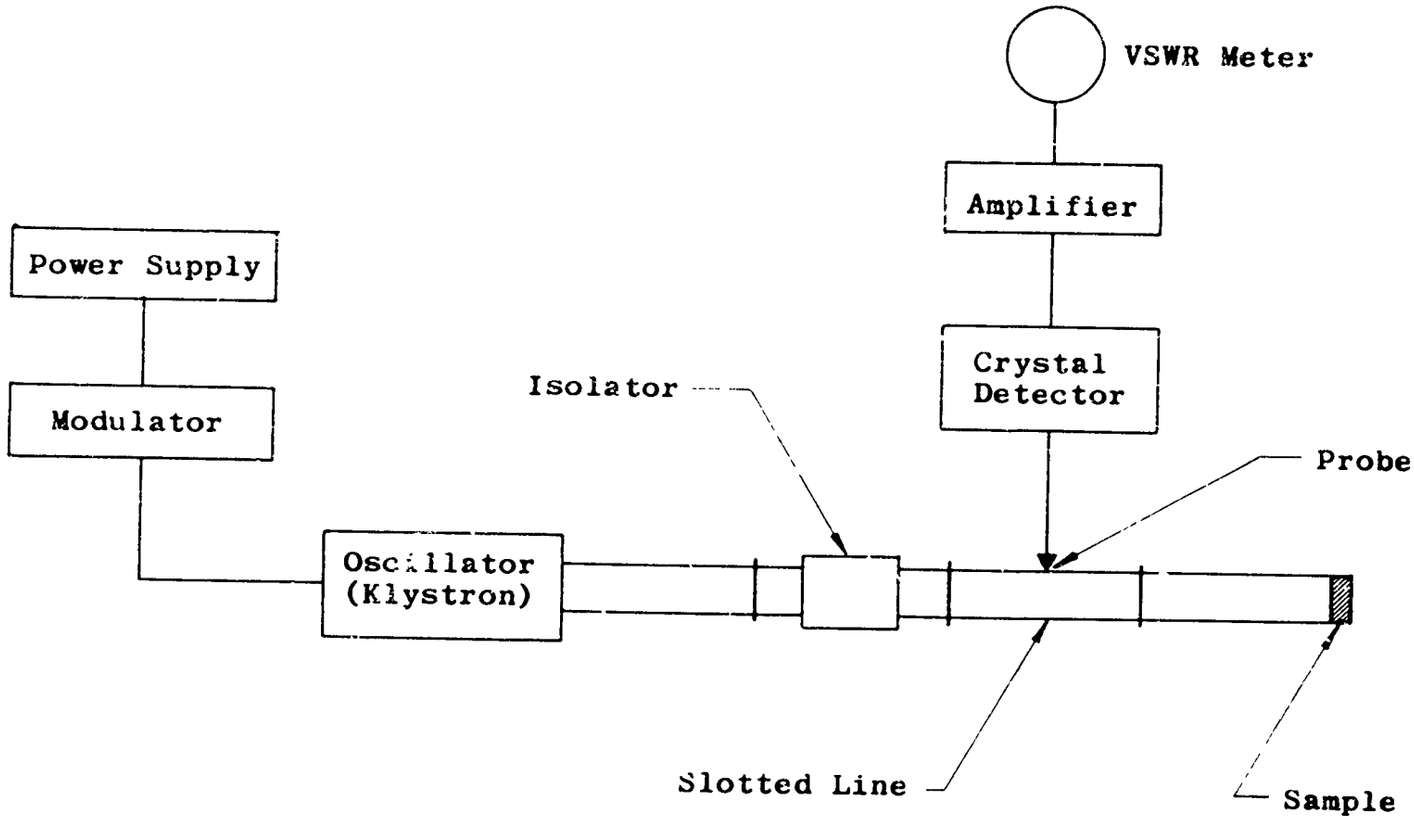

Complex Dielectric Constant
Measurement Test Setup

Fig. IV-1

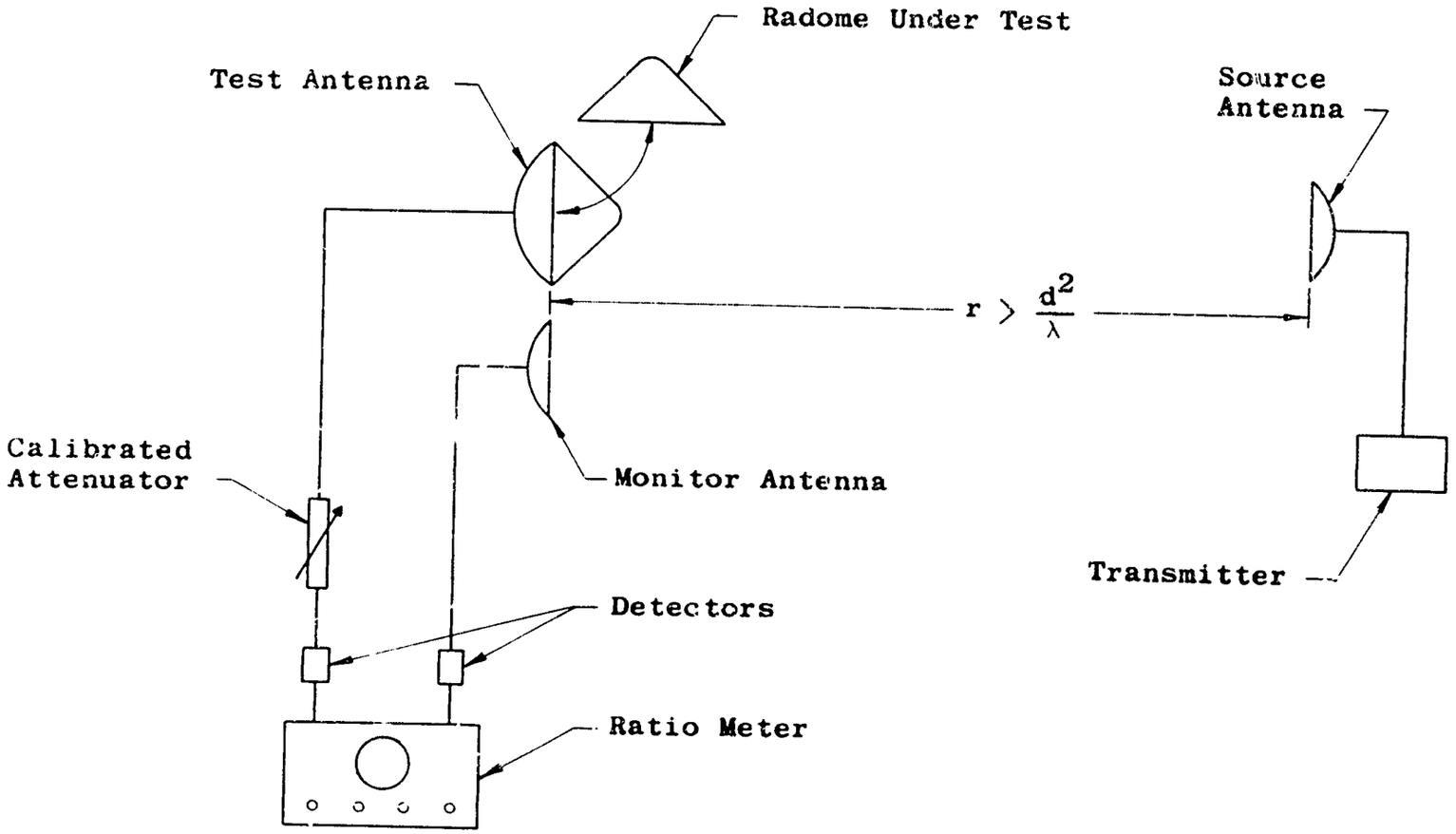

Electrical Test Setup to Determine Radome Loss

Fig. IV-2

V. MECHANICAL CHARACTERISTICS AND TESTS

The most realistic test of the mechanical performance of microwave radomes is their field performance. Unfortunately, nature is not very cooperative and a radome or group of radomes may not see the design environment for many years. Microwave sites are often remote and even when extreme environments occur they are usually not documented adequately to provide meaningful test data. The problem then is to simulate the design environments under controlled conditions. Field reports then serve as a check on the laboratory work and provide information relating to possible weak links and associated design improvements.

The effects of weathering, i.e., temperature cycles, sunlight, moisture, chemical action, etc., are fairly well known and documented. Ordinarily the material supplier has available detailed information regarding actual field tests and prescribed speeded-up environmental tests. The final radomes, as required, can be subjected to environmental tests to evaluate their adequacy. There are numerour tests for simulation environment conditions, including salt spray, heat cycles, humidity cycles, and rain tests. Specific details of these tests can vary but in essence they all aim for the same objective--introducing more severe laboratory conditions to simulate in a relatively short time the long time effects of nature.

Whenever a radome is made in any way differing from those in use for many years, the engineer must evaluate the effect of the change in weathering. The Engineering and Quality Control decisions relating to the extent of testing required to evaluate weathering depends on many factors, e.g., data available, quantity involved, and class of materials. Obviously not every such decision will be correct. Recently, Andrew replaced two laminated plastic radomes which were delaminating, after only two years of service. The difficulty is attributable to limitation in the manufacturing art, although the original design and construction followed recommended practice and should have resulted in a weatherproof product. It must also be recognized that certain locations are unique--a radome construction which has years of usage in many parts of the world may fail in weeks at a particular location due to atmospheric contamination unique to that location. If this were known originally it could be avoided, but such prior knowledge is rare.

Structurally radomes must withstand the forces caused by the wind. It is convenient to consider two aspects of this problem: wind forces and structural response. In certain instances the forces and response are coupled dynamically, but for the purposes of this paper it is adequate to consider them separately. Depending on the shape and orientation of an object placed in the wind (or in a wind tunnel) the pressure distribution over its surface can vary substantially. When interest is in the gross loads, e.g., in designing towers, these variations are not important and only the total force is significant. For the radome itself the nonuniformity of the load is of primary importance. General discussions of wind forces can be found in many sources including the ASCE report[7] and Hoerner[8]. Wind tunnel tests have been conducted with various shapes of interest. A typical example is the spherical segment with isobars shown on Fig. IV-1[9]. The complexity of the pressure distribution is obvious from this figure.

Determination of the response of a shell type structure to complex loading is a difficult problem either experimentally or theoretically. A theoretical approach which must be based on idealization regarding material and initial conditions, requires a complex numerical solution using a high speed digital computer. An experimental approach also is complex due to the load distribution required. The loading shown in Fig. V-1 was the basis for one such experimental study[10]. This particular example is mentioned here primarily to illustrate the complexity which can be involved. For other shapes, e.g., the flat radomes, the variations in pressure are much less violent and an assumption of uniform distribution is reasonable.

In evaluating the wind load resistance of various radomes, it is important that these complexities be kept in mind. For the flat membrane radome (see Fig. II-3) uniform loading is adequate. Load tests have been performed using dead weight, sand bags and subsequently sand, and more recently vacuum. The use of sand (or sand bags) introduces certain limitations since the arching of the sand causes nonuniform load and hence deceptive results. Applying a vacuum to the interior of the antenna produces a uniform load on the radome. The load deflection curve for one such vacuum test is shown on Fig. V-2.

For the rigid conical radome, as shown in Fig. II-1, the loading would be more complex. The shape reduces the gross loading, but introduces pressure variations over the surface.

As an approximation for the actual loading, it has been assumed that by taking no advantage of the load reductions, due to shape, would balance off against the use of symmetrical load. This assumption makes it possible to test this type of radome using internal vacuum. Fig. V-3 shows a 10 ft. radome under such vacuum load--it is interesting to note that even this gross buckling was not permanent. When the vacuum was released the radome returned to its initial position although there were cracks in the Fiberglas material along the break lines. Based on vacuum tests on Fiberglas, sprayed-up and hand layed-up, radomes, the following empirical formula has been developed to relate the pressure which can be resisted to the properties of the radome.

$$p = \frac{271E}{(r/a)^2}$$

where p = pressure (psf)
E = Young's Modulus (psi)
r = radius of antenna (in)
a = minimum thickness of radome (in)

It should be pointed out that this is an approximate formula and that the constant, i.e., 271 may vary by as much as 25%.

Snow and ice are of little consequence with regard to loading and are assumed to be covered within the specified pressure. k Falling ice is one exception. No quantitative data on falling ice is known to the writers. Some experiments involving dropping ice and simulated ice, i.e., aluminum and wood, have been conducted, but the results are at best qualitative. It is possible to compare radomes of different construction. It is also possible to observe the significance of "ice" shape on damage. It is obvious that "ice" from a sufficient height will damage all radomes. The system designer has a choice of accepting this risk or providing the ice screen to stop or break up the ice before it reaches the radome.

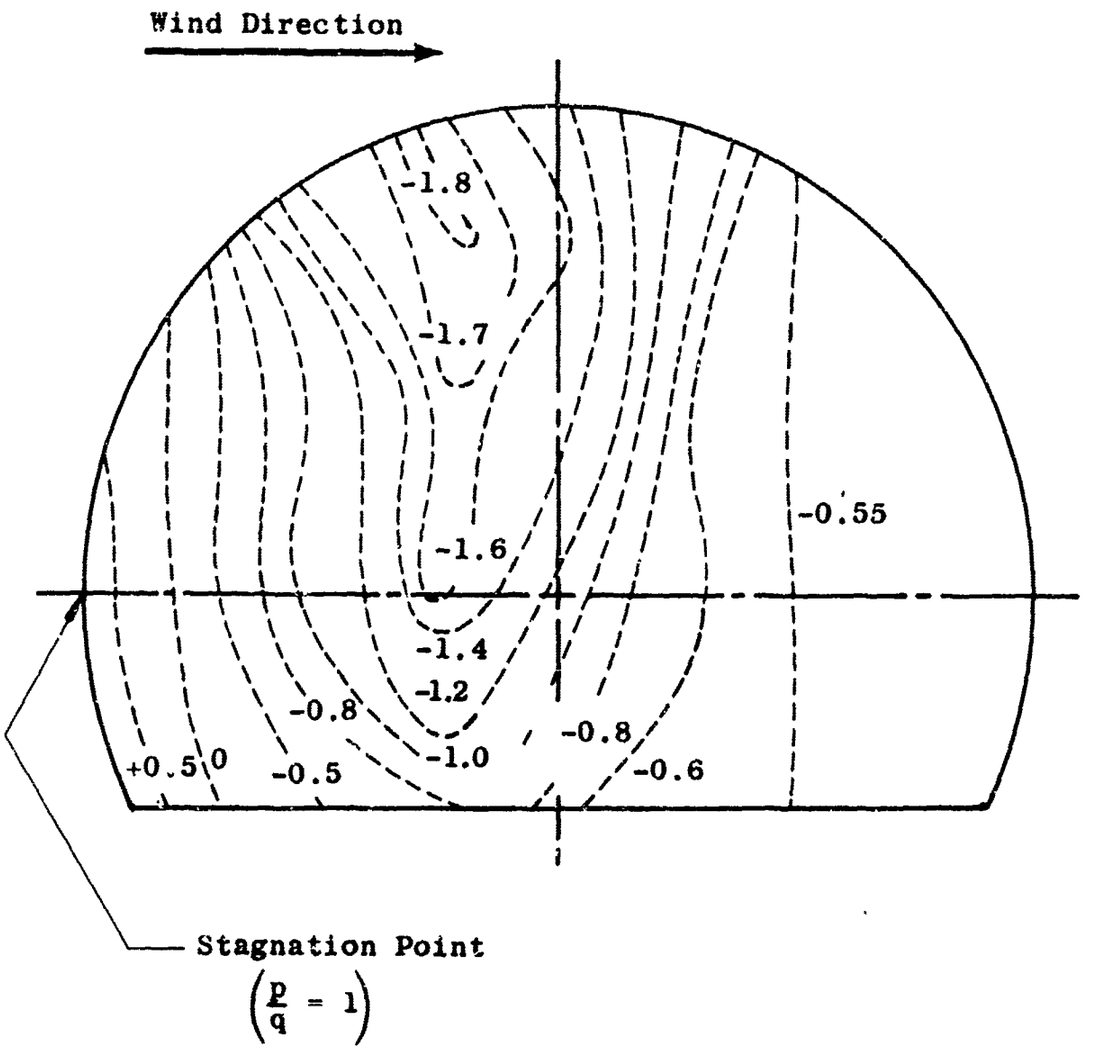

Experimentally Determined Isobars

Fig. V-1

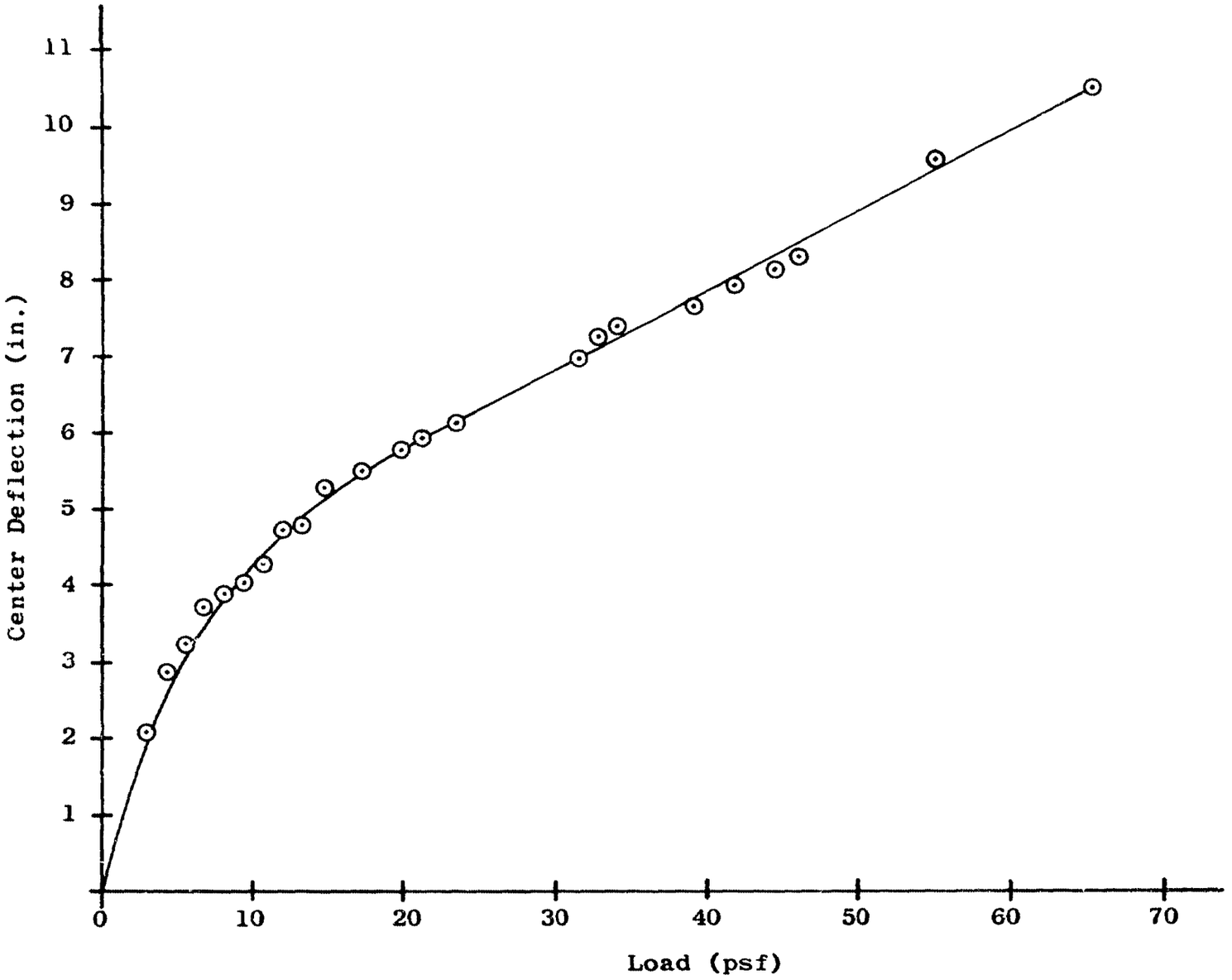

10 Ft. Diameter Hypalon Radome Subjected to Vacuum

Fig. V-2

Rigid 10 Ft. Radome Buckled Under Vacuum

Fig. V-3

VI. STATE OF THE ART

This paper has been considered in a relatively general fashion, radomes used in connection with microwave antennas. The current knowledge of these radomes is far from complete, but they do work with relative success. This is not an area in which any "break throughs" are to be expected, but rather improvements and modifications to the present approaches.

The classical solution has been Fiberglas radomes. This solution is limited by the relatively high losses which are particularly significant at higher frequencies. Structurally, the adequacy of rigid Fiberglas radomes is limited to perhaps 12 ft. diameter. It should be noted here that higher frequencies and/or higher performance antennas mitigate for thinner radomes which are structurally inadequate.

Undoubtedly, Fiberglas radomes will be with us for most standard applications. At least, at the present, they represent the most economical solution. It is obvious, however, that the new radome construction will be used in ever increasing numbers. For high performance, i.e., shrouded antenna, the membrane represents a relative inexpensive and electrically excellent radome. This technique has been used on antennas up to 12 ft. in diameter. Certain trade-offs are being considered, e.g., a tripod to support the membrane at the center to minimize the effect of deflection, thicker membranes to minimize deflection or longer shrouds to permit use of thinner membranes; reinforced membranes to minimize deflections; introductions of internal pressure to reduce deflection.

Where a shroud is required for electrical reasons the above class of solutions is clearly optimum in terms of both electrical performance and cost. For other applications, the semi-rigid approach appears to be the most advantageous. To date this approach has seen only limited use and yet it is suitable for high frequency, low loss application, and large diameters. There are problems relating to aperture blockage, surface inclination, and other factors, but these are at most details.

Other methods of radome construction have advocates and undoubtedly have certain advantages. Some of these have been mentioned such as sandwich type walls and thick foam of low density but so far they have not been made economically feasible. Inflated radomes, although economically feasible, still present certain problems in field usage.

The accompanying table summarizes the attributes of several radome types for comparison purposes. It is, perhaps, over-generalized and the data presented are intended to be typical rather than specific.

COMPARISON TABLE FOR PARABOLOID ANTENNA RADOMES

Radome Type	Material	Dielectric Constant	Loss Factor	Relative Cost	Reliability	Other Factors
Rigid (Single Wall)	Fiberglas	3-5	Fair	Low	Good	Mechanical Rigidity May Be a Problem For Antennas Larger Than 10' Diameter
Membrane Type (Flat)	Hypalon* Coated Nylon	3-4	Excellent	Low But Needs Shield for Support	History to Date is Good	
Membrane Type with Support Structure	Hypalon* Coated Nylon	3-4	Good	Medium	History to Date is Good	
Foam Type	Foamed Plastic	1.1 - 2	Excellent	Low to Medium	Depends on Foam Structure	Excessive Handling May Damage Structure
Inflatable	Hypalon* or Other Suitable Membrane	3-4	Excellent	High (Including Pressure Equipment)	Good, but Dependent on Environment and Inflating Mechanism	

* Trade name for Chlorosulphonated-Polyethylene

BIBLIOGRAPHY

1. Silver, Samuel, "Microwave Antenna Theory and Design," Radiation Laboratory Series, McGraw Hill Book Company, Inc., 1949, pp. 528-542.

2. Jasik, Henry, "Antenna Engineering Handbook," McGraw Hill Book Company, Inc., 1961, pp. 32-1 to 32-40.

3. Ramo, Simon and Whinnery, John R., "Fields and Waves in Modern Radio," John Wiley and Sons, Inc., New York, London, 1962, p. 291.

4. Roberts, S. and von Hippel, A., "A New Method for Measuring Dielectric Constants and Loss in the Range of Centimeter Waves," General and Applied Physics, Vol. 17, No. 7, pp. 610-616, July, 1946.

5. von Hippel, Arthur R., "Dielectric Material and Applications," John Wiley and Sons, Inc., New York, 1954.

6. Montgomery, C. G., "Techniques of Microwave Measurements," Radiation Laboratory Series, McGraw Hill Book Company, Inc., 1947.

7. "Wind Forces on Structures," ASCE Transaction, Vol. 126, Part II, Paper 3269, 1961.

8. Hoerner, S. F., Fluid-Dynamic Drag, Published by the Author, Midland Park, N. J., 1958.

9. Cornell Aeronautical Laboratory, Inc., "Wind Tunnel Tests of a 1/24 Scale Model Radome & Tower," Report No. VB-909-D-1, Air Force Cont. No. AF 30(602)-976, Sept. 1954.

10. Sevin, E. and MacDonald, V. L., "Model Studies of 3/4 Spherical Radome Shell Under Wind Loading," Symposium on Space Mechanics, Armour Research Foundation, Dec. 1962.

THE USE OF TRAVELING-WAVE STRUCTURES IN INTEGRATED ANTENNA-RADOME DESIGN

John R. Baechle
Antenna Laboratory
Department of Electrical Engineering
The Ohio State University
Columbus, Ohio, 43210

Acknowledgments

The suggestions of Dr. J.H. Richmond are greatly appreciated.

The research reported in this paper was supported in part by Contract AF 33(615)-1081 between The Ohio State University Research Foundation and the Research and Technology Division, Air Force Systems Command, United States Air Force, Wright-Patterson Air Force Base, Ohio 45433.

Introduction

The exigency of integrating the design of the antenna-radome system for aerospace vehicles became apparent when the possible benefits to be derived were recognized. It was realized several years ago that systems which were better electrically, mechanically, and aerodynamically and which made more efficient use of available space might be obtained through this approach.[1]

As the speed and performance of modern aircraft and missiles has increased a need has developed for more sophisticated electronic control. With this need comes the requirement for more efficient use of the total volume of the vehicle so that the necessary additional electronic stores can be accommodated.

The most common geometry for the antenna-radome combination is the dielectric nose cone covering a parabolic reflector antenna. There is a considerable volume between the reflector and the radome which might be used for electronic stores if the antenna could be moved closer to the radome.

One antenna structure which can be visualized as being located quite near to the radome is the traveling-wave structure. This concept is pictured in Fig. 1. To do this the antenna geometry should be made to

conform as nearly as possible to the radome shape which is in turn determined by aerodynamic and thermal requirements. In any event the antenna will probably be curved in at least one direction and it is important to know how this curvature affects the electric and magnetic fields immediately above the antenna surface since this will determine the manner in which the energy is coupled to the radome and therefore the characteristics of the combined antenna-radome radiating system.[2]

The traveling wave structure could also be integrated into a single unit on the surface of the vehicle. This concept is also pictured in Fig. 1. Again the antenna would likely have one or more degrees of curvature to satisfy the aerodynamic needs of the design. The manner in which curvature affects the radiating properties of the integrated structure are then of interest.

The fact that a traveling-wave structure might present solutions to other radome problems such as structural attachment, mechanical strength, and the need to manufacture large continuous dielectric structures in addition to space saving potential make the use of such structures more appealing in applications where they may have to be placed on curved surfaces.

With these facts in mind the effects of curvature on traveling-wave structures are investigated. The investigation is carried out by studying the effects of curvature in the direction of propagation on the wave number of an electromagnetic field propagating over a cylindrical traveling-wave surface. Calculated and experimental data are presented which show the effects of curvature on the wave number and on the electric and magnetic field intensity variations as a function of distance normal to the curved surface. Data are shown graphically for two specific antenna structures, the dielectric clad metal cylinder and the corrugated metal cylinder. Because of the simplicity of the expressions used, other types of structures may easily be studied either analytically or experimentally and calculations carried out with a minimum of effort on a desk calculator.

Analysis

To simplify the analysis that follows, it is assumed that conductor and dielectric losses are negligible. For purposes of design, a lossless traveling-wave structure is sufficiently characterized by either one or two parameters: either the guide wavelength or the leakage attenuation and the guide-wavelength. In the case of slow-wave structures in the absence of surface modulation or curvature, the wavelength along the structure is sufficient design information. In the case of leaky-wave structures both parameters must be specified.

The analysis is carried out using the coordinate transformation shown in Fig. 2. This transformation starts with the cylindrical coordinate system (r, ϕ, z') and sets $\chi = r - R$ and $y' = z'$ and $s = -R\phi$ where R is the radius of curvature of the surface being investigated. The analysis of an arbitrary field is made in terms of a superposition of the solutions for a TE and a TM field. The y' component is thus of prime interest. By using the transformation of Fig. 2 in the Helmholtz equations expressed in cylindrical coordinates and assuming no propagation in the y' direction the wave equation for the y' component of a vector field in the (χ, y', s) system is found to be

$$(1) \quad (R+\chi)^2 \frac{\partial^2 \overset{e}{\underset{m}{F}}_{y'}}{\partial \chi^2} + (R+\chi) \frac{\partial \overset{e}{\underset{m}{F}}_{y'}}{\partial \chi} + (R+\chi)^2 k^2 \overset{e}{\underset{m}{F}}_{y'} + \frac{\partial^2 \overset{e}{\underset{m}{F}}_{y'}}{\partial s} = 0;$$

$$k^2 = \omega^2 \mu \epsilon .$$

Here $\overset{e}{\underset{m}{F}}_{y'}$ represents the y' directed component of the electric field in the TE or m case or the magnetic field in the TM or e case. The quantity $\kappa = 1/R$ is the curvature of the surface and since the s-coordinate corresponds to the z-coordinate when the curvature becomes zero a separable solution of the form

$$(2) \quad \overset{e}{\underset{m}{F}}_{y'}(\chi, s) = \overset{e}{\underset{m}{F}}(\chi)\, e^{-j\overset{e}{\underset{m}{\gamma}} s}$$

is sought. Substitution of Eq. (2) into Eq. (1) and some algebraic manipulation gives

$$(3) \quad \frac{d^2 \overset{e}{\underset{m}{F}}}{d\chi^2} + \frac{\kappa}{1+\kappa\chi} \frac{d\overset{e}{\underset{m}{F}}}{d\chi} - \frac{(\overset{e}{\underset{m}{\gamma}}^2)\overset{e}{\underset{m}{F}}}{(1+\kappa\chi)^2} + k^2 \overset{e}{\underset{m}{F}} = 0.$$

The total derivatives arise because of the assumption that F is independent of the other variables: $F = F(\chi)$.

A solution of Eq. (3) in powers of κ would be of the form

$$(4) \quad \overset{e}{\underset{m}{F}}(\chi) = A[\overset{e}{\underset{m}{F_0}}(\chi) + \overset{e}{\underset{m}{F_1}}(\chi)\kappa + \overset{e}{\underset{m}{F_2}}(\chi)\kappa^2 + \ldots]$$

$$(5) \quad (\overset{e}{\underset{m}{\gamma}})^2 = (\overset{e}{\underset{m}{k}})^2 [1 + \overset{e}{\underset{m}{a_1}} \kappa + \overset{e}{\underset{m}{a_2}} \kappa^2 + \ldots]$$

for the field intensity and wave number respectively. The quantity $k'^{e,m}$ is the wave number normal to the surface for the limiting case of $\kappa = 0$.

On substituting Eqs. (4) and (5) into Eq. (3) and equating powers of κ after recalling that F_o is the solution for the plane structure the following relation is found for

$$(6) \quad F_1^{e,m}(\chi) = -\frac{k^2 + (\ell^{e,m})^2}{2\ell^{e,m}} \cdot \chi^2 e^{\ell^{e,m}\chi} + \frac{k'^{e,m} a_1^{e,m} \ell^{e,m} + k^2}{2(\ell^{e,m})^2} \cdot \chi e^{\ell^{e,m}\chi} .$$

The quantity $\ell^{e,m} = -jk_x^{e,m}$ is the wave number in the x direction for limiting case $\kappa = 0$, i.e., the plane structure.

Equation (6) has one undetermined constant, $a_1^{e,m}$. An equation for determining this constant is obtained by noting the requirement of the continuity of the tangential components of the electric and magnetic field intensities at a surface. From this, the requirement that the impedance in a direction normal to the surface be continuous, is obtained. The constant $a_1^{e,m}$ is determined from the impedance boundary condition. In order to apply this boundary condition, two separate cases, that of TM excitation and that of TE excitation, must be considered.

Using Maxwell's equations with the curl expressed in the proper form for the coordinate system of Fig. 2 the s-component of the field may be written in terms of the derivative with respect to χ of the y' component. The requirement of continuity of the impedance in a direction normal to the surface then leads to

$$(7) \quad \frac{dF^m}{d\chi} = j\omega\mu \frac{F^m}{Z^m}$$

for TE excitation and

$$(8) \quad \frac{dF^e}{d\chi} = j\omega\epsilon Z^e F^e$$

for TM excitation. Now $Z^{e,m}$, the surface impedance of the radiating structure, may depend on curvature, κ', and is therefore written

$$(9) \quad Z^{e,m} = Z_s^{e,m} [1 + Z_1^{e,m} \kappa + Z_2^{e,m} \kappa^2 + \cdots]$$

where $Z_s^{e,m}$ is the surface impedance for the plane structure.

If Eqs. (4) and (9) are substituted into Eqs. (7) and (8) and, after collecting coefficients of κ, use is made of Eq. (6), then some algebraic manipulation will give for the important special case of a surface-wave structure

$$(10) \qquad a_1^m = \frac{1 - 2\left(\frac{\eta_c}{X_s^m}\right)^3 k Z_1^m}{k\left(\frac{\eta_c}{X_s^m}\right)\left[1 + \left(\frac{\eta_c}{X_s^m}\right)^2\right]}$$

and

$$(11) \qquad a_1^e = \frac{1 + 2\left(\frac{X_s^e}{\eta_c}\right)^3 k Z_1^e}{k\left(\frac{X_s^e}{\eta_c}\right)\left[1 + \left(\frac{X_s^e}{\eta_c}\right)^2\right]}$$

Here η_c is the characteristic impedance of the ambient medium in which the propagation velocity is v and $k = \omega/v$. The quantity $X_s^{e,m}$ is the surface reactance of the plane structure.

An expression for $Z_1^{e,m}$ may often be obtained from an expression for the surface impedance in cylindrical coordinates.[3] For large radii of curvature Z_1^e for the corrugated metal cylinder is

$$(12) \qquad Z_1^e \simeq -\frac{1}{2} \quad \text{(depth of corrugation)}$$

and for the dielectric clad metal cylinder

$$(13) \qquad Z_1^e \simeq 0.$$

Good agreement with the boundary value solution and with experiment is obtained even for relatively small radii of curvature by using the first two terms in the series of Eq. (5) and by approximating the square root by the first two terms in its binomial expansion:

$$(14) \qquad \gamma_m^e \simeq k_m'^e \left[1 + \frac{a_{1m}^{re}\,\kappa}{2}\right].$$

Results

The results of substituting Eq. (11) into Eq. (14) and using Eqs. (12) and (13) are compared with the boundary value solutions and experiment in Figs. 3 and 4 respectively.

An interesting consequence of this analysis is that if the impedance function Z^{fn} is intrinsically real, as in the case of surface wave structures, then the curvature does not produce attenuation in the form of Eq. (5). An expression for the attenuation may be obtained by another approach such as a determination of the change in total transverse impedance as a function of wave number.[3] This indicates that radiation is a second order effect of curvature. Figure 5 shows calculations of the radiation attenuation due to curvature of a corrugated surface.

The effects of curvature on the electric and magnetic field intensity variation as a function of distance normal to the curved surfaces can be calculated using the first two terms of the series of Eq. (4) and good agreement is obtained with experimental data as can be seen in Fig. 6.

Conclusions

This analysis, which utilizes prior knowledge of the properties of the plane version of a curved structure, has yielded simplified expressions through which other types of structures may easily be studied either analytically or experimentally and calculations may be carried out with a minimum of effort on a desk calculator.

In many cases of interest k' is already well known. For those cases where k' is known but an analytic expression for a_1^{fn} cannot be obtained, a single measurement will determine a_1^{fn} through Eq. (14). The quantity k' may also be determined experimentally. Thus this method of analysis may easily be applied to many structures without the necessity of a tedious analytical solution.

References

1. Behrens, F.H., "Unified Antenna-Radome Development", Proceedings of the OSU-WADC Radome Symposium, WADC Technical Report 56-393, Vol. II, August 1956, ASTIA Document No. AD 97151.

2. Richmond, J.H., "A Reaction Theorem and Its Application to Antenna Impedance Calculations", IRE Trans., Vol. AP-9, No. 6, Nov. 1961.

3. Baechle, J.R., "A Study of Some Effects Associated with the Role of Traveling-Wave Structures in Integrated Antenna-Radome Design", Report 1751-3, Antenna Laboratory, Department of Electrical Engineering, The Ohio State University Research Foundation, Columbus 10, Ohio, 22 November 1963, DDC Number AD 427 133.

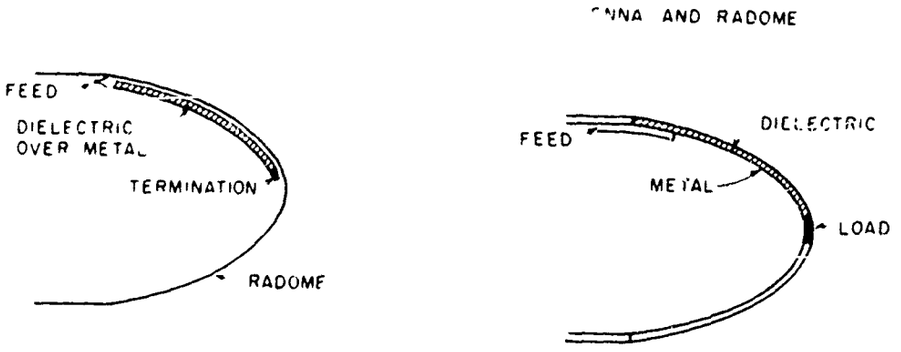

(a) Antenna and radome (b) Flush mounted antenna

Fig. 1. Integrated design concept.

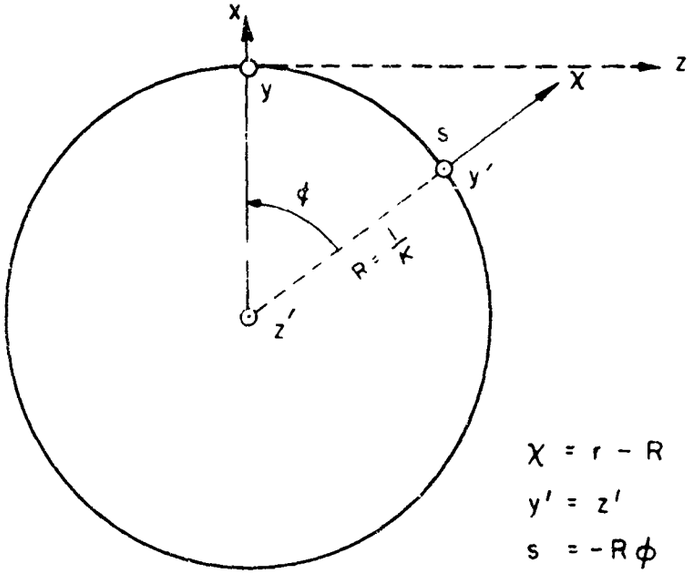

Fig. 2. Coordinate transformation.

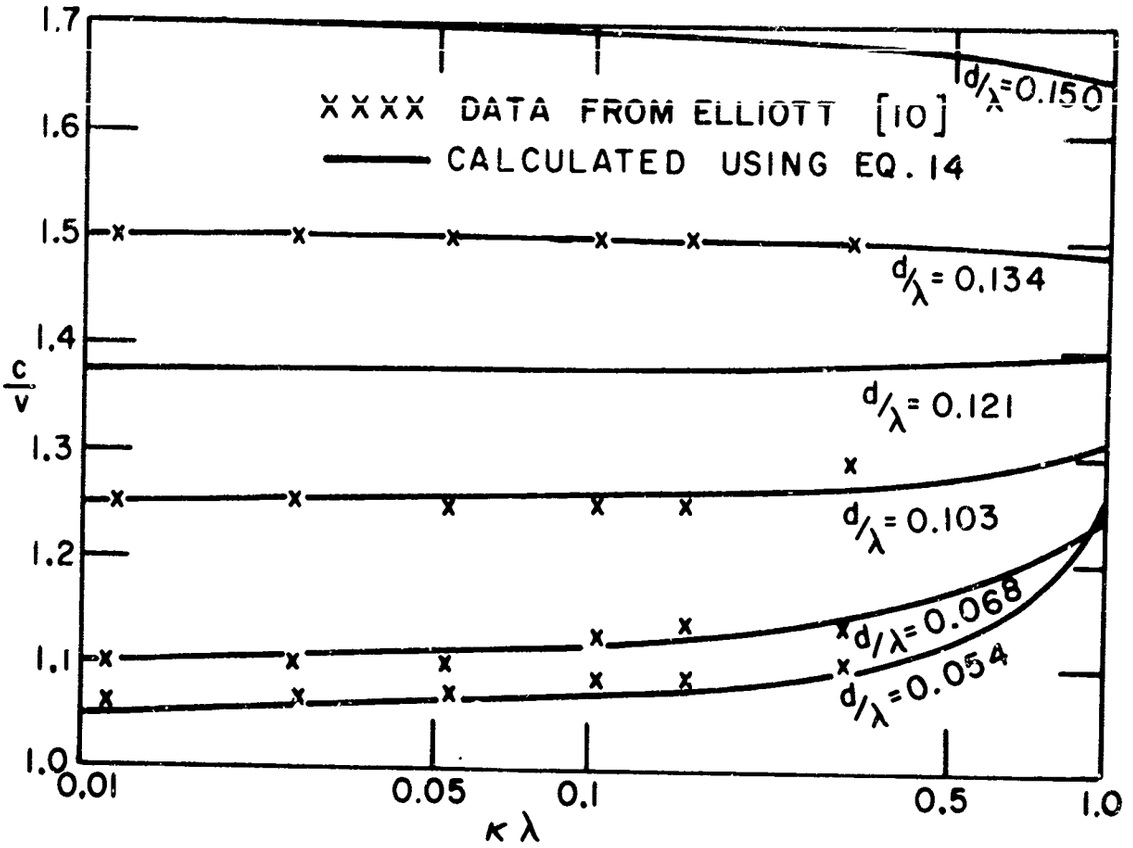

(a) Corrugated surface with depth of corrugations, d

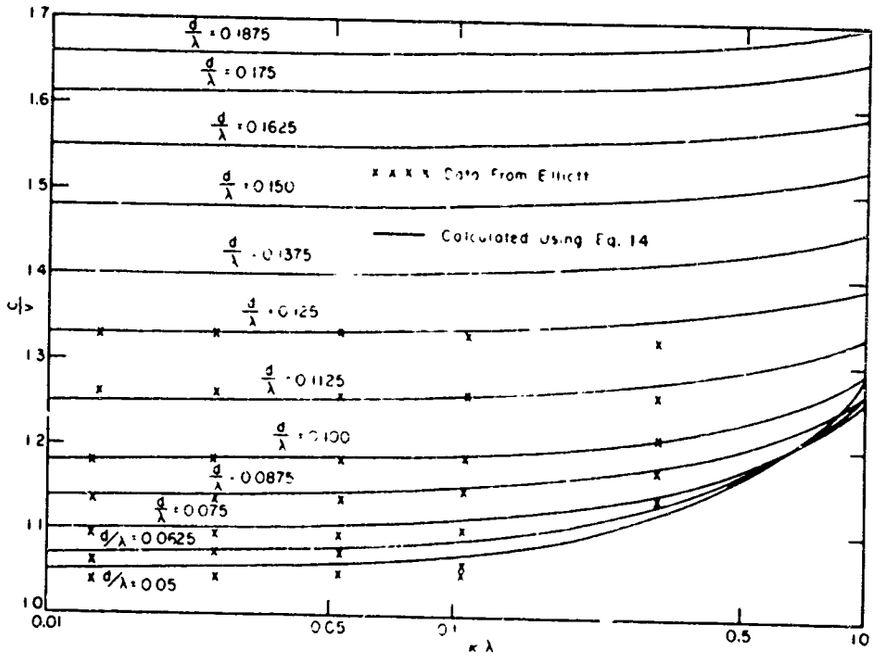

(b) Dielectric surface with $\epsilon_r = 4$ and thickness, d

Fig. 3. Comparison of calculated phase velocities.

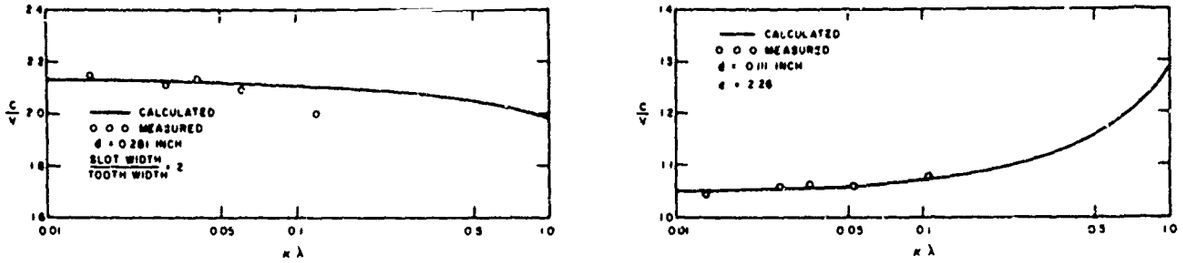

(a) CORRUGATED METAL SURFACE MEASURED AT 8.2 Gc

(b) POLYETHYLENE-COATED METAL SURFACE MEASURED AT 9.37 Gc

Fig. 4. Comparison of calculated and measured phase velocities.

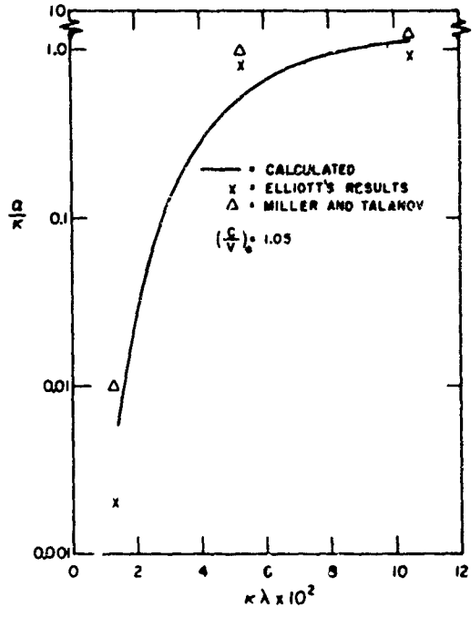

Fig. 5. Comparison of calculated values of the radiation attenuation.

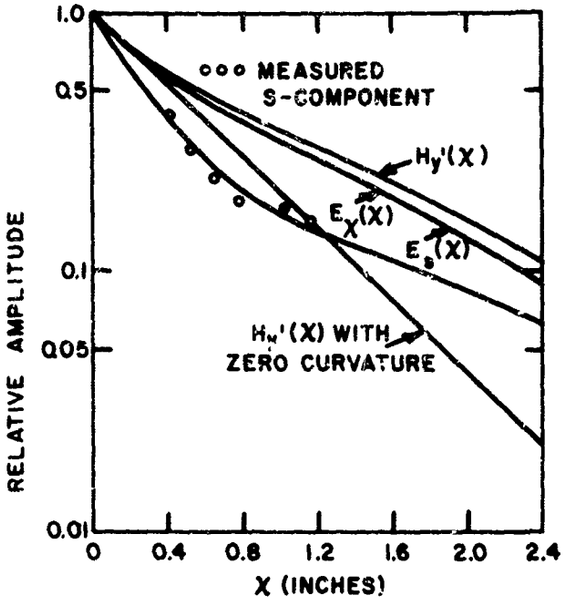

Fig. 6. Comparison of calculated and measured field variation normal to polyethylene with $\kappa\lambda = 0.105$.

ERROR AND LIMITATION ANALYSIS ON THE MEASUREMENT OF DIELECTRIC PROPERTIES BY USE OF THE SHORTED WAVEGUIDE REFLECTION THEORY AT HIGH TEMPERATURES

by Russell W. Johnston
Electromagnetic Radiation Laboratory
Douglas Aircraft Company, Inc.
Santa Monica, California

The development of microwave radomes and similar structures wherein the low loss transmission of electromagnetic energy is desired requires the determination of the dielectric constant and loss tangent as basic information. It is the intent here to examine the various major sources of errors and limitations of the shorted waveguide method which has been used over the past decade for this determination. Although the existence of other methods such as that of cavity resonance[1] or pure reflection[2] is acknowledged, the desire here is to restrict discussion to the shorted guide approach.

I. THEORY OF MEASUREMENT

The method itself is based on the phenomena that if measurements are made on the standing wave pattern within a shorted waveguide, the pattern will shift position and broaden at the null with the insertion of a sample material against the short. (Figures 1 and 2.) The rigorous mathematical theory is contained in several sources and will not be dealt with here except for the presentation of working equations.[3, 4, 5, 6]

Determination of γ for all materials high and low loss, may be done with equation (4). However, for low loss materials (tan δ less than .1) equation (4) may be simplified to equation (4A). Equation (4A) results by equating the real parts of equation (4) for the low loss case.[7]

The magnitude of error introduced by the use of equation (4), however, is about ±1 per cent, but then the evaluation of the cumbersome transcendental, tanh x/x, is eliminated.[8]

The necessary relations are as follows:

$$K = \frac{\left(\frac{1}{\lambda_c}\right)^2 - \left(\frac{\gamma}{2\pi}\right)^2}{\left(\frac{1}{\lambda_c}\right)^2 + \left(\frac{1}{\lambda_g}\right)^2}$$

EQUATION 1

$$\tan \delta = \frac{\Delta X}{d^*} \left\{ \frac{\frac{\lambda_g}{\lambda_c} + 1 - \left(\frac{\lambda_g}{\lambda_c}\right)^2 \frac{1}{K}}{\left(\frac{\lambda_g}{\lambda_c}\right)^2 - 1} \right\} \left\{ \frac{\gamma d^* + \gamma d^* \tan^2 \frac{2\pi X_o}{\lambda_g}}{\gamma d^* + \gamma d^* \tan^2 \gamma d^* - \tan \gamma d^*} \right\}$$

EQUATION 2

$$\frac{X_o}{\lambda_g} = \frac{N}{2} - \frac{d^*}{\lambda_g} - \frac{(X_2 - X_1)}{\lambda_g} \quad \text{Where } N = 1, 2, 3 \cdots \text{ so that } o < \frac{X_o}{\lambda_g} < .5$$

EQUATION 3

$$\frac{\tanh \gamma d^*}{\gamma d^*} = \left\{ \frac{\frac{E_{min.}}{E_{max.}} - j \tan \frac{2\pi X_o}{\lambda_g}}{1 - j \frac{E_{min.}}{E_{max.}} \tan \frac{2\pi X_o}{\lambda_g}} \right\} \frac{\lambda_g}{j 2\pi d^*} \qquad \text{EQUATION 4}$$

$$- \frac{\lambda_g}{2\pi d^*} \tan \frac{2\pi X_o}{\lambda_g} = \frac{\tan \gamma d^*}{\gamma d^*} \qquad \text{EQUATION 4A}$$

$$\frac{E_{max.}}{E_{min.}} = VSWR = \frac{\lambda_g}{\pi \Delta x_n} \qquad \text{EQUATION 5}$$

where: (and with reference to Figures 1 and 2)

$(X_2 - X_1)$ = shift in position of null of VSWR pattern due to insertion of sample material into guide

$\Delta X = \Delta X_2 - \Delta X$ = broadening of null at double power or 3 db points due to insertion of sample material in guide

d^* = sample dimension parallel to guide axis corrected for temperature at which measurements are taken

a^* = width of guide perpendicular to guide axis corrected for temperature at which measurements are taken

λ_g = guide wavelength $\qquad$ λ_c = cut off wavelength

λ = free space wavelength

X_o = distance from sample surface to first null of standing wave pattern (see Figure 2)

γ = propagation constant within sample under test

K = dielectric constant $\qquad$ $\tan \delta$ = loss tangent

A method for determining the value of the VSWR is provided by equation (5) where ΔX_n is measured with a slotted section as the distance between the double power or 3 db points of the standing wave pattern.[9] The ΔX method is used when measuring VSWR values above approximately 10 as conventional means become inaccurate. This is easily seen when one considers that in order to determine a voltage minimum accurately at a VSWR greater than 10, probe coupling must be increased. Increasing probe depth, however, can effect a deformation of the VSWR pattern and in addition cause a change in detector characteristics due to a change in RF level.

Concerning radome development within the microwave range, frequencies between C and K band with high temperatures approaching 1650°C will be the primary ranges of interest that are to be considered here. A typical simplified measurement arrangement is illustrated in Figure 3 and the following analysis will be based on this system.

II. TECHNICAL DISCUSSION

A. VSWR

The best mechanical readout systems that can be adapted to a slotted line, such as the Gaertner M342, have a readout capability of $\pm 10^{-4}$ cm. The following analysis will serve to illustrate that, with the above condition, a VSWR in excess of 200 at the slotted section is necessary in order that any reasonable degree of accuracy be associated with the loss tangent measurement of low loss materials.

Consider that an empty waveguide system has a VSWR of 200. The return loss due to the guide only will be: (assuming the line is terminated with a perfect short)

$$\text{db return loss} = 20 \log \frac{\text{SWR}+1}{\text{SWR}-1} = 20 \log \frac{201}{199} = .0864\text{db}$$

Further consider that a sample whose dielectric constant and loss tangent are to be determined when inserted into the guide as in Figure 2 causes an additional .01 db return loss. (From Figure 5, a typical low loss sample approximately .4 cm thick at a wavelength of 3 cm and with a dielectric constant of about 3.0 will yield a loss tangent of .0008.)

$$.01 \text{ db} + .0864\text{db} = .0964\text{db} = 20 \log \frac{SWR+1}{SWR-1} \text{ or } SWR = 180.4$$

The value of ΔX corresponding to the above condition may now be obtained through the use of equation (5).

$$\Delta X_n = \frac{\lambda g}{\pi SWR} \quad \text{let } \lambda g = 3\text{cm} \qquad \Delta X_2 - \Delta X_1 = .0520.10^{-2}\text{ cm}$$

$$\Delta X_1 = \frac{3}{\pi 200} = .4777.10^{-2}\text{ cm}$$

$$\Delta X_2 = \frac{3}{\pi 180.4} = .5297.10^{-2}\text{ cm}$$

With the readout capability of $\pm 10^{-4}$ cm, an error of approximately 20 per cent would be resultant in the calculation of the loss tangent regardless of other sources of error (since $\Delta X \propto \tan\delta$ by equation (2)). A further calculation starting with a VSWR = 50 in empty guide and the same .01 db return loss through the inserted sample will result in a value of .00022 for ΔX. With the same readout capability as in the former case, this value of ΔX would imply an error approaching 50 per cent in the loss tangent. From these two cases, it would appear that a VSWR higher than 200 is required in order to determine ΔX by a conventional mechanical readout system.

However, it is not possible, at K band for example, to obtain a VSWR of over 160 on a 10" section of waveguide as the following consideration illustrates: (on an oven capable of maintaining 1600°C, 10" could be about the minimum length of guide from short to slotted section as in Figure 3).

Assume a distance of 10" between short and slotted line. Let the guide be of pure silver (.1db attn./ft.).[10] The return loss from the guide would be:

$$10'' \times \frac{1^1}{12''} \times .1db \times 2 = .16667 \text{ db return loss}$$

$$\text{then: } .16667db = 20 \log \frac{SWR+1}{SWR-1} \text{ or } SWR \sim 97$$

As a VSWR approaching 200 is then unattainable in the practical case, the only alternative would be to increase the sample size in the direction of the guide axis (d* in Figure 2) which would in turn increase ΔX. However, sample materials from existing radomes under development are necessarily less than a quarter guide wavelength thick at any given frequency. At K band, this obtainable sample size necessitates a VSWR higher than that theoretically obtainable.

The high error will not always be had, particularly when one has an exceptionally lossy sample, in which case ΔX will increase to a value such that the error could go as low as 1 per cent. However, with the low loss materials that are desired in radome or electromagnetic window applications, ΔX will remain small and the lower the loss, the higher the empty guide VSWR must be in order to determine the loss tangent with any reasonable degree of accuracy.

B. Residual VSWR

The residual VSWR of a system arises from one or more low loss discontinuities such as flanged joints and slots in slotted sections.

This residual VSWR can be calibrated from the system if one has a movable short which duplicates that of the shorted sample holder. The sample holding short however, must be designed and constructed for the highest VSWR attainable as has been shown to be necessary. Construction of a sliding short to duplicate this condition over a wide linear range would be impractical, in particular since "sliding" implies that the short may not be even a good one electrically.

The residual VSWR of a slotted line is given as $1 + \frac{2\pi A}{\lambda g}$ where A is the peak to peak linear error of the slotted line.[11] That is, if a short is moved away from the end of a slotted line, a null position on the line will vary in amplitude as a sine wave. A is then the peak to peak value of this sine wave or the tracking error.

With a residual VSWR of 1.01 (typical of the best commercial slotted sections), A can vary between .010 cm and .003 cm for frequencies between C and K band respectively. From the example presented earlier in this paper, ΔX_n may be on the order of magnitude of A. If then, calibration of the particular system utilized here is impractical, the tracking error may cause an error in the loss tangent as high as 50 per cent.

The errors in linear measured quantities are not only applicable to the loss tangent, but to the determination of the dielectric constant, K, as well. Consider the case where the dielectric constant of a material is 4.00, and a sample is made with its length equal to a quarter guide wavelength. By use of the relation:

$$\lambda = \frac{1}{f\sqrt{\mu\epsilon}}$$ where for good dielelectrics

$\mu = \mu_o$, it can be shown that the standing wave shift, $(X_2 - X_1)$ in equation (3), will be a quarter guide wavelength.

Any error introduced in measuring this quantity is negligible. Consider further however, the case where the dielectric constant is 9.00. Here there will be no null shift. It is then theoretically possible to have a null shift that can only be measured to a very high degree of error even with $\pm 10^{-4}$ cm capability. From equation (3), a shift this small, though, would produce little error in the value of X_o and hence little in the determined value of K.

Also, the magnitude of error in measuring ΔX will appear in equation (4) where values of VSWR are required. The error will appear in the propagation constant, γ, of the material and in turn in K. This will be the case if equation (4) instead of (4A) is used when precise solution for γ is required (i.e., when, as a minimum, ±1 per cent error can be tolerable in determining K).

C. Sources of Various Other Errors

1. Attenuation

When determining ΔX, the 3 db level is found by using a precision attentuator. The best commercial units available specify a readout tolerance of .1 db or 2 per cent, whichever is greater. A simple analysis will reveal that with this tolerance, the error in determining the 3 db points will give a linear deviation in ΔX of approximately $11 \cdot 10^{-7}$ cm. Assuming that a VSWR of 50

or 34 db is obtained and that the SWR pattern has the form $y = A \sin^2\theta$ where A is a constant then:

$$34 \text{ db} = 10 \log y$$

$$34 \text{ db} = 10 \log (A \sin^2\theta)$$

@ $\theta = 90°$, $\sin^2\theta = 1$ and $A = 25000$

$$y \text{ in db} = 10 \log 25000 \sin^2\theta \qquad (1)$$

differentiating: $\frac{\Delta y}{\Delta\theta} = \frac{20}{\sin\theta} (\log e) (\cos\theta)$ (2)

@ y = 3 db, $\sin\theta$ and $\cos\theta$ are determined from (1) and substituting in (2) results in $\frac{\Delta y \text{ db}}{\Delta\theta} = 970$. When $\Delta y = .1$ db, $\hat{\theta} = 1.032.10^{-4}°$ which at X band gives a linear deviation of $11 \cdot 10^{-7}$ cm.

This figure will increase with lower values of VSWR, however it has been shown that a VSWR well above 50 is required. A value of VSWR of 50 though is easily attained and as the deviation of $11 \cdot 10^{-7}$ cm is far smaller than a readout capability of $\pm 10^{-4}$ cm, the error introduced here is seen to be far less than that of other sources and in the practical case may be considered negligible.

2. Error Related to Frequency Stability and Modulation

Frequency instability will have the effect of causing an increase in measured values of ΔX.[12] The loss tangent would then contain a further error from this effect. The effect, however, may be made minimal by the addition of 1000 cycle amplitude modulation of the carrier signal by utilizing a waveguide crystal switching circuit. With the further addition of an oscillator synchronizer, frequency stability of the klystron can then be expected to be within 10^{-4} per cent per week or 10^{-6} per cent per day.

3. Multiple Reflections

Multiple reflections, caused by the existence of higher modes of transmission within the sample under test, may cause a serious error in all measurements at the slotted section and as a result negates the use of large samples.

The precise effect of this phenomenon, however, has not been determined and it must suffice to say that care must be taken to see that the sample dimensions are not quarter or half wavelength multiples of these higher modes.[13]

4. Temperature

As measurements on materials for radomes are often done at high temperatures, there will enter expansion errors.

The error effects of thermal expansion of the microwave system can be divided into two types: measurable and indeterminant. The measurable errors are primarily those involving determination of lengths and the problem of fits.

If standard waveguide is utilized, that is with tolerances of ±.003" at X band and ±.002" at K band, an empiracal fit correction must be applied to the measured value of K:[14] See Figure 4.

$$K_{true} = (K_{measured}{}^{-1}) \cdot \left(\frac{h}{h^1} + 1 \right)$$

The exact value of a given dielectric is not known, therefore, it can only be said that the value of K is shifted to a more correct value but that a percentage error will still remain. For example, if a material has a dielectric constant of 8.637 exactly and the measured value is 8.59[illegible] within 3 per cent, the fit correction may yield 8.620 but still with the initially associated error.

The indeterminant error lies in the temperature difference between the slotted line and the heated sample. The configuration illustrated in Figure 3 might have a 10" to 12" distance between slotted section and short with a temperature difference of 1600°C. As the guide inner dimensions will not be the same over this distance neither will the field configuration remain unaffected.

The magnitude of the standing wave within the guide will change with position as attenuation of the walls will vary with the temperature gradient from sample to slotted line. The problem here is compounded by a temperature stability of approximately ±10 to 15°C at best when taking measurements at 1600°C. As a result, measured linear quantities would not be the same at the slotted section as directly in front of the slotted line. Considering the nonlinearities in the change of the standing wave pattern in the sample contrasted to the change of the pattern in empty guide with a change in temperature, the error introduced here would be fairly difficult to determine.

5. Mechanically Introduced Error and Repetition

The slotted line probe can produce an error by disturbing the standing waves within the guide, but if the penetration of the probe is set such that at maximum VSWR meter sensitivity, vertical movement of the probe causes very little or no change in ΔX or the null shift, this error is effectively eliminated.[15]

On a side drive slotted line however, gimballing of the probe can result from the effects of the drive upon the ways of the probe carriage. At high values of VSWR, this effect has in practice shown to produce incorrect data. Variations in ambient temperature can tighten

or loosen the fit of the drive to the carriage and in turn cause a change in the verticality of the probe with an error resulting in all linear measurement.

Concerning repetition, it has been determined experimentally that if the slotted line has a linear readout capability of 10^{-4} cm or smaller, determination of a linear position cannot be made repetitively as the VSWR meter null readings are not quite sharp enough and utilization of the slotted line's readout capability is then lost.

III. CONCLUSION

The produced error is seen to arise from many sources and will vary particularly with the precision of mechanical readout. The error contained in the determination of tanδ may be quite high as has been shown. Also, the accuracy of determining tanδ will depend on the loss characteristics and chosen widths of samples and a precise prediction of error will not be attempted.

The dielectric constant may be determined to a higher degree of accuracy than the loss tangent as the linear measurement necessary, $(X_2 - X_1)$ is not in direct proportion to K and it has been shown that when the quantity becomes so small as to be measured only with high error, no major error is contributed to the value of K.

A figure of within 5 per cent may be considered to be typical but may increase depending on the precision of equipment utilized and care expended in achieving high stability of both frequency and temperature.

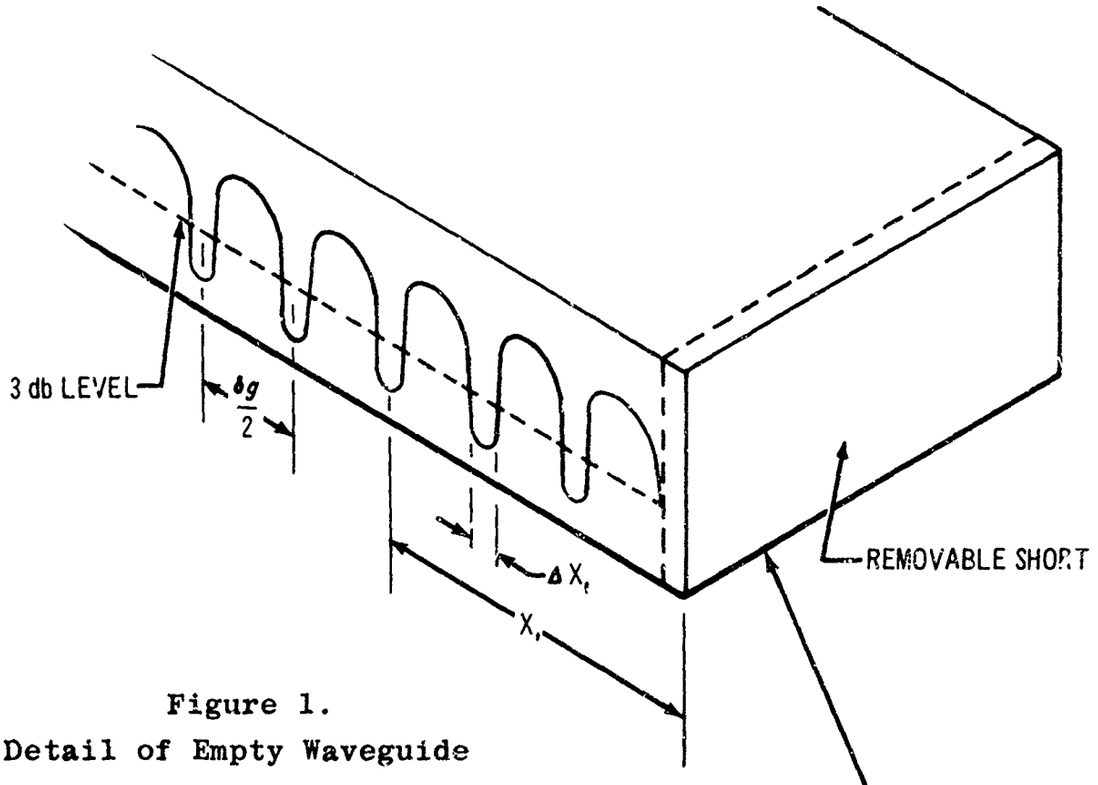

Figure 1.
Detail of Empty Waveguide

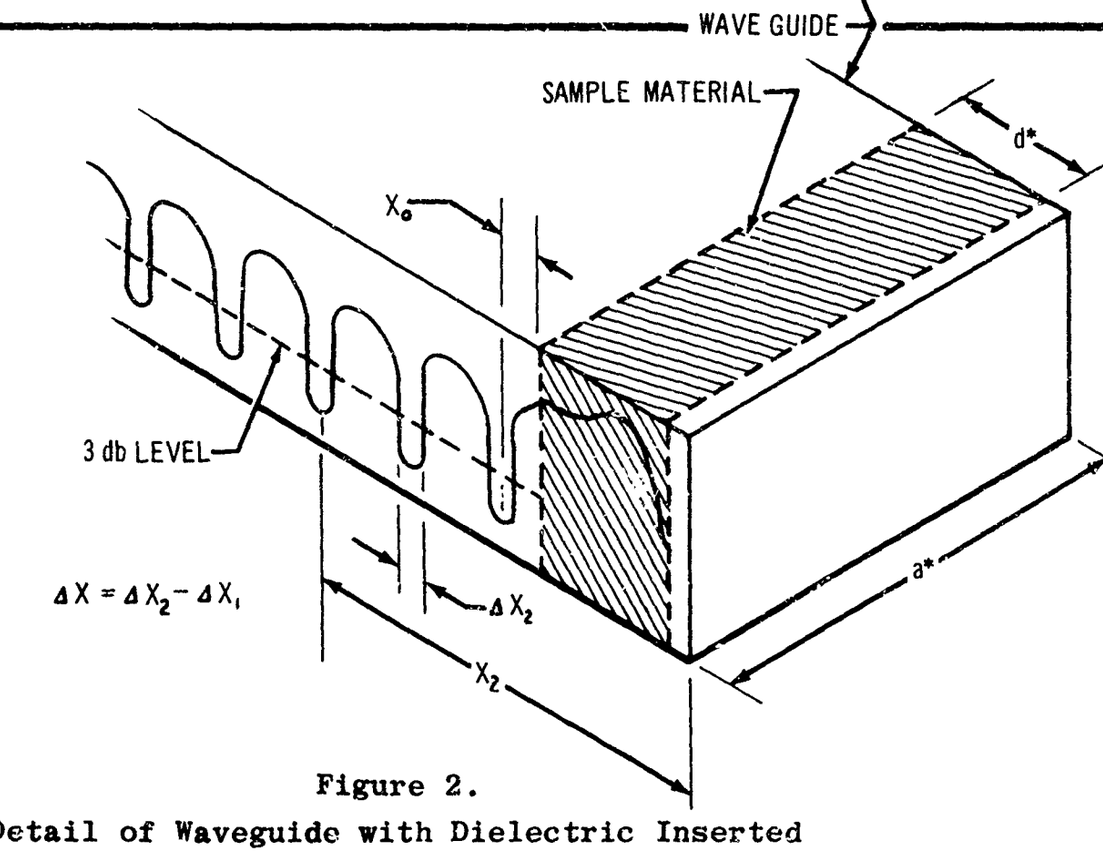

Figure 2.
Detail of Waveguide with Dielectric Inserted

Figure 3.

Detail of Typical Apparatus Arrangement

Figure 4.

Cross Sectional View of Dielectric Sample within Waveguide

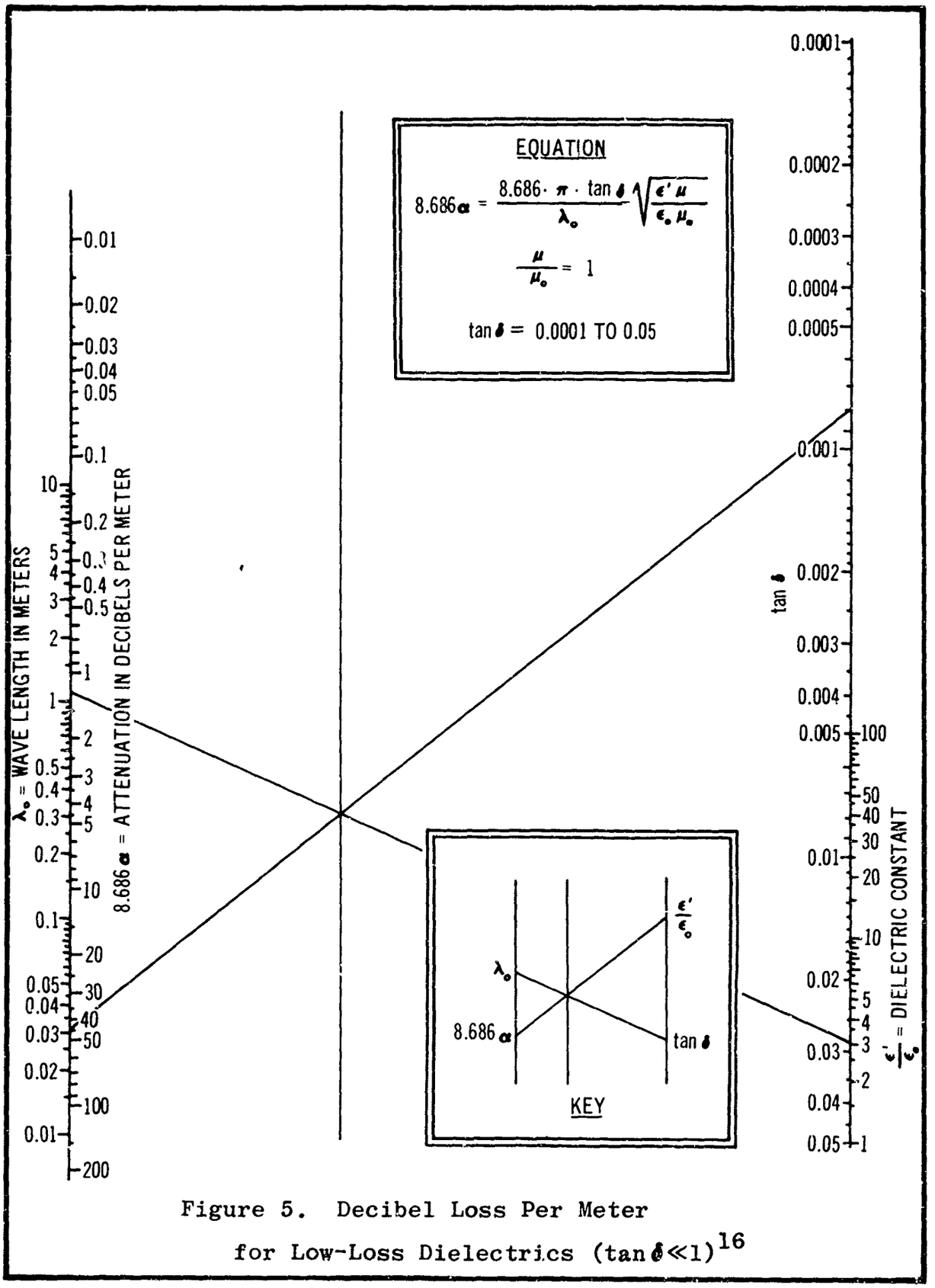

Figure 5. Decibel Loss Per Meter for Low-Loss Dielectrics ($\tan\delta \ll 1$)[16]

REFERENCES

1 "Proceedings of the OSU-WADD Symposium on Electromagnetic Windows", R. Fouty and W. Green, WADD Technical Report 60-274, Wright Air Development Division, Wright-Patterson Air Force Base, Ohio, 1961, see page 497

2 see 1, page 451

3 M.I.T. Radiation Laboratory Series, Volume 11 "Technique of Microwave Measurements", C. G. Montgomery, ed. McGraw Hill, New York, 1947, see pages 625 to 657

4 A. R. vonHippel, "Dielectrics and Waves", Wiley, New York, 1954, see pages 73 to 77

5 A. R. vonHippel, "Dielectric Materials and Applications", Wiley, New York, 1954, see pages 65 to 69

6 Melpar, Inc., Falls Church, Virginia, Technical Report "A Tentative Method for Measuring Dielectric Constant and Loss at Microwave Frequencies"

7 see 6, page 20

8 see 6, page 22

9 Hewlett-Packard Company Operating Manual for 415-C SWR Meter, see pages 3 to 7

10 "Standard Waveguide Data", Narda Microwave Corporation general catalog

11 Hewlett-Packard Company, Palo Alto, California application note 38, "Microwave Measurements for Calibration Laboratories", second edition, 1962, see pages 15 to 21, section 4 and page 11, section 4

12 see 6, page 26

13 see 6, page 27

14 see 3, page 576

15 see 6, page 26

16 see 5, page 297, also pages 297 and 298 for additional nomographs